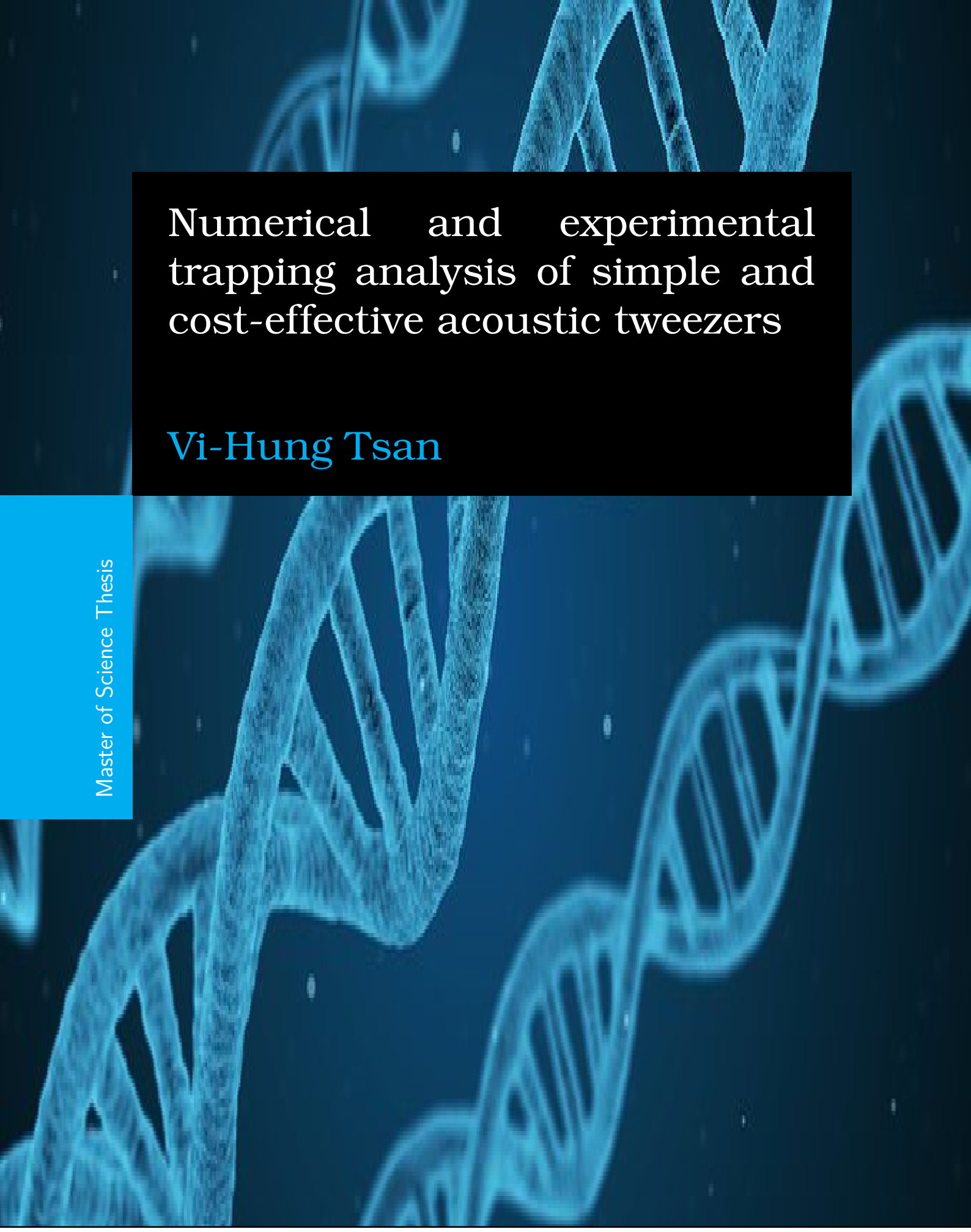

Numerical and experimental trapping analysis of simple and cost-effective acoustic tweezers

Vi-Hung Tsan

Master of Science Thesis

TU Delft Delft University of Technology

Delft Center for Systems and Control

Numerical and experimental trapping analysis of simple and cost-effective acoustic tweezers

Master of Science Thesis

For the degree of Master of Science in Systems and Control, Mechanical Engineering at Delft University of Technology

Vi-Hung Tsan

September 8, 2022

Faculty of Mechanical, Maritime and Materials Engineering (3mE) · Delft University of Technology

Delft University of Technology
Department of
Delft Center for Systems and Control (dcsc)

The undersigned hereby certify that they have read and recommend to the Faculty of Mechanical, Maritime and Materials Engineering (3mE) for acceptance a thesis entitled

Numerical and experimental trapping analysis of simple and cost-effective acoustic tweezers

by

Vi-Hung Tsan

in partial fulfillment of the requirements for the degree of

Master of Science Systems and Control, Mechanical Engineering

Dated: September 8, 2022

Supervisor(s):

dr. C.S. Smith

dr. G.J. Verbiest

dr. D. Fan

Reader(s):

dr.ir. J.F.L. Goosen

Abstract

Acoustic Force Spectroscopy (AFS) is a versatile tool that uses sound waves to manipulate tiny particles such as cells, bacteria, and even zebrafish embryos in microfluidic systems. This kind of acoustic tweezer is gaining increasing attention due to its high throughput capability and non-invasiveness. In addition, this device allows for parallel manipulation of bio-molecules. Therefore, it can provide statistically significant data about the DNA replication process, which is widely considered a stochastic process. Understanding the dynamics of the DNA replication process plays a vital role in developing medicine to cure diseases that are still incurable today.

Most single-molecule techniques, such as optical tweezers, magnetic tweezers, and atomic force microscopy, can only manipulate a limited number of particles simultaneously. Therefore, obtaining statistically significant data with these methods is laborious, time-consuming, and expensive.

This report describes the design, fabrication, simulation and characterization of an easy-to-build and cost-effective acoustic tweezer. The trapping stiffness of this device is derived from finite element modelling and experiments. This property is used to benchmark the acoustic tweezer developed in this project against other microparticle manipulation devices found in the literature. The results show that the acoustic tweezer developed in this project provides sufficient trap stiffness for studying DNA replication.

Table of Contents

List of Figures

List of Tables

Preface & Acknowledgements

> "I hear and I forget. I see and I remember. I do and I understand."
>
> — *Confucius*

I would like to thank my supervisors, Carlas Smith, Gerard Verbiest, and Daniel Fan, for their support and valuable and pragmatic advice throughout my thesis. I started my thesis in the middle of the COVID-19 pandemic. During this time, I was a bit lost and did not know what I wanted after studying at the university. After discussions with my supervisors about potential research topics, I realized the importance of technology and its value in understanding and curing diseases such as COVID-19. I am naturally curious and grateful that I can apply everything I have learned from my double master's degree in this thesis project, which consists of mechanical design and control aspects. This project's hands-on nature helped me understand the topics and gain insight into the current developments concerning the research topic.

I would also like to thank Sabina Caneva for presenting me the work and methodology used by students in her group in developing acoustic tweezers, Murali Ghatkesar for the lively discussion on acoustic impedance and methods to check if the piezo chip works properly, Gurhan Ozkayar on the microfluidic operation and Dong Hoon Shin, Gideon Emmanuel and Andres Hunt for help with glass cutting and drilling.

Finally, I would like to thank my family and friends for their unwavering support and love. Without them, my life would be much more challenging during this pandemic.

Chapter 1

Introduction

This chapter serves as a general introduction to this report. First one will read a short introduction about the subject Acoustic Force Spectroscopy (AFS) and its state-of-the-art applications to biology. Hereafter, the relevance of this thesis report and the objective are discussed. Finally, an outline of this report is presented covering the most important topics concerning the AFS chip.

1-1 Acoustic tweezer

In this section, the working principle and performance of the AFS chip will be explored and compared to other available configurations. Hereafter, the main focus is on acoustic tweezers, and we will discuss the pros and cons of each kind of acoustic tweezer and narrow it down to the bulk acoustic wave (BAW) type and discuss its operating modes.

1-1-1 Working principle

A schematic representation of a general AFS device is shown in Figure 1-1.

The most critical part of the design process in this thesis is the chip/flow cell. The piezo element on top of the top glass layer will be excited at a specific frequency. This leads to the forming of waves in the fluid layer Ψ_{In} and scattering of these waves around the beads Ψ_s (in m^2/s) as is shown in Figure 1-2.

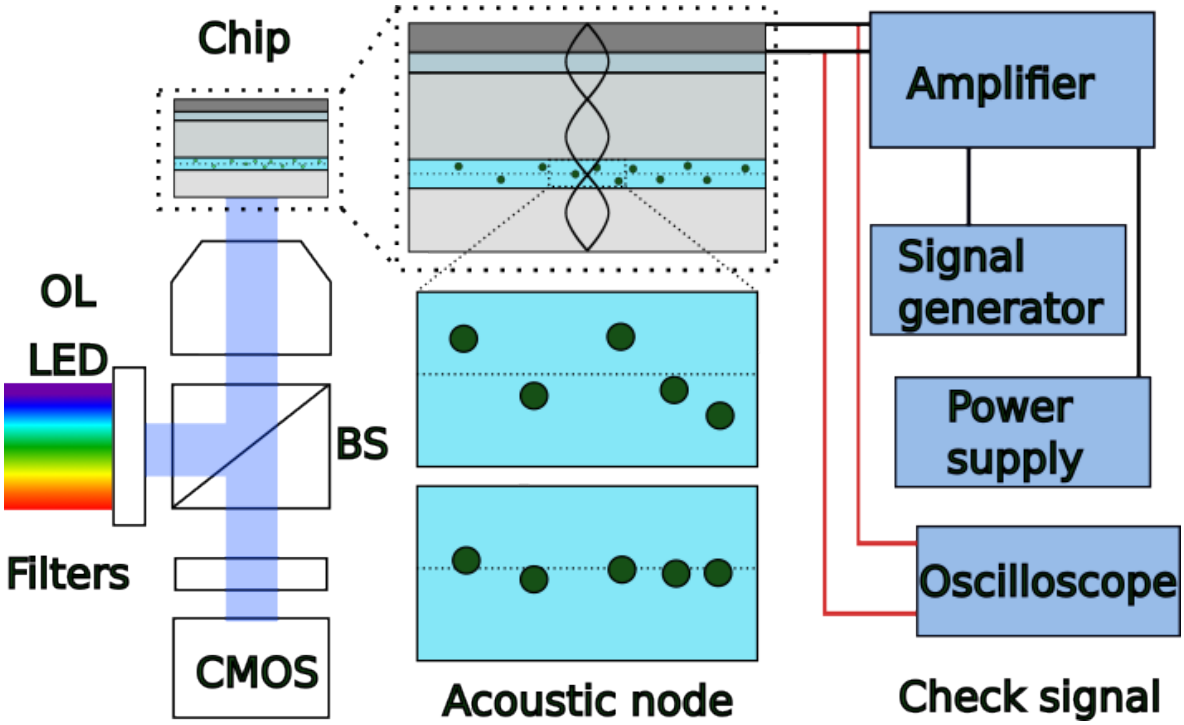

Figure 1-1: General setup of an Acoustic Force Spectroscopy (AFS). The chip/flow cell in this thesis consists of 5 layers. From top to bottom we have: the piezoceramic, aluminium layer, top glass plate, the fluid channel and the bottom glass plate. The 1.5-micron diameter beads (green particles) are focused on the acoustic node whenever the chip is driven with its resonance frequency. Images of the beads are captured with an inverted microscope consisting of the water immersed objective lens (OL) at 64 times magnification, beamsplitter (BS), filtered LED light source (470 nm) and the digital camera (CMOS).

The resulting first-order wave is the superposition of incoming and scattered waves:

$$\Psi_1 = \Psi_{In} + \Psi_s \tag{1-1}$$

Settnes et al. [70] and Bruus et al. [10] showed that for a standing waves Ψ_{In}, the acoustic radiation energy and force on the micro-particle as a results of these waves can be described by the equations in chapter 2, Equation 2-8 and Equation 2-9, respectively.

Standing waves are created in the flow cell when it is driven at its resonance frequency. When this happens, an acoustic pressure node will be created in the fluid layer where the net force on particles equals zero. Particles and beads in the fluid will be attracted to this node; hence, a force can be applied to the DNA chain attached to the bead. The force balance of all the forces acting on the bead in this node can be described by [44]:

$$0 = F_{rad,trap} + F_{Buoyancy} - F_{drag} - F_g \tag{1-2}$$

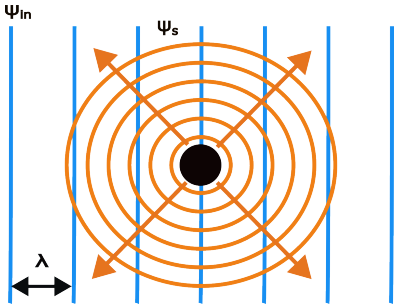

Figure 1-2: Microparticle subjected to incoming acoustic field Ψ_{In} (vertical blue lines) with a wavelength of λ, which leads to an outgoing scattered wave Ψ_s around the particle. Adapted from [70] and [10].

Where $F_{rad,trap}$ represents the acoustic radiation force at the trap location, $F_{Buoyancy}$ the buoyancy force, F_{drag} the drag force due to a viscous fluid, and F_g the gravitational force on the bead (all in N).

1-1-2 Comparison between state-of-the-art microparticle manipulation methods

Besides acoustic tweezers, several tweezers based on different principles already exist [64]. The different particle-manipulation tweezers are summarized in the Table 1-1. This table shows that the acoustic tweezers are relatively efficient in power consumption, and no special equipment or particles are needed apart from the acoustic source. Optical and magnetic tweezers offer the best spatial resolution, but optical tweezers require high input power and complex optics. The high input power can damage cells [8]. Magnetic tweezers need specialized beads and can manipulate a limited range of beads sizes. Plasmonic tweezers are related to optical tweezers. They rely on locally enhanced electromagnetic fields to trap beads and require lower input power, but the local fields can lead to substantial heating of the surrounding fluid [15]. Electrokinetic tweezers rely on an electric field to manipulate particles. So they are dependent on the polarizability of the particles. Finally, hydrodynamic tweezers use fluid flow streaming around an object to trap particles at specified locations [56], so it is harder to change the locations of the particles once the geometry is fixed, and it requires complex flow-control algorithms.

Compared to the other methods, acoustic tweezers are more cost-effective and apply to a broader range of particles. However, the spatial resolution is sacrificed for high throughput by choosing this method. However, as shown by Sitters et al. [71], acoustic tweezers can still provide comparable results to magnetic tweezers. Furthermore, acoustic standing wave tweezers can perform particle manipulation on multiple DNA chains in parallel. Therefore, it can provide higher throughput experimental data since it does not rely as much on local fields as the other platforms do.

Acoustic tweezers can, in turn, be subdivided into different operating principles, as shown in Figure 1-3. In Table 1-2, the advantages and disadvantages and suitable applications are listed.

Both bulk acoustic wave (BAW) and surface acoustic wave (SAW) belong to the group of standing-wave tweezers. BAWs use piezoelectric transducers to create standing waves in the

Table 1-1: Different particle-manipulation platforms adapted from [64]. *The field strength for the magnetic and electrokinetic tweezers are the minimum values. Different units are shown since power usage depends on geometry, material properties and distance between electrodes.

Technique	Size range	Input power (W/cm^2)	Spatial resolution	Labeling required	Additional system requirements
Acoustic tweezers[71]	100 nm-10 mm	10^{-2}-10	1-10 μm	No	Acoustic source
Optical tweezers[4],[3],[89]	100 nm-1 mm	10^6-10^7	0.1-1 nm	Required for smaller particles	High-powered laser, high-numerical-aperture lens
Magnetic tweezers[6]	1 μm-10 μm	1-10 $tesla^*$	1-10 nm	Yes	Permanent magnet, superparamagnetic beads
Optoelectronic tweezers[86]	100 nm-10 μm	10^{-2}-10	1-10 μm	No	Photoconductive substrate, low-conductivity media
Plasmonic tweezers[84]	10 nm-1 μm	10^2-10^4	10-100 nm	No	plasmonic substrate, heat sink
Electrokinetic tweezers[68],[18]	1 nm-1 mm	10^4-10^7 V/m^*	0.1-1 μm	Yes	Prepatterned electrodes, Low-conductivity media
Hydrodynamic tweezers[56]	100 nm-1 mm	N/A	1-10 μm	No	Multiple pressure regulators, flow-control algorithm

fluid layer. SAWs, on the other hand, use interdigitated transducers (IDTs), which are patterned on a piezoelectric surface to create the required acoustic waves. While surface acoustic waves can provide a more precise 3D particle manipulation, it offers limited throughput. On the other hand, the travelling wave and acoustic-streaming tweezers rely on fluid flow. As a result, they are more complex to simulate and design. So the bulk acoustic wave tweezer is the most viable option in this case.

The bulk acoustic wave tweezers can be divided into two configurations: the layered resonator type and the transversal resonator type as described by A. Lenshof et al. [52] and shown in Figure 1-4. Each configuration has its distinct advantages and disadvantages. The main advantage of the transversal resonator configuration is that it provides in-plane trapping. This eases tracking of the bead, but it can not compensate for gravity effects and is, therefore, less precise than the layered resonator. The layered resonator can compensate for gravity effects since the manipulation direction is the same as gravitational force. Therefore the layered resonator is of primary interest, and subsequent sections and chapters will only focus on this resonator type.

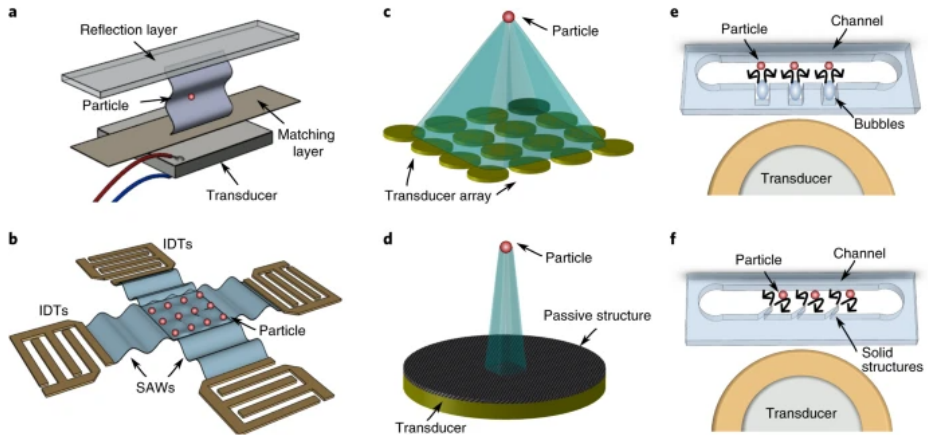

Figure 1-3: Sketch of various acoustic tweezers. (a) A typical bulk acoustic wave (BAW) standing-wave device. (b) surface acoustic wave (SAW) based standing-wave device. (c) An active travelling-wave device with a transducer array for particle manipulation. (d) Single transducer passive travelling-wave device for particle manipulation. (e) An acoustic-streaming device that generates out-of-the-plane acoustic micro-streaming flows with oscillating micro-bubbles. (f) A solid-structure-based acoustic-streaming device that generates directional fluid flow with acoustic excitation. Adapted from [64].

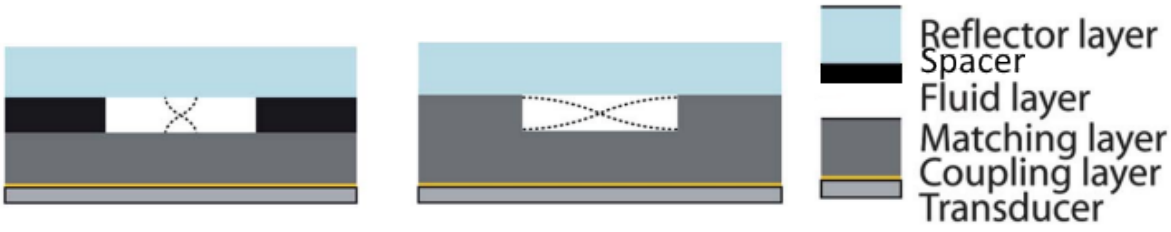

Figure 1-4: Two configurations of the bulk acoustic wave acoustic tweezer. (a) Layered resonator (b) Transversal resonator. Adapted from [52].

1-1-3 Operating modes

This thesis focuses on the layered resonator as described by A. Lenshof [52]. A layered resonator is a structure composed of different layers of different materials, as shown in Figure 1-1. The sound waves of the piezoelectric actuator pass through all the layers. This resonator type is the most suitable structure for the available setup.

The most common mode of operation of the layered resonator is the half-wave mode because of its stability [52]. This mode is shown in Figure 1-4a, where the acoustic node is located at the center of the flow channel. Another operation mode is the quarter wavelength mode. This mode is shown in Figure 1-5. This mode enables its user to trap beads closer to the glass layer. However, this mode is less stable, and simulations are required to determine its behaviour [80].

While the aforementioned half-wave mode and the quarter-wave mode are explored the most in literature, it is by no means a restriction on the modes that can be applied. However, this

Table 1-2: Different types of acoustic tweezers adapted from [64]

Type	Subtype	Advantages	Disadvantages	Applications
Standing-wave	Surface acoustic waves[22]	Precision (ability to manipulate nano-particles), simple, compact, inexpensive devices and accessories	Low throughput (<1mL/min) and limited acoustic -field pattern	Nanoparticle manipulation, cell separation, cell patterning, cell concentration, 3D translation and rotation
	Bulk acoustic waves[21]	High throughput (10 mL/min)	Limited precision and excessive heat generated due to high power	Cell separation, sample preparation, levitation of cells and small organisms
Traveling-wave	Active[58]	Flexibility (ability to rewrite the acoustic field in real time)	Typically multiple transducers needed; multiplexed transmission system needed	Cell sorting, real-time cell patterning for bioprintng and tissue engineering, 3D translation and rotation of cells and droplets
	Passive[61]	Simple, easily fabricated structures and simple electronic control scheme	Generation of only a few acoustic-field patterns with one structure and complex simulation and calculations needed	cell patterning, levitation of droplets, high-resolution ultrasonic imaging
Acoustic-streaming	Bubble based[1]	selective frequency actuation	Unstable bubble size and limited reproducibility	Fluid mixing and pumping, 3D rotation of cells and small organisms, neural stimulation
	Solid structure based[39]	stability, reproducibility and ability to handle highly viscous fluids (such as blood and sputum)	Limited vibration patterns	Fluid mixing and pumping 3D rotation of cell and small organisms

thesis focuses on the half-wave mode, which is used to validate the trapping capability shown in the simulation results discussed in section 5-1.

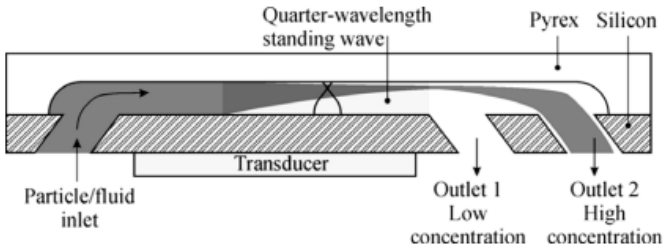

Figure 1-5: Sketch of a quarter-wave operation mode adapted from [80].

1-2 Biological aspects

In this section, the material properties of DNA obtained with trapping devices will be explored, and a short introduction will be given to the DNA replication process. Also, the results of existing trapping devices will be examined and used as a reference for the acoustic force device in this report.

1-2-1 Elasticity of DNA

A DNA chain can consist of either a single or double strand, as shown in Figure 1-6. The elasticity is different for both configurations. For the single-stranded DNA (ssDNA) con-

figuration, the freely jointed chain (FJC) model is the most accurate model to describe its elasticity. And for the double-stranded DNA (dsDNA), the worm-like chain (WLC) model is best suited to describe its elasticity [13].

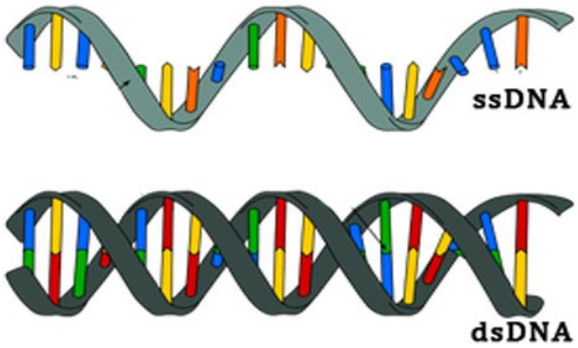

Figure 1-6: Sketch of a single-stranded DNA (ssDNA) as the top image and a double-stranded DNA (dsDNA) as the bottom image from [47]

.

The FJC model represents the DNA chain as a discrete chain of uncorrelated segments of length b connected with joints, as is shown in Figure 1-7. The force-extension relationship of a ssDNA chain for this model reads as [73]:

$$\langle x \rangle = L(\coth \frac{Fb}{k_{\mathrm{B}}T} - \frac{k_{\mathrm{B}}T}{Fb}) \tag{1-3}$$

Where $\langle x \rangle$ represents the end-to-end distance of the DNA chain (in m), L the molecular contour length (in m), T the temperature (in K), k_B the Boltzmann constant (in $\mathrm{m^2 kgs^{-2} K^{-1}}$), b the length of uncorrelated Kuhn segments (in m) as is shown in Figure 1-7 and F is the force applied to the chain (in N).

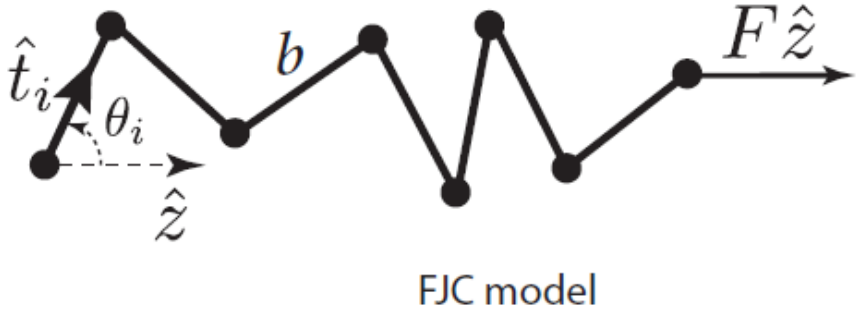

Figure 1-7: Sketch of the FJC model, which represents the DNA chain as a discrete sequence of uncorrelated (Kuhn) segments of length b, direction vector $\hat{t}_i$ for segment i, direction angle θ_i for segment i and a force F applied to the end in direction $\hat{z}$ of the chain adapted from [13].

The WLC model assumes a worm-like configuration as is shown in Figure 1-8. In this case, its force-extension relation can be described by the polymer model described by Bustamante et al. [12] [11], which reads as:

$$\mathrm{FA}/(k_B T) = \frac{1}{4}(1 - x/L)^{-2} - \frac{1}{4} + x/L \tag{1-4}$$

Where F represent the force on the DNA chain (in N), A is the persistence length of the polymer representing the DNA (in m), k_B is the Boltzmann's constant, T the absolute temperature (in K), L the molecular contour length (length at maximum possible extension) (in m) and x the end-tot-end extension of the DNA (in m) as is shown in Figure 1-8.

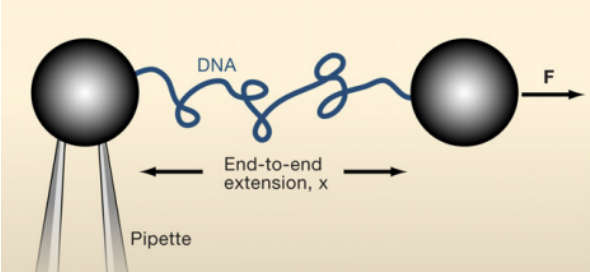

Figure 1-8: Worm-like chain model of DNA corresponding where the elasticity corresponds to Equation 1-4 from [11].

The WLC model represents the DNA chain as a continuous elastic chain with a bending stiffness term [13]. This representation is shown in Figure 1-9.

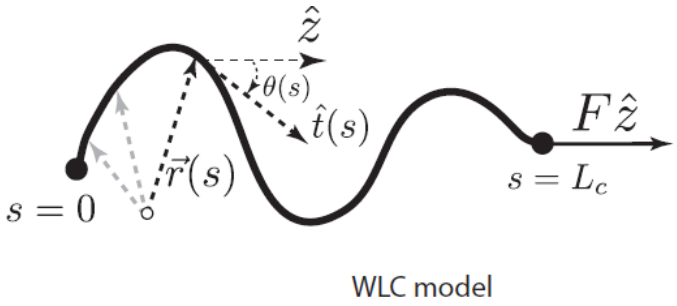

Figure 1-9: Sketch of the WLC model, which represents the DNA chain as a continuous chain with bending stiffness. Where $\vec{r}$(s) represents the position vector along the chain at point s, position angle θ(s) at point s, $\hat{t}$(s) the tangent vector at point s, and F the force applied at the end of the chain in direction $\hat{z}$ adapted from [13].

The characteristic shape force-extension plot are different for the ssDNA and dsDNA as can be seen in Figure 1-10. In this figure, one can see the force-extension curve for a torsionally unconstrained DNA chain. For the dsDNA case (plotted as gray lines and fitted by the orange and red lines using Equation 1-4), one can observe that at approximately 65 pN, the force-extension plot becomes flat, and the force does not increase much while the DNA is being stretched. This happens because the first part of the extension is due to unstretching of the DNA chain, and at 65 pN, overstretching transition takes place where the stretching

happens due to force-induced melting of the two strands [82]. The elasticity of the DNA is also reported to be dependent on the concentration of salt and the temperature [13]. The overstretching transition for a torsionally constrained DNA is reported to take place at forces around 110 pN [82]. The force-extension plot for the ssDNA is plotted with dark gray line and fitted with the blue and green lines using Equation 1-3.

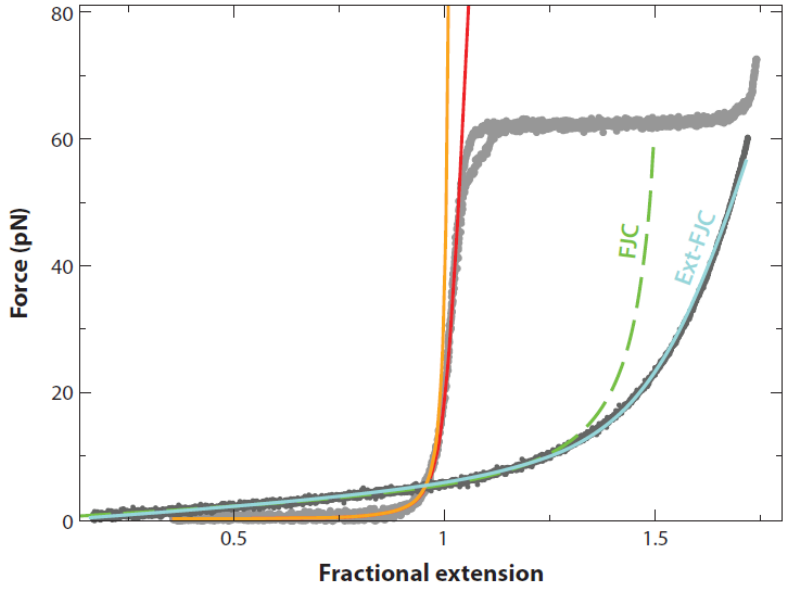

Figure 1-10: A plot of the DNA elasticity force-extension curve of a λ phage DNA (NEB) with a contour length of 16.4 μm in 150 mM NaCl buffer [72] obtained with an optical tweezer for dsDNA (light gray curve), WLC model fit (orange curve), extensible-WLC model (red-curve), ssDNA force-extension curve obtained with an optical tweezer (dark gray), FJC model fit for ssDNA extension (green dashed curve) and extensible-FJC model fit (cyan) for ssDNA adapted from [13].

1-2-2 DNA replication

In 1953 Watson et al. identified the first enzyme that is capable of synthesizing (replicating) DNA [85]. This enzyme is called the DNA polymerase (DNApol). The DNA is separated into two strands for replication by an enzyme called helicase. Each one is then used as a template for a new DNA strand. One strand will be synthesized continuously, which is called the leading strand, and the other is synthesized discontinuously, called the lagging strand. The DNApol can be seen as a molecular motor that converts chemical energy into mechanical force to move over the template. Its translocation have been linked to the conformational change of the DNApol subdomain as is shown in Figure 1-11 [32]. However, the actual mechanism for the translocation is still unknown [9].

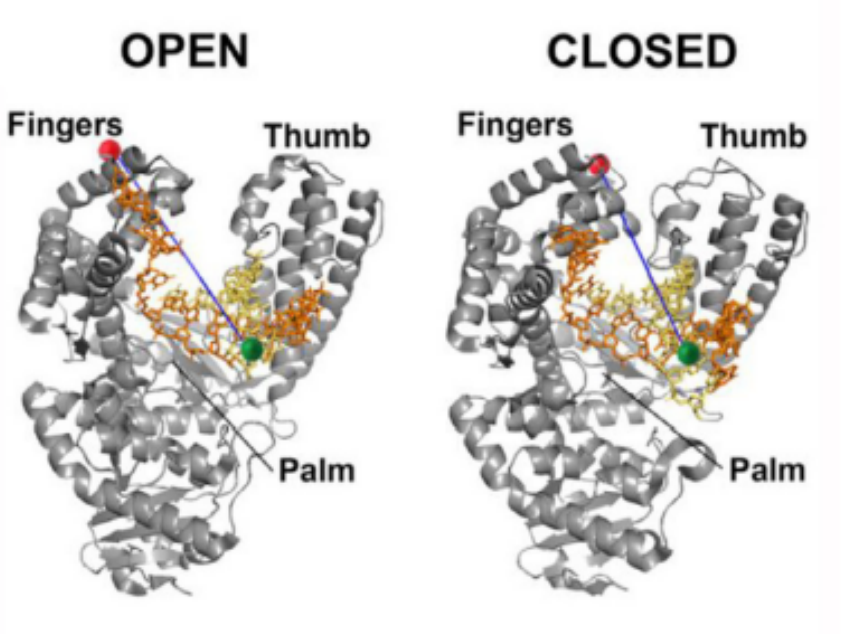

Figure 1-11: Conformational change in DNApol subdomain called the fingers are switching between the closed and open state. The red and green particles are fluorophores used to detect the open and close state adapted from [9].

Wuite et al. [87] showed with an optical trapping device that the replication rate depends on the applied tension on the template strands. An increase in tension also increases the replication rate to a certain point. A further increase in the tension will reduce the replication rate till stalling. This can be explained by the conformational change of the DNApol shown in Figure 1-11. The replication process is essentially converting a ssDNA into a dsDNA by the DNApol. The authors studied the T7 DNA polymerase and assumed that the optical trapping force exerted on the template would exert torque on the fingers. A schematic sketch of the setup used in their experiments is shown in Figure 1-12a, and the work $W(F)$ (in Nm) needed to close the fingers is given in Equation 1-5.

$$W(F) = aF + nF\left(x_{\mathrm{ss}}(F) - x_{\mathrm{ds}}(F)\right) \tag{1-5}$$

Where F represents the force exerted on the template (in N), a is the distance moved by the fingers along the pulling direction of the template (in m), and n is the number of sugar-phosphate units that are organized from single- to double-stranded geometry by closing the fingers, x_{ss} and x_{ds} the end-to-end distance per base of ssDNA and dsDNA (in m). The second term on the right-hand side of Equation 1-5 can change sign and therefore either assist or oppose the replication process. With this model, the replication rate k (in bases/s) can be expressed as:

$$k = k_0 e^{-((W(F)-T\Delta S)/k_{\mathrm{b}}T)} \tag{1-6}$$

Where k_0 represents the rate coefficient at $F = 0$ (in bases/s), k_b the Boltzman constant, T the temperature, $W(F)$ the work described in Equation 1-5 and ΔS the entropy change (in J/K) needed to convert ssDNA to dsDNA at any given force (obtained as the area under experimental force-extension curves). So $W(F)-T\Delta S$ represents the activation energy needed to transition between closed to open fingers configuration and the other way around.

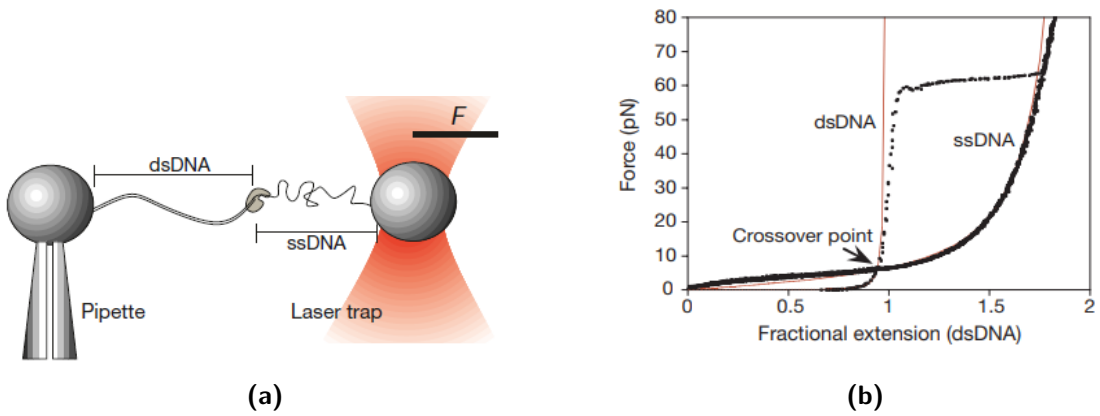

Figure 1-12: (a) Optical trap setup used to measure the replication rate dependence on the applied force. (b) The Force–extension curve for the hybrid chain consists of both ssDNA and dsDNA (dotted lines). The wormlike chain model (solid lines) fits the ssDNA and dsDNA with a persistence length of 0.7 nm and 53 nm, respectively. Adapted from [87].

Equation 1-6 is mainly used to fit the data obtained with experiments since many parameters are unknown and hard to determine in practice. In practice, the replication rate is determined by the elongation of the DNA chain during the replication process. This DNA chain will consist of both ssDNA and dsDNA. A plot of the force-extension curve for such a hybrid chain is obtained by Wuite et al. and shown in Figure 1-12b. Smith et al. have shown that for such a hybrid chain, the force-extension curve is a linear combination of the purely ssDNA and dsDNA force-extension curves [72]. With this knowledge Wuite et al. [87] determined the remaining ssDNA bases at time t, $N_{ss}(t)$ with the following equation:

$$N_{\mathrm{ss}}(t) = \frac{x_{\mathrm{meas}}(F,t) - x_{\mathrm{ds}}(F)}{x_{\mathrm{ss}}(F) - x_{\mathrm{ds}}(F)} N_{\mathrm{tot}} \tag{1-7}$$

Where $x_{meas}(F,t)$ represents the end-to-end distance of the whole DNA chain at force F (in m), N_{tot} the total number of bases in the DNA chain, x_{ds} and x_{ss} represents the end-to-end distance of fully double- and single-stranded DNA (in m) at force F, respectively.

With the derivative of Equation 1-7 with respect to time, one can determine the instantaneous replication rate as shown in the lower curve in Figure 1-13 a. In this curve, one can observe a burst in replication rate. This happens due to the activity corresponding to a different DNA polymerase binding, polymerizing, and falling off the template [11]. The upper curve in this figure corresponds to the fraction of ssDNA left in time, so since it is decreasing in time, one can verify that the ssDNA is indeed converted to dsDNA. In Figure 1-13 b one can see the replication rate for different values of n (from Equation 1-5) fitted with Equation 1-6.

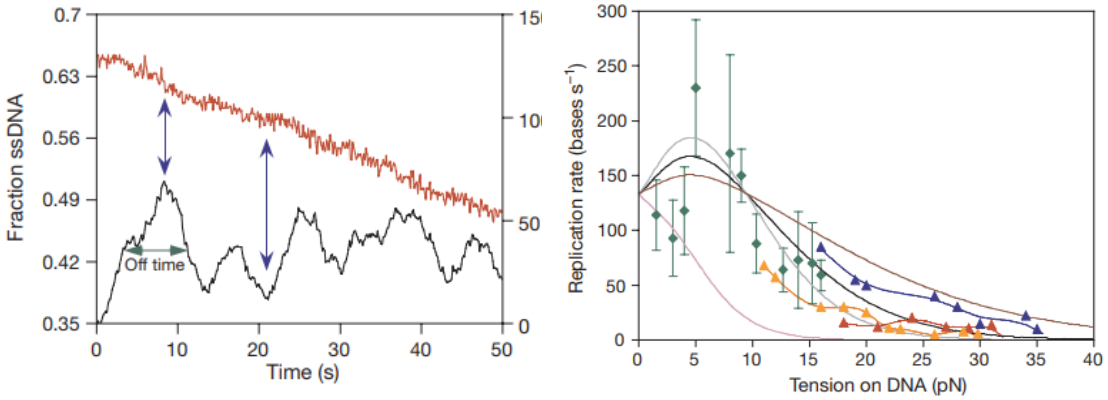

Figure 1-13: (a) The upper curve represents the conversion of ssDNA to dsDNA plotted as a fraction of ssDNA left in the template versus time. The Lower curve gives the polymerization rate obtained with the derivative of the upper curve (and choosing the right sign) and smoothing it with a moving-average filter to reduce Brownian noise. (b) The replication rate plotted against the template tension. The diamonds represent 50 polymerization bursts taken at 11 different tensions (the error bar represents the standard deviation), and the triangles represent fits of the successive replication bursts derived at constant end-to-end distances till stalling is reached. Thick lines represent fits using Equation 1-6 and Equation 1-5, where a = 0, k_0 = 130 bases per second for all the lines except the purple line. With values of n = 1 (brown), n = 2 (black), n = 3 (grey) and a = 1 nm, n = 2 (purple). Adapted from [87].

1-2-3 Results of available trapping devices

The acoustic tweezer built by Sitters et al. [71] has the closest properties to the chip discussed in this report. A plot of the force-extension experiment obtained from their device is shown in Figure 1-14.

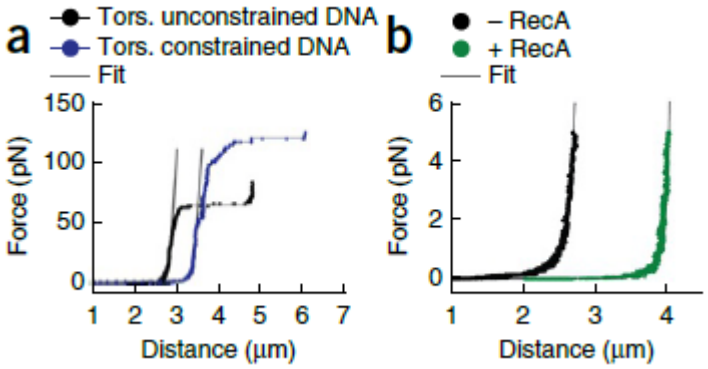

Figure 1-14: DNA elasticity measurements measured with an acoustic tweezer. (a) Force-extension curve for both torsionally constrained and unconstrained DNA chains with lengths of 10.1-kilo base pairs (kbp) and 8.4-kbp, respectively. (b) Stretching curves of an 8.4-kbp DNA molecule measured with or without 1 μM RecA. Adapted from [71]

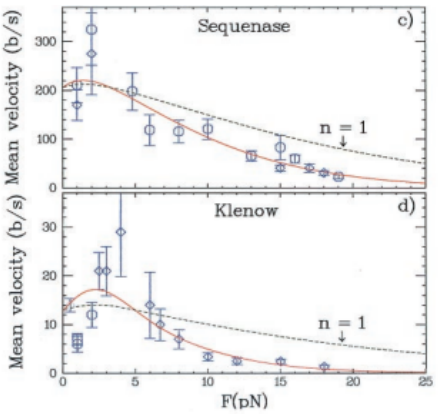

Figure 1-15: Mean replication rate of two different proteins Sequenase and Klenow plotted against applied template force F (c) Plot of the mean replication rate of Sequenase, where the circles represent the experimental data points with their standard deviation and the red curve is a fit using Equation 1-8 with optimized parameters, and the black dashed curve is a fit with the same equation but with initially assumed parameters (d) Plot of the mean replication rate of Klenow, where the diamonds represents the experimental data points, and its legs represent its standard deviation. The red and dashed black curve also represents the optimized and initial fit of the data points using Equation 1-8. Adapted from [57]

Sitter et al. did not measure the dependency of the replication rate on the applied force directly. However, they have conducted experiments on how protein binding affects the stiffness of the DNA chain.

Earlier experiments performed by B. Maier et al. with a magnetic tweezer directly showed the dependency of replication rate on the applied force for different proteins, as seen in Figure 1-15. This figure shows the replication rate expressed in base pair per second (b/s). The size of a DNA base pair is typically 0.34 nm for a double-stranded DNA [24]. In order to obtain the replication rate, the authors measured the elongation of the DNA chain during the replication process. With this value, they were able to determine the amount of replicated bases and the derivative of this is equal to the instantaneous replication rate as is explained in subsection 1-2-2. The authors fitted the replication rate with the Arrhenius law [57], which reads as:

$$\langle v(F) \rangle = v_0 \exp\left(-nF\Delta h / k_{\mathrm{B}}T\right) \tag{1-8}$$

Where n represents the minimum number of contracted bases during the polymerization rate-limiting step, F is the applied force, Δh is the difference in the distance between successive bases in ssDNA and dsDNA and k_B the Boltzmann constant. Note that this law is closely related to Equation 1-6.

1-3 Relevance

Since the discovery of the Deoxyribonucleic acid (DNA) by Swiss chemist Friedrich Miescher [67], a lot of research has been conducted to understand its dynamics and replication process. The DNA replication process is a fundamental process of life. The primary function of the replication process is to build protein to grow and repair damaged tissues. However, this process is prone to error and can lead to mutations and various diseases such as cancer [16]. Gaining more insight into the replication process is therefore of vital importance and may lead to developing medicine for diseases that are incurable today.

Over the last 60 years, biochemists have been able to qualitatively describe the replication process and identify the components responsible for the replication. However, a quantitative understanding of this process's dynamics and mechanical principles is still missing [9].

Single-molecule localization microscopy (SMLM), as well as single-molecule manipulation methods, have allowed scientists to study the trajectories of the individual molecules [88] and measure the forces during the replication process [24] [29].

Currently, AFS is gaining increasing attention. AFS is a particle manipulation technique that uses acoustic waves generated with a piezoelectric actuator to exert force on microparticles. Its increasing popularity is gained due to its high throughput capability, cost-effectiveness, non-invasiveness and applicability to a wide range of particles [62]. Especially the high throughput capability is of significant importance since the dynamics of the replication process are widely considered a stochastic process [43], it can provide scientists with statistically significant data.

1-4 Objective

AFS has many advantages over existing single-molecule manipulation techniques due to its multiplexing capability. However, one major roadblock hinders access to this technique:

price. Therefore, the thesis project aims to design, build and characterize an easy-to-build, cost-effective acoustic tweezer. By utilizing ordinary build materials and techniques, the price of an acoustic tweezer can be reduced significantly, allowing anyone interested in this topic to perform experiments. Widespread access to particle manipulation methods such as the one described in this thesis can help accelerate the understanding of biological processes. The objectives are specified more accurately below:

- Price of chip below €1050 [55]
- Deliver force up to 120 pN on a 4.5 μm polystyrene bead attached to a 10 μm DNA strand [82], [71], [90].
- Trap multiple beads simultaneously.
- Trap micro-beads between 1 and 20 μm [52].
- Bottom/Matching layer made of glass with a thickness of 170 μm. Adaptable to super-resolution imaging due to incorporation of standard thickness coverslips.

1-5 Outline of thesis

The current chapter briefly introduced acoustic tweezers and their relevant applications in biology. In chapter 2, the chip design and simulation with both finite element method (FEM) and the analytical model will be described. It describes in detail the design requirements, optimum chip design, piezo selection, simulation results, channel width and usable range of bead sizes. In chapter 3, the fabrication of the AFS chip is described for the laser micro-machined chip, and chapter 4 describes the fabrication, operation instructions and results of the double-sided tape chip. In chapter 5, the simulated trap stiffness, setup, image analysis approach, calibration sample, trapping stiffness derivation, and error propagation will be discussed, and the results will be presented in a HardwareX format. This thesis will end with a summary of the main findings, recommendations for future research and an outlook in chapter 6.

Chapter 2

Chip design & Simulations

This chapter discusses the chip design requirements, optimum layer thicknesses, channel width, piezo selection, simulation results and comparison and suitable bead sizes. An optimum design is derived from available theory on the design of standing wave resonators. This design will be analyzed with the circuit equivalent model (Krimholtz, Leedom and Matthae model (KLM)) and compared with the finite element model built with COMSOL Multiphysics 5.6. The limitations of the models are also discussed.

2-1 Requirements

Before a design can be devised, one must first set specific requirements to be met. The requirements follow from the restrictions and opportunities available at the university and the properties of DNA strands.

The design requirements for the AFS device can be summarized as follows:

- Deliver force up to 120 pN on a 4.5 μm bead attached to a DNA strand
- Trap multiple beads simultaneously
- Bottom/Matching layer made of glass with a thickness of 170 μm
- DNA strand with a length around 10 μm
- Cost-effective

2-2 Optimum layer thicknesses

The choice of material and thickness of each layer is of significant importance in designing a powerful layered resonator [52]. The material for the chip is chosen to be made of glass because

of its high-quality factor. This means that the layers of the chip exhibit less acoustic energy attenuation. Furthermore, glass is transparent, which is important for imaging purposes.

Since the material is already chosen, the main aspect of this section is to focus on optimizing the layer thicknesses. Hawkes et al. showed with simulations that in order to get as powerful resonance as possible [34] for a half wavelength layered resonator, the thicknesses of the layers should satisfy the following rule of thumb:

$$\begin{aligned} h_f &= \frac{\lambda_f}{2} \\ h_t &= \frac{\lambda_{g1}}{4}(2n_t + 1) \\ h_b &= \frac{\lambda_{g2}}{4}(2n_b + 1) \end{aligned} \tag{2-1}$$

Moreover, by using the standing wave equations and requiring the chip to be in resonance as described in the equation below:

$$f_f = f_t = f_b = f = \frac{c_f}{\lambda_f} = \frac{c_{g1}}{\lambda_{g1}} = \frac{c_{g2}}{\lambda_{g2}} \tag{2-2}$$

Where h_f represents the fluid height (in m), h_t the height of the top layer, h_b the height of the bottom layer (in m), λ_f the wavelength in the fluid layer (in m), λ_{g1} the wavelength in glass 1 (in m), λ_{g2} the wavelength in glass 2 (in m), n_t the number of nodes in the top layer, n_b is the number of nodes in the bottom layer, c_f the speed of sound in the fluid layer (m/s), c_{g1} the speed of sound in glass 1, c_{g2} the speed of sound in glass 2 (in m/s), f the resonator frequency and f_t, f_b and f_f represents the frequency in the top layer, bottom layer and fluid layer (all in Hz), respectively.

Since the channel will be cut in the top glass layer, there is an additional geometric relationship:

$$h_t = 1 \cdot 10^{-3} - h_f \tag{2-3}$$

The parametric model described in this section is shown in Figure 2-1. In this case, the value SW is equal to zero since the angle of the sidewalls is not considered in this section.

Known constants:

$$\begin{aligned} n_b &= 0 \\ c_f &= 1480 \text{ m/s} \\ c_{g1} &= 5403 \text{ m/s} \\ c_{g2} &= 5389 \text{ m/s} \\ \alpha &= 0^o \\ h_b &= 170 \ \mu\text{m} \end{aligned} \tag{2-4}$$

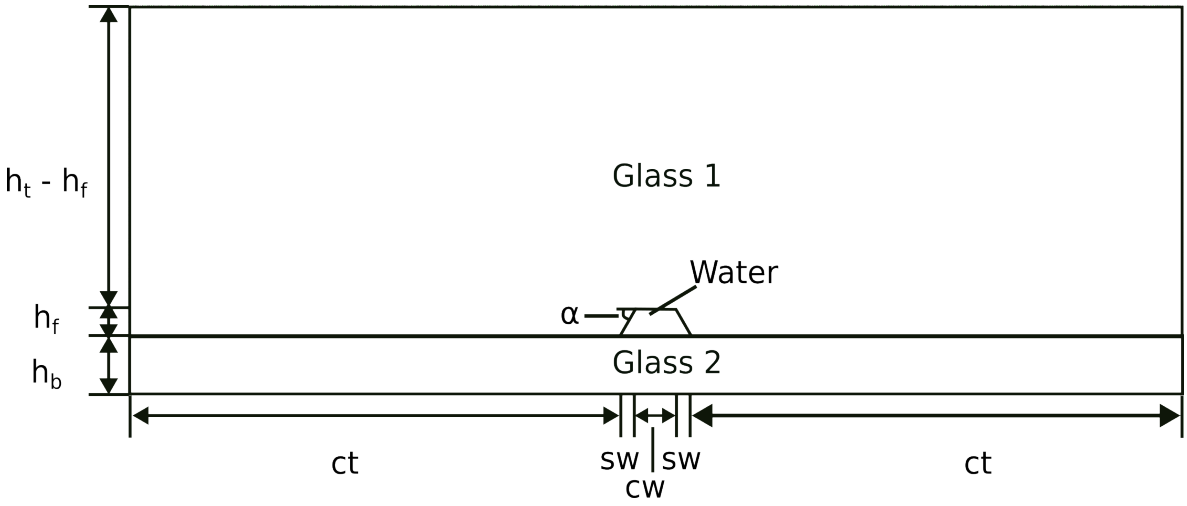

Figure 2-1: Parametric chip model for design optimization.

With these constants, one can derive the frequency and the optimal height/thicknesses for each layer to be:

$$\begin{aligned} f &= 7.93 \text{ MHz} \\ h_f &= 93 \ \mu\text{m} \\ h_t &= 907 \pm 50 \ \mu\text{m} \\ h_b &= 170 \pm 10 \ \mu\text{m} \end{aligned} \tag{2-5}$$

However, the top and bottom glass have uncertainties in thickness that can influence the optimum fluid height as indicated in Equation 2-5. Therefore, a parametric sweep in COMSOL is used to explore this uncertainty's effect on the chip's eigenfrequency and the corresponding acoustic pressure field. It turns out that by keeping the fluid layer at 93 μm, the variation in the eigenfrequency is less than 0.15 MHz, and the magnitude of the acoustic pressure stays within the same order.

P. Glynne-Jones et al. [31] conducted a sensitivity analysis on the thickness of the top glass layer and showed that the optimum design is not sensitive to variation in thickness. Hill et al. [37] showed that the peak energy density in the fluid layer barely change if the thickness divided by the wavelength of the acoustic wave in the fluid layer changes slightly.

2-3 Channel width

According to Spigarelli et al. [74], high trapping stiffness can be obtained with high aspect ratio channels for rectangular geometries. The aspect ratio is the ratio between the channel's height and width (H/W). The authors showed that the trapping capability increased for higher aspect ratio channels.

For bead diameters above 1 μm, an aspect ratio of 1 is sufficient to trap and focus all particles in the center of the channel. This is the case because the influence of acoustic streaming near the top and bottom walls is reduced, and the acoustic radiation force becomes dominant.

However, a high aspect ratio also means that the side walls will have more influence on the trapping capability. In addition, the sidewalls can considerably impact the trapping capability, as shown by P. Glynne-Jones et al. [31] and Ponsen et al. [66]. Therefore an aspect ratio of 0.5 is used for the laser micro-machined chip, which should be able to capture more than 80 percent of all particles [74]. The width of the channel for the double-sided tape chip is based on the chip developed by Sitters et al. [71], which is equal to 2 mm.

2-4 Piezo selection

As a first-order approximation, the standing wave equations for longitudinal waves in a tube with two close ends are used to determine the required driving frequency to generate the required acoustic pressure nodes. The standing wave equations are described by [78]:

$$\begin{aligned} \lambda_n &= \frac{2}{n}h \\ f_n &= \frac{v}{\lambda_n} \\ n &= 1, 2, 3, ... \end{aligned} \tag{2-6}$$

Where λ_n represents the wavelength of the n-th order harmonic (in m), h represents the fluid layer thickness (in m), f_n represents the driving frequency for the n-th order harmonic (in Hz), and v is the speed of sound the media where the acoustic wave goes through (in m/s).

For the chip design discussed in section 2-2, it was calculated with the standing wave equations that the required driving frequency for the first harmonic is equal to 7.93 MHz. This means that the selected piezoelectric transducer needs to have a thickness resonant frequency around this value.

The available amplifier also constrains the choice of the piezoelectric transducer. The amplifier available at the university can provide a maximum current of 1A for a 40 V power supply. And the average current required (I_a) by a piezoelectric transducer can be calculated with:

$$\begin{aligned} I_a &\approx f \cdot C \cdot V_{pp} \\ &=_t \cdot C \cdot V_{pp} \\ &= 8 \cdot 10^6 \cdot 0.992 \cdot 10^{-9} \cdot 37 \\ &= 0.29 \end{aligned} \tag{2-7}$$

Where f is the driving frequency of the transducer (in Hz), C is the electrical capacitance of the transducer (in F), V_{pp} is the peak-to-peak voltage applied (in V) to the transducer and ω_t the thickness resonant frequency of the transducer.

In Table 2-1, the parameters of the chosen piezo are listed. By applying Equation 2-7 on this piezo, one can deduce that the maximum V_{pp} that can be applied is equal to the maximum peak-to-peak voltage the amplifier can handle, which is around 37 V_{pp}. That is more than enough for trapping purposes.

Table 2-1: Transducer parameters from [76].

Parameters	value	unit
Material	PIC255	-
thickness	0.25	mm
length	5	mm
width	5	mm
Q_m (quality factor)	80	-
$tan(\beta)$ (dielectric loss)	0.02	-
h_{33} (piezo constant)	$1.18 \cdot 10^9$	V/m
permittivity	$1.638 \cdot 10^{-8}$	C/(V m)
speed of sound	4485	m/s
density	7800	kg/m^3
C (Electrical capacitance)	0.992	nF
f_t (Thickness resonant frequency)	8	MHZ

2-5 Simulations

2-5-1 Material properties

Before any simulations can be conducted, first, one needs to obtain the material properties of each layer. The material properties of all layers except the piezo ceramic are tabulated in Table 2-2

Table 2-2: Layer material properties. Values indicated with * are derived with $c = \sqrt{\frac{E}{\rho}}$ from [48]. Values indicated with ^{m} mean measured values. Values indicated with ^{c} means obtained from COMSOL library

Material property	Units	Aluminium	Top glass	Fluid layer	Bottom glass	Tape[20]
Thickness	mm	0.02^m	$1^{[42]}$	0.1	$0.17^{[83]}$	0.1^m
Width	mm	5	5	2	5	3
Density, ρ	kg/m^3	$2700^{[2]}$	$2500^{[81]}$	$1000^{[44]}$	$2510^{[41]}$	1190^c
Poisson's ratio, ν	-	$0.35^{[25]}$	$0.23^{[81]}$	-	$0.208^{[41]}$	0.35^c
Young's Modulus, E	GPa	$70^{[25]}$	$73^{[81]}$	-	$72.9^{[41]}$	3.2^c
Speed of sound, c	m/s	5091.8*	5403.7*	$1480^{[44]}$	5389.2*	1639.8*
Quality factor, Q	-	$230^{[71],[44]}$	$230^{[71],[44]}$	$230^{[71],[44]}$	$230^{[71],[44]}$	-

2-5-2 Analytical analysis

The KLM model [49], also known as the equivalent circuit model, is used to analyze the chip performance by calculating the pressure fields in the fluid as well as the acoustic radiation force on the bead. This model assumes that a circuit can model the behaviour of a piezoelectric actuator. The intuition behind the circuit equivalent model is described in section A-1. Subsequent layers of the layered resonator will be modelled as additional impedance on the piezo. The impedance of the layers can be derived with the equations provided by Kinsler et al. [48]. When the impedance of each layer is known, one can calculate the force on each layer boundary, and subsequently, the velocity $v(x)$ (in m/s) and pressure field $p(x)$ (in Pa) in the fluid layer [36],[38]. These velocity and pressure fields are then substituted into the 1D equations for the acoustic radiation energy and force as is shown below [70]:

$$U^{rad} = V_p \left(\frac{1 - \kappa_p/\kappa_f}{4} \kappa_f |p(x)|^2 - \frac{3}{4} \left(\frac{\rho_p/\rho_f - 1}{2\rho_p/\rho_f + 1} \right) \rho_f |v(x)|^2 \right) \tag{2-8}$$

$$F^{rad}(x) = -\nabla U^{\mathrm{rad}}(x) \tag{2-9}$$

Where V_p is the volume of the bead (in m^3), κ_f and κ_p represent the compressibility of the fluid and bead (in m^2/N), respectively, and ρ_f and ρ_p the density of the fluid and bead (in kg/m^2), respectively, U^{rad} is the potential (in Nm), and F^{rad} is the radiation force in the

fluid layer (in N). This model is implemented in MATLAB by Kamsma et al. and is freely available [44]. From this code, a user-friendly user interface can be called and used to study different flow cell designs. Using this interface, one can observe that the applied frequency will influence the number and position of the nodal points. Furthermore, by changing the amplitude of the voltage, one can change the amplitude of acoustic radiation force and, therefore, the trapping stiffness. This model is used to plot the analytical acoustic pressure field and acoustic radiation force profile in Figure 2-6a and Figure 2-6b.

2-5-3 Finite Element Analysis

In COMSOL Multiphysics 5.6, two different chips are modelled. These chips are shown in Figure 2-2. The chip shown in Figure 2-2a represents the chip with a laser cut channel, and the chip shown in Figure 2-2b represents the chip with double-sided tape channels.

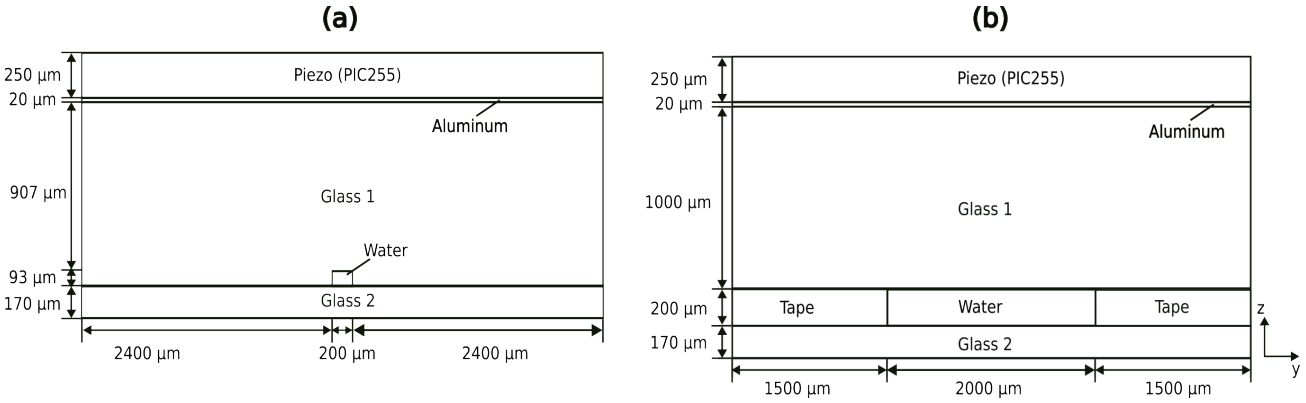

Figure 2-2: (a) COMSOL model of laser cut channel chip. (b) COMSOL model of double-sided channel chip.

The materials glass 1, glass 2, tape and the aluminium layer are considered linear elastic solid materials. And the piezo is modelled as a transversely isotropic material with an axis of symmetry using the constitutive relation for piezoelectric material in the strain-charge form, which reads as:

$$\begin{aligned} S &= s_E T + d^T E \\ D &= dT + \epsilon_0 \epsilon_{rT} E \end{aligned} \tag{2-10}$$

Where S represents the strain applied to the piezoelectric material, s_E is the compliance (in m^2/N) of the material under constant or zero electric field E, d the coupling matrix (in $\mathrm{m/V}$) that is equal to the partial derivative of the strain S with respect to the electric field E for constant or zero stress T (in $\mathrm{N/m}^2$), D the charge displacement (in $\mathrm{C/m}^2$) and ϵ_{rT} the relative permittivity of the material for constant or zero strain and ϵ_0 is the vacuum permittivity ($\mathrm{F/m}$).

The following material properties are inserted into COMSOL for the piezo chip made from piezoceramic material PIC255 [26]:

$$s_E = \begin{bmatrix} 1.38 \cdot 10^{-11} & -5.699 \cdot 10^{-12} & -7.376 \cdot 10^{-12} & 0 & 0 & 0 \\ -5.699 \cdot 10^{-12} & 2.17 \cdot 10^{-11} & -7.376 \cdot 10^{-12} & 0 & 0 & 0 \\ -7.376 \cdot 10^{-12} & -7.376 \cdot 10^{-12} & 2.17 \cdot 10^{-11} & 0 & 0 & 0 \\ 0 & 0 & 0 & 4.492 \cdot 10^{-11} & 0 & 0 \\ 0 & 0 & 0 & 0 & 4.492 \cdot 10^{-11} & 0 \\ 0 & 0 & 0 & 0 & 0 & 4.319 \cdot 10^{-11} \end{bmatrix}$$

$$d = \begin{bmatrix} 0 & 0 & 0 & 0 & 5.35 \cdot 10^{-10} & 0 \\ 0 & 0 & 0 & 5.35 \cdot 10^{-10} & 0 & 0 \\ -1.74 \cdot 10^{-10} & -1.74 \cdot 10^{-10} & 3.94 \cdot 10^{-10} & 0 & 0 & 0 \end{bmatrix}$$

$$\epsilon_{rT} = \begin{bmatrix} 1649 & 0 & 0 \\ 0 & 1649 & 0 \\ 0 & 0 & 1750 \end{bmatrix}$$

The movement of the solid glass and fluid layers is coupled using the acoustic structure boundary option in the multiphysics tab. The pressure field in the fluid can be calculated by selecting the fluid layer to be the pressure acoustics domain. Then, the voltage is applied on top of the piezo surface. All the relevant boundary conditions are shown in Figure 2-3.

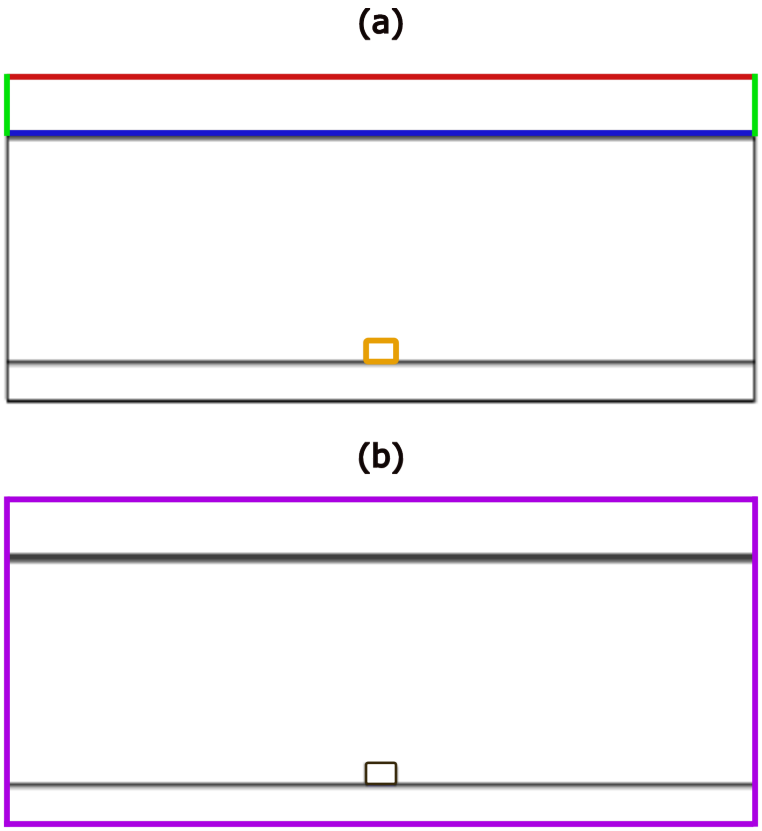

Figure 2-3: The boundary conditions used in the COMSOL FEM models. (a) Boundary conditions for the piezoceramic material are: red = 10 V, blue = ground, green = zero charge, and the orange boundary conditions represent the multi-physics acoustic-structure boundary condition derived from [19]. (b) The magenta boundary represents the free boundary condition in the solid mechanics domain derived from [23].

By applying a 20 peak-to-peak voltage (V_{pp}) to the piezo ceramic material and performing a frequency domain study by setting the frequency equal to the eigenfrequency of the pressure acoustics domain, one will obtain the pressure field in the fluid layer as is shown in Figure 2-4.

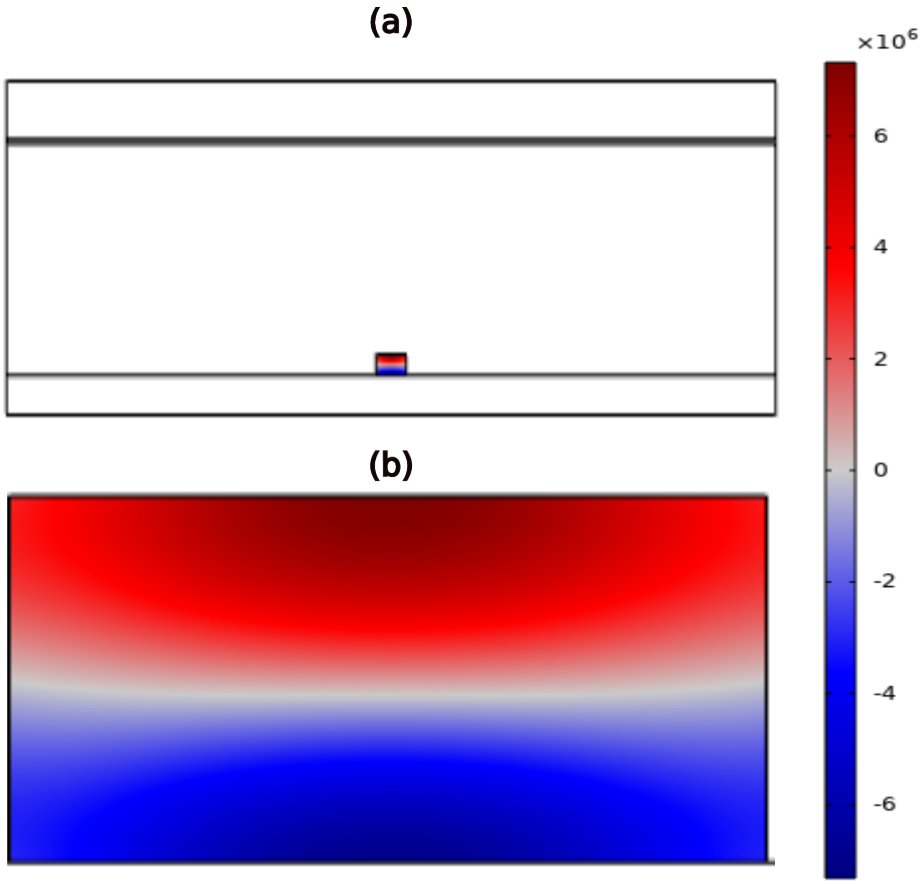

Figure 2-4: (a) Whole chip with the calculated pressure field in the fluid layer for 20 V_{pp} excitation of the piezo ceramic with a frequency of 7.9648 MHz. (b) Zoomed in image of the pressure field in the fluid layer.

The acoustic radiation force on a 1.5-micron polystyrene bead can be obtained by utilizing the particle tracing module in COMSOL and adding the fluid particle interaction option in the multiphysics tab. First, the data points are obtained by releasing ten evenly spaced particles in a vertical line through the middle of the channel, as shown in Figure 2-5, satisfying the sampling theorem at ten times the highest frequency [27]. Next, these 10 data points are fitted with a sine function to obtain the acoustic radiation force profile in the middle of the channel as shown in Figure 2-6b.

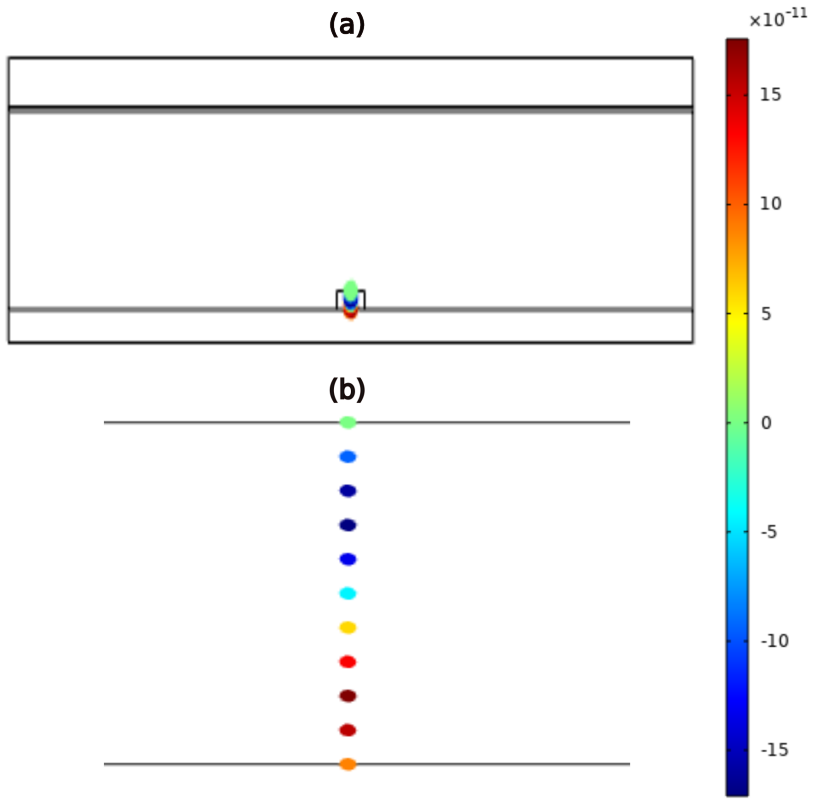

Figure 2-5: Derivation of radiation force in the middle of the channel for 20 V_{pp} excitation and frequency of 7.9648 MHz

2-5-4 Model comparison and limitations

In this section, the analytical model described in subsection 2-5-2 will be compared with the numerical model described in subsection 2-5-3. This comparison is made on the laser-cut microchip shown in Figure 2-2a since the analytical model assumes a microchannel to be etched on glass.

The pressure profile for the FEM model is obtained by evaluating the pressure along a vertical line in the middle of the fluid channel shown in Figure 2-4b. Derivation of the acoustic radiation force for the FEM model is described in subsection 2-5-3

In Figure 2-6, one can deduce that the analytical and finite element model show comparable results for the pressure field, acoustic radiation force on the bead and the eigenfrequency. The boundary effects of the sidewalls cause the difference in trapping position and amplitude. The boundary effect will slightly distort the pressure field, as shown in Figure 2-6. The analytical model is a 1D model and is, therefore, unable to capture any boundary effects and lateral resonances within the various layers.

The finite element model can also simulate non-ideal situations like weaker acoustic pressure

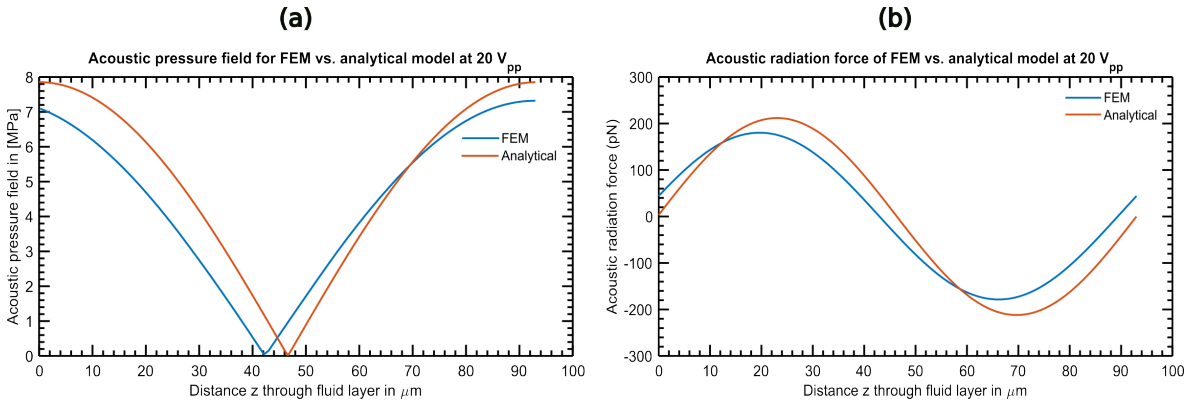

Figure 2-6: (a) Comparison of the acoustic pressure field for the half wave mode and 20 V_{pp} excitation between the analytical (at 7.936 MHz) and FEM model (at 7.9648 MHz). (b) Comparison of the acoustic radiation force on a 1.5-micron bead between the analytical (at 7.936 MHz) and FEM model (at 7.9648 MHz) with excitation of 20 V_{pp}

fields near the edges of the flow cell, as described by P. Glynne-Jones et al. [31]. P. Glynne-Jones et al. [31] also mentioned that the channel width causes width-wise variation in focusing force and acoustic node position. It will also cause particles to form into bands. Moreover, it can simulate a chip with a double-sided tape channel, which is impossible with the analytical model since it assumes the channel is etched in the glass. Therefore, the FEM model will be used for all the following chapters. However, in both models, the glue layers are neglected. Therefore the results may deviate from the experimental results, and both models are unable to capture microbubbles trapped in the tape during fabrication.

Also, the tilt and decenter of the piezo chip can cause discrepancies between the simulation and experiments since the displacement of a piezoelectric transducer is not uniform. The displacement is higher at the center [69]. This means that if the center of the piezo is close to the tape layer, it may be damped more, and the tilt due to nonuniform glueing layer thickness can increase the deviation between the model and experiments. The solder on top of the piezo causes another discrepancy between the model and experiments.

Also, all the materials, including the double-sided tape, are assumed to be homogeneous linear elastic materials. However, Tiwari et al. [79], and Sönnerlind [77] showed that more complex models are needed to represent the glueing layers accurately.

2-6 Bead size

Another essential variable is the properties of the bead and especially the diameter of the bead. As seen in the Equation 2-8, the radiation force on the bead depends on its volume and compressibility. A practical range of bead sizes used with a layered resonator is between 1 μm to 20 μm [52]. If the bead is too small viscous drag from acoustic streaming starts to dominate, and if the bead is too large, sedimentation may occur due to the dominant gravity force. The finite element model described in subsection 2-5-3 can be used to analyze the trapping performance of different beads.

Chapter 3

Fabrication

This chapter discusses the fabrication of the chip designs described in chapter 2. First, we will discuss the fabrication of the laser-cut channels by selecting the relevant parameters and describing how to obtain the relevant channel properties for evaluation. Then the Taguchi orthogonal design array is used on the nanosecond and femtosecond laser cutter to find the optimum process parameters and minimize the number of required experiments. These process parameters should minimize the surface roughness of the channel and the roughness at the edges. Hereafter we will look into the fabrication of the inlet and outlet and the limitations of this fabrication process.

3-1 Laser micro-machining

Laser micro-machining is chosen to fabricate the microchannels in glass. This method is cost-effective and time-efficient compared to traditional photolithography processes. Furthermore, since our objective is to reduce the price of the acoustic tweezer, laser micro-machining is a suitable fabrication method.

A general setup using laser micro-machining to produce microchannels in glass is shown in Figure 3-1. The laser head will send a laser beam toward the Galvanometer through precisely aligned mirrors. The Galvanometer will move at speed specified by the user. This speed is often referred to as the laser speed or just speed in this report. The laser beam is not continuous, but it is made up of fast pulses, and the frequency of the pulses is known as the pulse rate or laser firing rate. The stage on which the substrate rests can also move, but it is best to allow the Galvanometer to move since that is more precise. In order to avoid the movement of the stage, the working area needs to be restricted to 40 by 40 mm for the laser cutters available at the university.

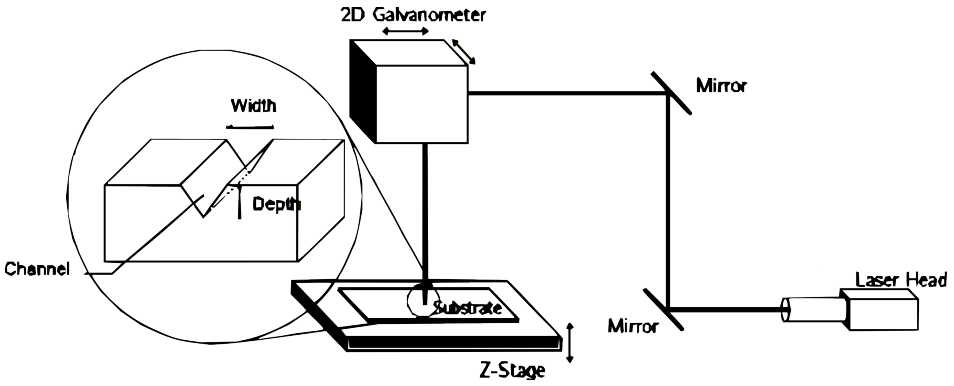

Figure 3-1: Setup of laser micro-machining for the fabrication of microchannels. Adapted from [60].

3-2 Laser process parameters

The main objective for selecting process parameters is to find parameters with the most significant influence on the surface roughness and roughness at the edges of the channel. The surface roughness of the channel is important since Lei et al. [51] showed that surface roughness of a few microns could significantly enhance the inner streaming vortex velocity. This can be problematic for DNA-tethered microbead experiments close to the chip surface. Moreover, Sitters et al. [71] showed that surface roughness of less than 1-nanometer negligible effect on the generated radiation forces. The channel edge roughness is important since rough edges can lead to leakage since height differences in the edges can mess up the bonding between the top and the bottom glass layer.

The most relevant process parameters for the channel height, surface, and edge roughness of the fluid channel found in literature [60] and derived with own experiments are the repetitions/number of passes, laser speed, laser pulse frequency, hatching pitch and the laser power. So these are the parameters that will be optimized.

The laser speed is the speed at which the 2D Galvanometer is moving. The 2D Galvanometer guides the laser beam towards the substrate as shown in Figure 3-1, which is equivalent to the laser scan speed in Figure 3-2. The hatching pitch represents the distance between the subsequent cut lines, equivalent to the hatch distance shown in Figure 3-2.

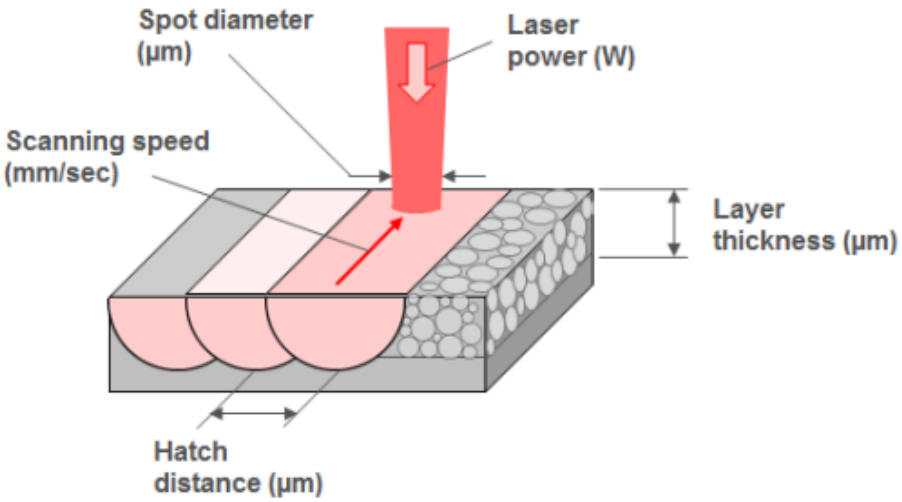

Figure 3-2: Laser micro-machining parameters

3-3 Channel properties evaluation

The channel properties of the laser-cut channels, such as the channel height, surface roughness and channel edge roughness, are all derived with a digital microscope from the manufacturer Keyence (model VHX-6000).

The height of the channel is evaluated in the middle of the channel. The channel profile can be derived along a defined line using the digital microscope. The reason for choosing the middle of the channel is that it is far away from the drilled holes, so the channel roughness is less.

The edge roughness of the channel can also be evaluated using the digital microscope. The arithmetical mean height along a line, Ra, is used to measure the roughness of the edges of the channel.

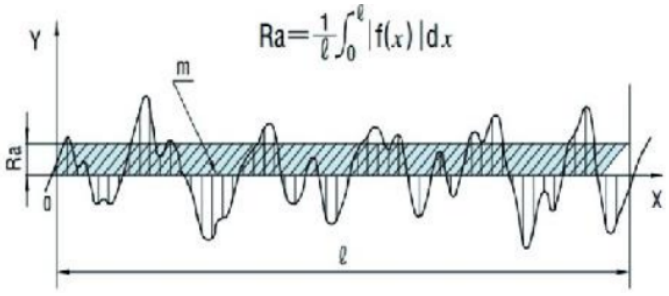

Figure 3-3: Illustration of the arithmetical mean height along a line (Ra) from [50]

The surface roughness is evaluated using the arithmetical mean height (Sa). This is an extension of the arithmetical mean height along a line. This parameter is generally used to evaluate surface roughness, and its principle is shown in Figure 3-4. This parameter represents the mean height away from the mean plane and is evaluated using a surface integral over the

whole mean plane. To get the roughness of the channel, a polygon or rectangle is drawn on the bottom of the channel, over which the optical microscope calculates the surface roughness. It is essential to exclude the edges of the channel since these are located at a different plane. Another approach to evaluating the surface roughness is to determine the power spectral density of the surface of interest, as shown by Y. Gong et al. [33]. This can lead to a more accurate measure of surface roughness. However, as long as the limitations of the arithmetical mean height evaluation are taken into accounts, such as its inability to distinguish between surface roughness due to angled sidewalls and surface roughness due to peaks and troughs, this method is more time efficient to use since it is already implemented in the software of most optical microscopes.

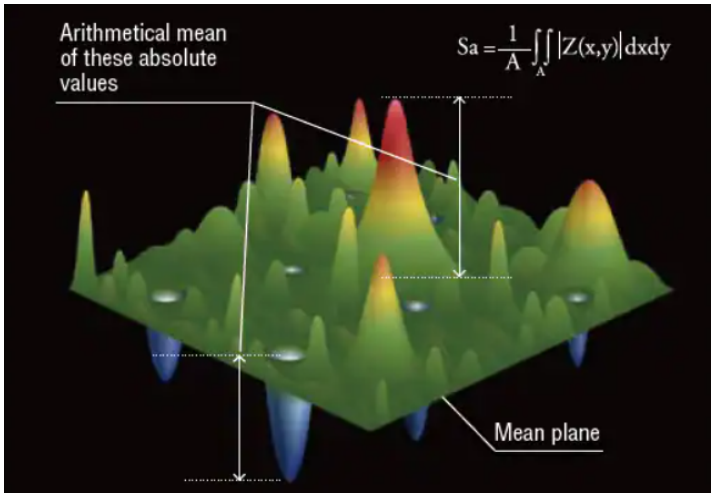

Figure 3-4: Illustration of the arithmetical mean height along a surface (Sa) adapted from [46]

3-4 Nanosecond laser microchannels

Since the femtosecond laser cutter was unavailable when the channels were needed, the nanosecond laser was used to cut the microchannels. First satisfactory values of the process parameters described in section 3-2 are found with trial and error. After that, the Taguchi orthogonal array is applied to parameter values close to it to optimize the channel properties described in section 3-3. Also, the evaluation method described in this section is used except for the channel edge roughness since the nanosecond laser induces a lot of cracks, the quality of the channel edges can be inspected with the imaging device on the laser cutter to reduce production time. The power can not be varied for the nanosecond laser since the mechanism to regulate it was broken. Instead, the current needs to be adjusted. In this case, it was decided to keep the current constant at 6.44 A, which was optimized for glass.

After many evaluations, an initial Taguchi design array shown in Table 3-1 was used to model the effect of the process parameters on the channel properties. The height of the channel and surface roughness are derived with the methods described in section 3-3.

By analyzing the Taguchi design, one can derive the effect of each process parameter on the height of the channel and the surface roughness. This is done by calculating the signal-to-noise

Table 3-1: Initial Taguchi design array. The vertical line divides this table into set values to the left and measured values to the right.

speed (mm/s)	laser firing rate (kHz)	repetitions	hatching pitch (μm)	mid channel height (μm)	surface roughness (μm)
50	50	2	5	179.97	15.62
50	100	6	10	184.56	28.1
50	130	10	15	159.91	36.59
100	50	6	15	241.58	25.8
100	100	10	5	246.96	36.89
100	130	2	10	1.60	0.000001
150	50	10	10	274.76	62.81
150	100	2	15	9.33	0.000001
150	130	6	5	1.80	0.000001
50	100	10	15	159.47	36.83

ratio. The signal-to-noise ratio for height and surface roughness are described in Equation 3-1 and Equation 3-2.

$$(S/N)_{\text{height}} = -10\log_{10}\left(\sum \frac{y^{-2}}{n}\right) \tag{3-1}$$

$$(S/N)_{\text{surface roughness}} = -10\log_{10}\left(\sum \frac{y^{2}}{n}\right) \tag{3-2}$$

Where y represents the responses for a given factor level combination and n is the number of responses in the factor level combination. Equation 3-1 increases with y and is used to find process parameters that maximize the value of y, and the reverse happens to Equation 3-2.

By analyzing the Taguchi design array using Minitab 18 (Minitab Inc., USA) software packages, the main effect plots for the channel height and surface roughness of the channel are derived and shown in Figure 3-5. This figure shows that the laser firing rate influences the channel height most, and the number of repetitions affects the surface roughness the most. This effect can be derived from the plots because the signal-to-noise ratio of the mean values of the response changes the most with these variables. All the process parameter values that provide the highest mean of the SN ratios are the best for the given response. So to get the maximum height, we need to use a speed of 50 mm/s, a laser-firing rate of 50 kHz, 10 repetitions and a hatch of 0.015 mm. From Figure 3-5, it becomes evident that to get the best values for the surface roughness, the opposite process parameter values need to be taken.

The accuracy of the Taguchi analysis is shown in Table 3-2. This table shows that the surface roughness is better captured with the Taguchi model than the channel height. This is the case since the Minitab software can not deal with a channel height of zero. This happens when the laser power is insufficient to cut through the glass and can only create a rough surface. Also, the software can not capture cases where debris and molten glass accumulate at specific locations and create the inverse of channel depth.

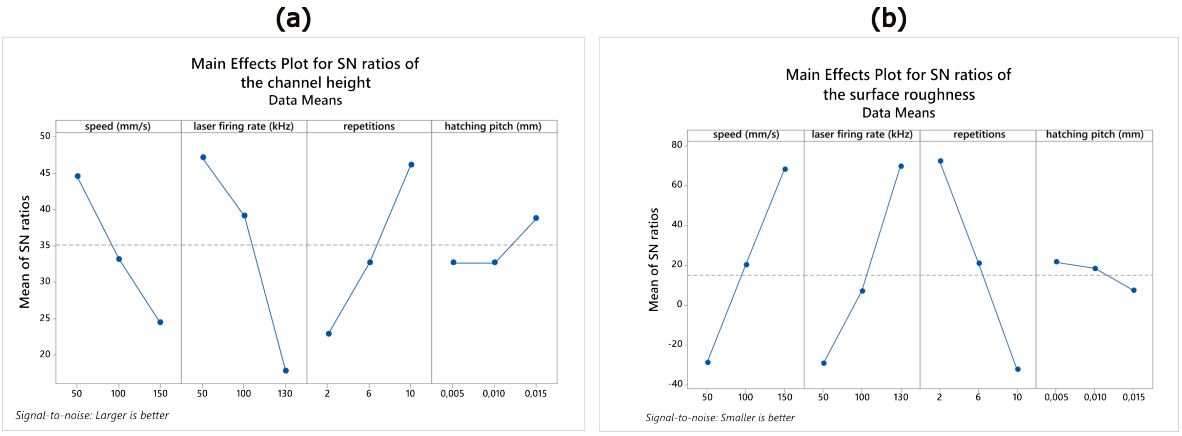

Figure 3-5: The effect plots of the process parameters on the channel height and surface roughness derived with the Taguchi design array tabulated in Table 3-1. (a) A plot of the effect of each process parameter on the channel height, the larger the value for the mean of SN ratios, the more it will increase the channel height. (b) A plot of the effect of each process parameter on the surface roughness of the channel. Large values of the mean of SN ratios will minimize surface roughness.

Table 3-2: Model performance measures of linear models derived with Taguchi method for channel height and surface roughness. The value of S represents the standard deviation of the distance between the data and the fitted values, R-sq represents the percentage of variation in the response that can be explained by the model, R-sq(adj) represents the adjusted R-sq that is adjusted for the number of predictors relative to the number of observations.

Model	S	R-sq	R-sq(adj)
Channel height	13.9958	93.43%	40.86%
Surface roughness	35.0901	97.40%	76.63%

A linear model can be fitted to the channel height and surface roughness using analysis of variance (ANOVA). These models can optimise the process parameters to minimize surface roughness while reaching a target channel height. However, since the model is not accurate, it was decided to use the data in Table 3-1 together with the knowledge obtained in Figure 3-5 to optimize these parameters further.

The best parameters found for the nanosecond laser cutter were:

$$\begin{aligned} \text{speed} &= 50 \text{ mm/s} \\ \text{laser firing rate} &= 130 \text{ kHz} \\ \text{repetitions} &= 3 \\ \text{hatching pitch} &= 5 \ \mu\text{m} \end{aligned}$$

Using the process parameters listed above, one can obtain the channel with a height of 77.57 μm and surface roughness of 16.75 μm as shown in Figure 3-6. The objective was to find parameters to get as close to the height of 93 μm as possible. This is the optimum height calculated in section 2-2.

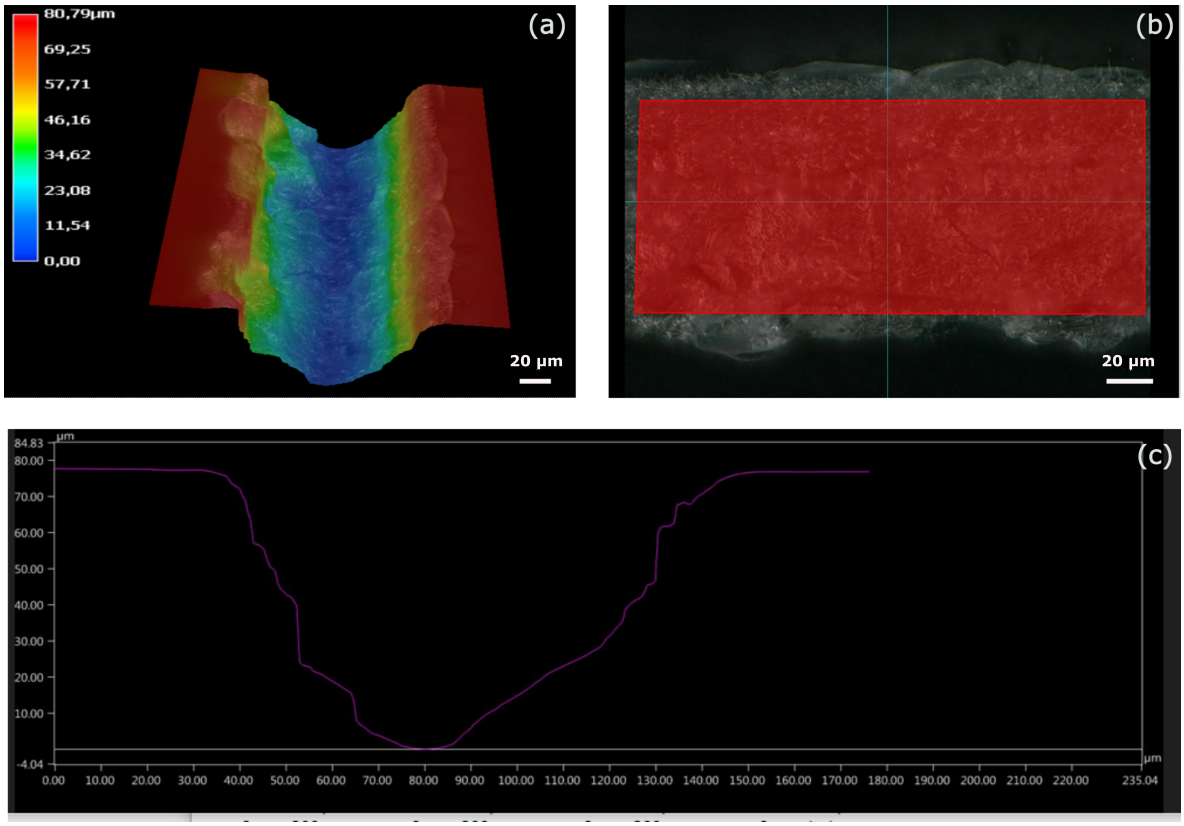

Figure 3-6: (a) Optical microscope 3D reconstruction of nanolaser cut channel with best parameters and a magnification of 1500 times, (b) Surface roughness evaluation with an optical microscope using a red rectangular evaluation plane, the obtained value for Sa is 16.75 μm. (c) The profile of the channel in the middle of the channel with a height of 77.57 μm.

The channel shown in Figure 3-6 is rough, and the channel height is not uniform. It varies from 73.66 μm to 84 μm. This can be expected since Kasaai et al. [45] and Liu et al. [53] had shown that unless modifications in the fabrication process are conducted, the nanosecond laser will be inferior to the femtosecond laser in producing microchannels. This happens since the nanosecond laser fires long and intense pulses at the glass surface that induces shock waves on the glass and creates cracks. The femtosecond laser fires short and less powerful pulses at the glass specimen, and therefore it can minimize the damage zone significantly and create much smoother channels.

The channels could be optimized further by manually tuning the process parameters. For example, combining a coarser laser run with a smoother laser run, starting with a lower laser firing rate to get rough cuts and finishing with a higher laser firing rate to smooth the cuts further. However, since the femtolaser cutter was available shortly after reasonable process parameter values were found for the nanosecond laser, it was decided to continue with the femtolaser instead.

3-5 Femtosecond laser microchannels

Due to the limited availability of the femtosecond laser during this project, a suboptimal Taguchi design array was found to optimize the laser cutting parameters. This Taguchi array is tabulated in Table 3-4. Furthermore, with this Taguchi array, the effects plot of the relevant parameters is obtained and shown in Figure 3-7.

From Table 3-3, one can deduce that the fitted linear model cannot model the edge roughness properly, and the standard deviation value for the height is large. The fitted linear model is inaccurate in predicting the channel height and edge roughness. So it was decided to select the best process parameters directly from Table 3-4. The parameters used to cut the channel are in the eighth row of Table 3-4.

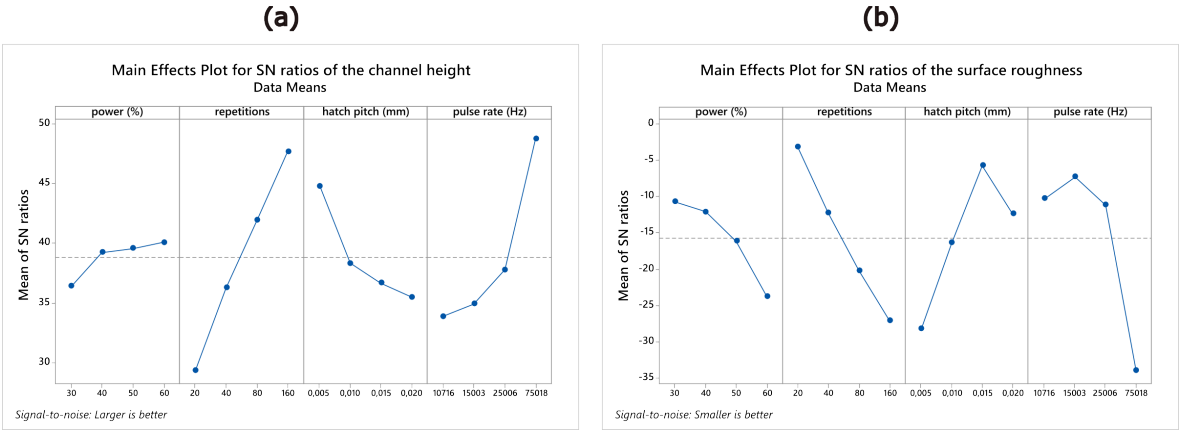

Figure 3-7: The effect plots of the process parameters on the channel height and surface roughness derived with the Taguchi design array tabulated in Table 3-4. (a) A plot of the effect of each process parameter on the channel height, the larger the value for the mean of SN ratios, the more it will increase the channel height. (b) A plot of the effect of each process parameter on the surface roughness of the channel. Large values of the mean of SN ratios will minimize surface roughness.

When these process parameters are used to cut the channels, one will obtain the channel with a height of 123.16 μm and a channel surface roughness of 0.41 μm. The channel has a uniform height, but the channel sidewalls are not perfectly straight and contain some irregularities as shown in Figure 3-8.

Table 3-3: Model performance measures of the linear models derived with Taguchi method for channel height, surface roughness and edge roughness. The value of S represents the standard deviation of the distance between the data and the fitted values, R-sq represents the percentage of variation in the response that can be explained by the model, R-sq(adj) represents the adjusted R-sq that is adjusted for the number of predictors relative to the number of observations, and R-sq(pred) describes how well the linear models can predict the response for new observations.

Model	S	R-sq	R-sq(adj)	R-sq(pred)
Channel height	35.05	99.20%	96.00%	77.23%
Surface roughness	6.65	99.70%	98.52%	91,56%
Edge roughness	1.01	83.84%	19.20%	0.00%

Table 3-4: Femtolaser Taguchi design array for fixed laser speed of 200 mm/s. The vertical line divides this table into set values to the left and measured values to the right.

power (%)	repetitions	hatch pitch (mm)	pulse rate (Hz)	mid-channel depth (μm)	surface roughness (μm)	edge roughness (μm)
30	20	0.005	10716	24.24	1.18	0.09
30	40	0.010	15003	33.50	0.94	0.01
30	80	0.015	25006	66.45	1.34	0.30
30	160	0.020	75018	358.18	94.23	0.37
40	20	0.010	25006	23.68	0.82	0.05
40	40	0.005	75018	427.10	115.08	4.56
40	80	0.020	10716	56.94	2.45	0.02
40	160	0.015	15003	122.01	1.15	1.08
50	20	0.015	75018	87.51	3.91	0.07
50	40	0.020	25006	41.45	1.13	0.02
50	80	0.005	15003	159.46	22.91	0.22
50	160	0.010	10716	142.86	16.81	0.14
60	20	0.020	15003	15.00	1.16	0.15
60	40	0.015	10716	30.56	2.33	1.17
60	80	0.010	75018	412.20	145.91	0.13
60	160	0.005	25006	553.53	139.37	0.47

3-6 Inlet and outlet

The inlet and outlet to the laser-cut microchannels are drilled through the top glass with a thickness of 1 mm. These holes are drilled using the nanosecond laser cutter used to cut channels described in section 3-4. To drill the holes, the drill tool mode was used, and the best laser settings were found to be:

- Drill numbers = 3
- Drilling step = 0.005 mm
- Number of levels = 40
- Z Start = 0 mm
- Z Step = -0.03 mm
- Group Z Drills
- Z Levels in different Layers

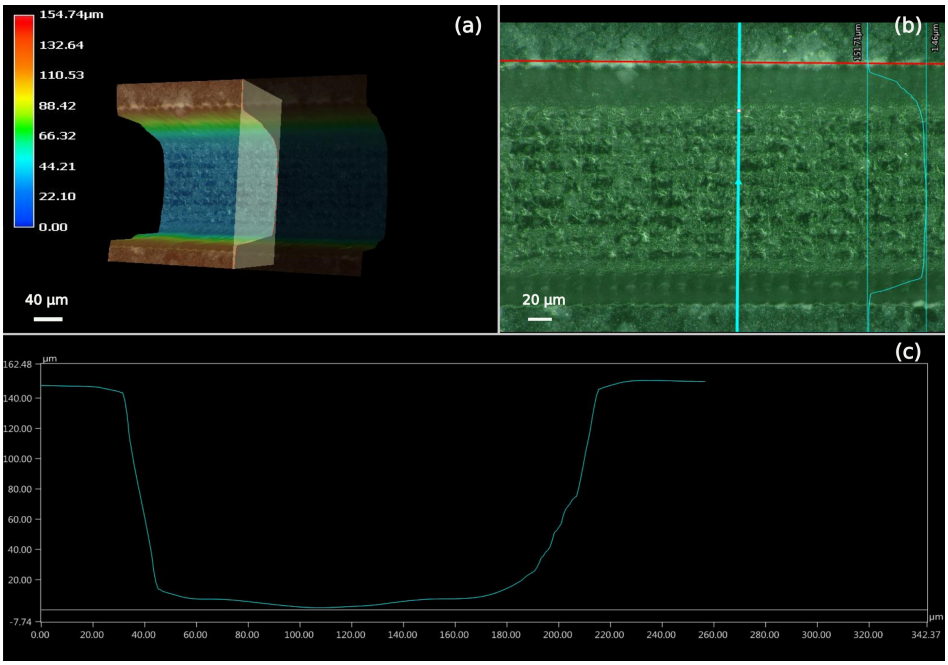

Figure 3-8: (a) 3D reconstruction of the femtosecond laser cut channel using found parameters. (b) Evaluation of the channel profile in the middle of the channel. (c) Zoomed in channel profile in the middle of the channel with a height of 123.16 μm

- Speed = 10 mm/s
- Jump Speed = 200 mm/s
- Laser firing rate = 50
- Burst time = 1000
- Repetitions = 40
- LaserOn Delay = 0
- LaserOff Delay = 0
- Laser Diode current = 6.44 A

The center of the holes is placed at each end of the channel as shown in Figure 3-9. This is done to prevent the debris from cutting the holes to block the fluid from entering and leaving the channel. By observing the channel near the holes, it was found that the channels need to be cut at the same side as where the holes are cut since the glass will melt and bulge out at the other end and block the channel on the other side but not on the side where the cutting takes place as shown in Figure 3-10a and Figure 3-10b.

Figure 3-9: Laser cut file of the channel together with the holes. The centers of the holes coincide with the channel ends. The channel length is equal to 40 mm, and the width is equal to 200 μm

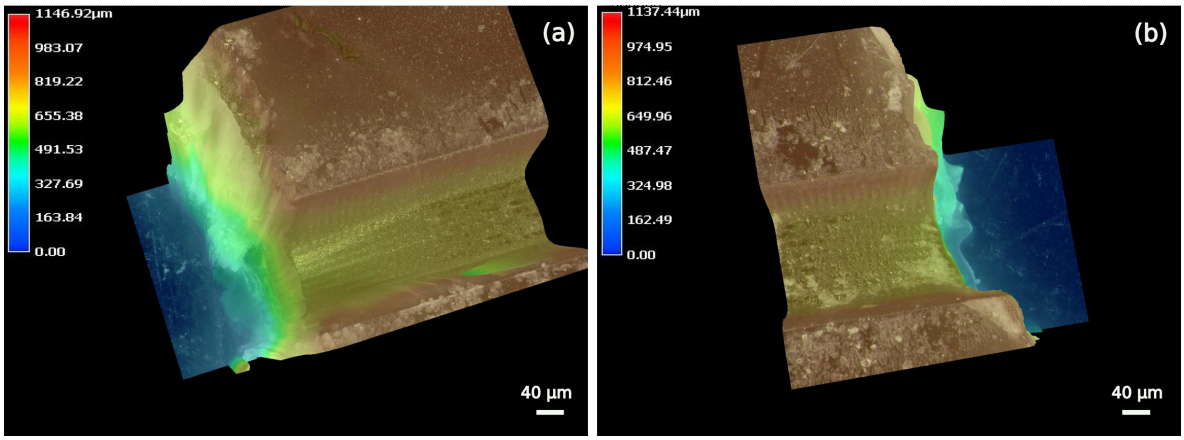

Figure 3-10: (a) 3D reconstruction of the left hole and adjacent channel with the keyence microscope. (b) 3D reconstruction of the right hole and adjacent channel.

3-7 Fabrication limitations

Our first choice was to use the femtosecond laser to fabricate the microchannels. However, due to challenges with accessibility and an unreliable model for the edge roughness, pure glass-to-glass bonding based on clamping [28], without the need for any polymer layer between the glass layers, was not possible. The roughness of the edges caused leakage and flow going out the channel.

Bonding the two glass layers with a polymer also presents its difficulties. It was challenging to prevent the polymer from flowing into the channel during the curing process. Once the polymer enters the channel, the channel will be blocked after curing, which renders it useless. Two glass plates were eventually connected with bio133 [54] without leakage, but there was too little time left to perform reliable trapping experiments due to high flow rates during actuation. So the following chapters will only focus on the chip with double-sided tape channels. Its fabrication procedure and operating instructions are described in detail in the HardwareX paper found in chapter 4.

Chapter 4

Low-cost acoustic force trap in a microfluidic channel

This chapter presents the step-by-step build instructions, operating instructions and main findings of the AFS chip with double sided tape channels.

Low-cost acoustic force trap in a microfluidic channel

Vi-hung Tsan, Daniel Fan, Sabina Caneva, Carlas S. Smith*, and Gerard J. Verbiest*

Faculty of Mechanical, Materials, and Maritime Engineering, Technische Universiteit Delft, Delft 2628CD, The Netherlands

g.j.verbiest@tudelft.nl, c.s.smith@tudelft.nl

Abstract A low-cost glass-based microfluidic flow cell with a piezo actuator is built using off-the-shelf parts to apply acoustophoretic force on polystyrene micro-beads. Beads with 1.5 μm diameter flowing in a 100 μm deep channel were trapped at 7.5 MHz using a 23.7 peak-to-peak voltage (V_{pp}) sinusoidal input. The trap located at 50 $\pm$0.1μm depth was measured to have a stiffness of approximately 0.6 pN/μm. This allows for the study of physical interactions between neighbouring beads and various applications such as cell trapping, manipulation, and basic physics and engineering education. We intend to use the device for force spectroscopy on micro-bead tethered DNA. This can be combined with super-resolution imaging techniques to study protein binding along the DNA strand.

Keywords
Acoustic trapping, acoustic force spectroscopy, acoustophoretic, microfluidics, low-cost

Specifications table

Hardware name	Microfluidic acoustic force trap
Subject area	• Engineering and material science • Biological sciences (e.g. microbiology and biochemistry) • Educational tools and open source alternatives to existing infrastructure • General
Hardware type	• Imaging tools • Measuring physical properties and in-lab sensors • Mechanical engineering and materials science
Closest commercial analog	Lumicks z-Movi [1] or uFluidix custom chip [2]
Open source license	Copyright 2022 under the GNU General Public License (GPL). This hardware is free; you can redistribute it and/or modify it under the terms of the GNU General Public License as published by the Free Software Foundation; either version 2 of the License, or any later version. This hardware is distributed in the hope that it will be useful, but WITHOUT ANY WARRANTY; without even the implied warranty of MERCHANTABILITY or FITNESS FOR A PARTICULAR PURPOSE. See the GNU General Public License for more details. You should have received a copy of the GNU General Public License along with this article; if not, write to the Free Software Foundation, Inc., 51 Franklin St, Fifth Floor, Boston, MA 02110-1301 USA
Cost of hardware	9 - 230 EUR
Source file repository	*If you've uploaded your source files to an approved repository (OSF, Mendeley Data or Zenodo) write the DOI URL here. For exemple: http://doi.org/10.17605/OSF.IO/WGK7Q*

1. Hardware in context

Microfluidic devices are a versatile technology widely used for research in biotechnology, medicine, chemistry, etc. [3]. The trapping and manipulation of micro-sized objects within the microfluidic channel are especially relevant for cell studies, molecular biology, biotechnology, and medicine [4]. Acoustic force or acoustophoretic tweezers use ultrasonic pressure fields to trap multiple micro-particles in parallel [5]. Due to this device's multiplexing capability, it can offer statistically significant data on the DNA replication process by stretching DNA strands to study replication dynamics. A quantitative model of the replication process is still missing [6]. By utilizing these tweezers, statistically significant data can be obtained about the replication process cost-effectively and time efficiently. This may lead to the development of medicine for incurable diseases for example. Furthermore, these devices can also be used for contact-less transportation of fragile silicon wafers [7]. This can lead to a considerable reduction in the price of microchips found in nearly all devices. The acoustic tweezer can also be used to sort microparticles based on size. This ability allows it to be used to filter out bacteria or dust particles from water [8].

Compared with other micro-manipulation methods [9][10][11], acoustic tweezing is relatively low-cost and less complex in terms of hardware, allows for a high number of particles to be trapped for high-throughput measurements, and affects the trapped object less (e.g., less local heating effects compared to optical trapping). Although acoustic traps have a comparatively lower spatial resolution, they can still provide performance similar to magnetic traps.

Multiple designs using acoustic traps have been realized, including surface acoustic waves, travelling waves, and acoustic streaming [5]. However, we focus on one of the simplest designs: a layered resonator, schematically shown in Figure 1, which uses a bulk acoustic standing wave to levitate micro-objects in the middle of a microfluidic channel [12][13]. We can study the interactions between neighbouring objects by trapping objects at the focal plane of the imaging device. Further, by tethering DNA strands to the coverslip and micro-beads at the other end and trapping those beads, we can perform acoustic force spectroscopy on stretched DNA strands [13].

Therefore, our objective is to replicate the device in [13] with a simple fabrication method accessible to most laboratories and with the following goals:

- Low-cost using off-the-shelf parts.
- Trap micro-beads between 1 and 10 μm.
- Trap multiple beads simultaneously.
- Able to trap at a force equivalent to $\sim$100 pN for a 10 μm DNA strand attached to a 4.5 μm polystyrene bead.

2. Hardware description

We present a simple, easy-to-build, and low-cost microfluidic chip with a piezo actuator based on [13]. As far as the authors are aware, the closest commercial equivalent is either an integrated system specifically for measuring cell avidity [1], or a custom-made system that becomes cost-effective only for bulk orders [2] (and hence not suitable for rapid prototyping). The chip we present is:

- Suitable for biological experiments such as bead trapping and stretching tethered biomolecules, e.g. DNA, as the glass material can be easily cleaned and functionalized.
- Suitable for educational experiments to explain acoustic forces as well as physics/biophysics experiments such as studying the interactions between particles close to each other.
- Compatible with super-resolution imaging due to the incorporation of standard thickness coverslips.
- Cheaper and simpler than commercial devices and allows high-throughput experiments as multiple beads can be trapped at the same time.

Further, acoustic force traps avoid common micro-object trapping problems such as local heating (optical trapping), charge screening in salty solutions (electrical trapping), customized beads (magnetic trapping), low throughput (mechanical trapping[14]), and limited control (hydrodynamic trapping).

For design considerations, we simulated the acoustic pressure field across the structure in Figure 1 using COMSOL Multiphysics 5.6 (see design files). We verified the results using calculations based on an equivalent circuit model [15]. For a 100 μm deep channel filled with deionized water (speed of sound in water is approximately 1480 m/s), the fundamental mode, where the trap is located halfway at 50 μm, occurred at approximately 7.4 MHz since $f_0 = v/2h$ where v is the speed of sound, h is the height of the channel, and f_0 is the frequency of the fundamental mode.

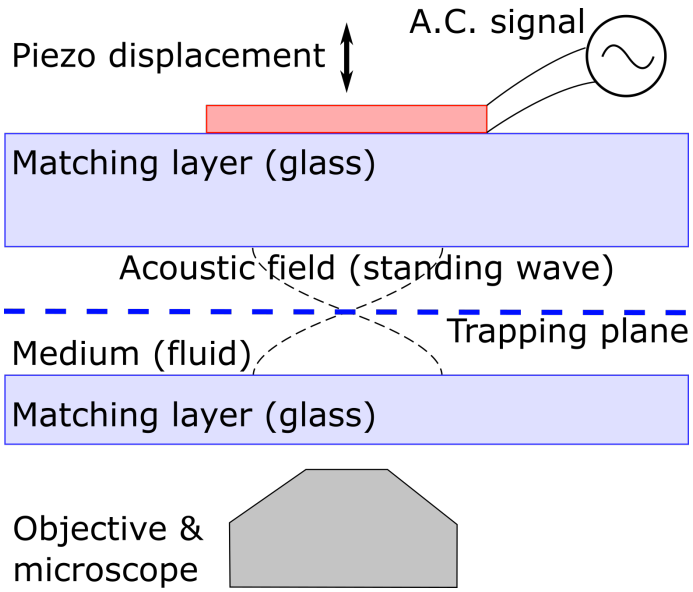

Figure 1: Concept of acoustic force or acoustophoretic trapping. Sound waves are generated by piezo displacement actuated via a signal generator. For the fundamental frequency, a standing wave will form in the layered structure, with a node appearing in the middle of the fluid channel. Beads and other micro-objects are trapped at this node due to the scattering of acoustic waves. The trapped objects are observed via a microscope.

The piezo disc was then selected to be able to reach the calculated frequency, and the material stack was chosen to ensure a minimal amount of acoustic damping. Typically, customized microfluidic devices are made from polymers such as polydimethylsiloxane (PDMS), which are easier to mold into channels. However, since we require high Q-factors to avoid damping of acoustic forces, we chose a glass substrate and glass matching layer.

Originally, we chose to fabricate a microchannel in the glass substrate via laser ablation using a fs-laser cutter, followed by bonding the glass coverslip via dehydration condensation [16]. However, while the laser-cut channel profile was acceptable (100 μm deep and 200 μm wide), the slag at the edges of the channel bulged out slightly by approximately 3-5 μm. This bump prevented strong glass-glass bonding as the two surfaces were not sufficiently flat. Therefore, we chose to fabricate the channel using two strips of double-sided tape. In this case, care must be taken to prevent air bubbles in the adhesion surfaces by pressing gently but firmly down using a plastic pipette. The edges can then be sealed using epoxy glue or nail polish.

3. Design files summary

Design filename	File type	Open source license	Location of the file
afchip.mph	COMSOL simulation	...	Online (see instructions)

A finite element model (COMSOL) used to simulate the acoustic pressure is provided for purposes of modification of design. It models the structure in Figure 2. Since the device is made from off-the-shelf parts, only a sketch Figure 2 is provided along with build instructions.

4. Bill of materials summary

Designator	Component	Number	Cost per unit currency	Total cost currency	Source of materials	Material type
1	Piezo disc PRYY+0398	1	€8	€8 (minimum order €80)	Physik Instrumente (PI) GmbH & Co. KG https://www.physikinstrumente.store/eu/pryy-0398/?c=65670	Ceramic
2	Epoxy glue	0.1 gram	€11.49 per 30 gram	€0.04 (minimum orde €11.49)	Gamma https://www.gamma.nl/assortiment/super-epoxy-30-gram/p/B432512	Polymer
3	Silver conductive paste	0.05 gram	€19.2 per 3 gram	€0.32 (minimum order €19.2)	Farnell https://nl.farnell.com/electrolube/scp03b/paint-conductive-scp-silver-3g/dp/725614?CMP=grhb-commerceconnect	Metal
4	Wires	30 cm	€0.21 per meter	€0.06 (minimum order €21)	RS https://nl.rs-online.com/web/p/hook-up-wire/1805914	Metal, polymer
5	Aluminium foil	1 cm^2	€0.08 per meter	€0.08 (minimum order €1.39)	Action https://www.action.com/nl-nl/p/dumil-aluminiumfolie-/	Metal

6	Glass microscope slide 631-1552 (76x26x1 mm)	1	€0.10	€0.10 (minimum order €5)	VWR https://nl.vwr.com/store/product/564378/object glaasjes#order	Inorganic
7	Scotch 3M double-sided tape 12 mm wide, 0.1 mm thick	20 cm	€2.95 per 6.3 meters	€0.10 (minimum order €2.95)	https://www.123inkt.nl/3M-Scotch-665-dubbelzijdig-tape-12-mm-x-33-m-6651233-i24276-t62000.html	Polymer
8	Glass coverslip #1.5 thickness 631-0853 (24x60 mm)	1	€0.09	€0.09 (minimum order €86.5)	VWR https://nl.vwr.com/store/catalog/product.jsp?catalog_number=631-0853	Inorganic

Table 1: Table containing all the materials needed to build the chip (€8.79 per chip).

The total cost of the chip (not including driving hardware and microscope) is approximately €9. For minimum order amounts, the total cost is approximately €230. This does not include equipment necessary for fabrication: soldering iron, solder, drill with a bit suitable for glass, ultrasonic bath, pipette tip, scalpel, toothpick, gloves, nail polish, and solvents for cleaning.

5. Build instructions

See Figure 3 for corresponding photos in the build instructions.

a) Drill two holes through a glass slide roughly centered and roughly 40 mm apart. A Dremel-type drilling tool with a 4 mm diameter drill bit suitable for glass can be used at low rpm and light pressure.

b) Clean glass slide (item 6) and coverslip (item 8) using acetone immersion combined with ultrasonic cleaning for 5 minutes, then isopropanol immersion with ultrasonic cleaning for 5 minutes, followed by a thorough rinse in deionized water and drying under an air-gun.

c) Place the glass slide on a clean, flat surface and tape it down along the two long edges with double-sided tape (item 7), leaving a 2 mm gap between the tapes and down the middle of the glass slide. Make sure the tape is flat.

d) Carefully place the coverslip on top of the two double-sided tapes.

e) Use a plastic pipette tip to gently press the coverslip down into the tape so that it is flat. Interface colour darkening as the coverslip is pressed indicates good contact of the coverslip with the tape. Therefore, press all along the edges of the microchannel.

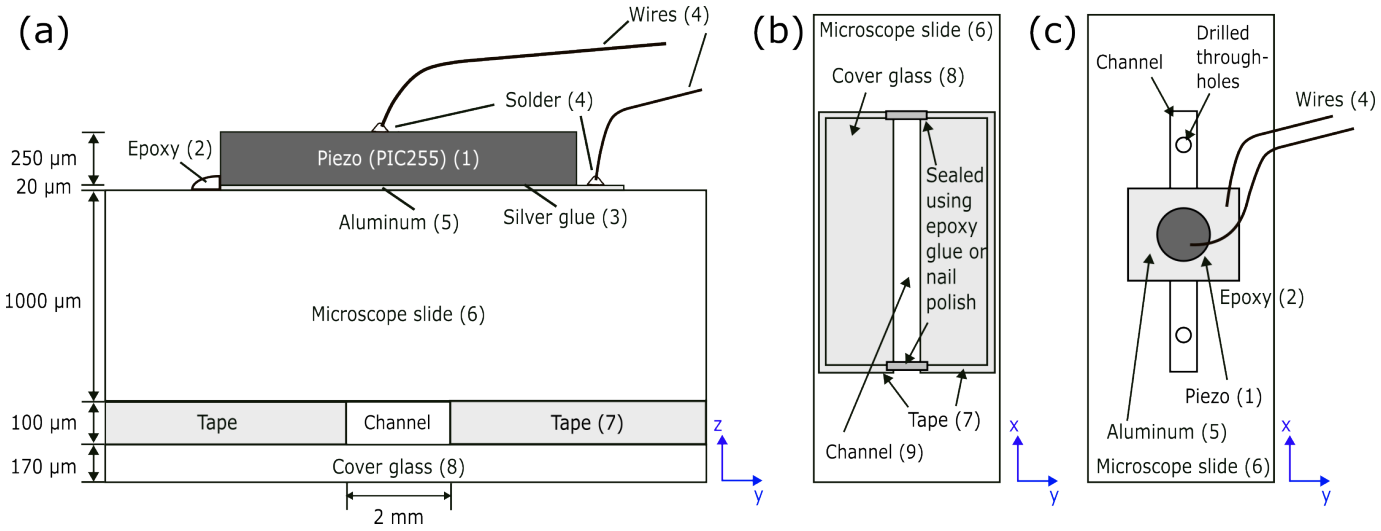

Figure 2: Schematic of the device with side view along the length of the microchannel (a), bottom (b) and top-down view (c). Numbers correspond to designated in "4. Bill of materials summary".

f) Use a scalpel to remove the excess double-sided tape.

g) If there are through-holes, ensure the double-sided tape does not cover them.

h) Once the coverslip is placed over the microchannel, the edges can be sealed using epoxy glue or nail polish.

i) Cut a thin strip of aluminium foil (item 5) of approximately 5 mm x 20 mm. Place on the glass slide over the microchannel. Use a toothpick to place a droplet of conductive silver paste (item 3) in the center of the aluminium foil over the microchannel. Place the piezo disc (item 1) on top of the silver paste droplet and press down.

j) Using another toothpick, cover the edges of the foil/piezo disc sitting on top of the glass slide with epoxy glue (item 2). Wait for it to cure (approximately 1 hour).

k) Once cured, solder one wire (item 4) onto the top of the piezo disc and one wire (item 4) onto the excess aluminium foil. The top and bottom of the piezo disc should now be electrically contacted by wires. Use tape to ensure the wires are mechanically stable.

- Safety: be careful when using the scalpel and soldering iron. Ensure ventilation when using epoxy glue and silver paste.

6. Operation instructions

- Fill the microchannel with ethanol via capillary forces using a pipette at one end and tissue at the other end, or if through-holes are present, simply pipette into the through-holes. This is to wet the surfaces of the microchannel.
- Flush the microchannel with deionized water using a pipette at one end and tissue at the other end or via the through-holes.
- Connect the wires to the amplifier (Analog Devices ADA4870) and connect the amplifier to the signal generator (RS pro RSDG 830) and power supply (Delta electronics E018-0.6D) as per Figure 4.
- Fill the channel with 1.5 μm diameter polystyrene microbeads (or other micro-objects) suspended in deionized water.

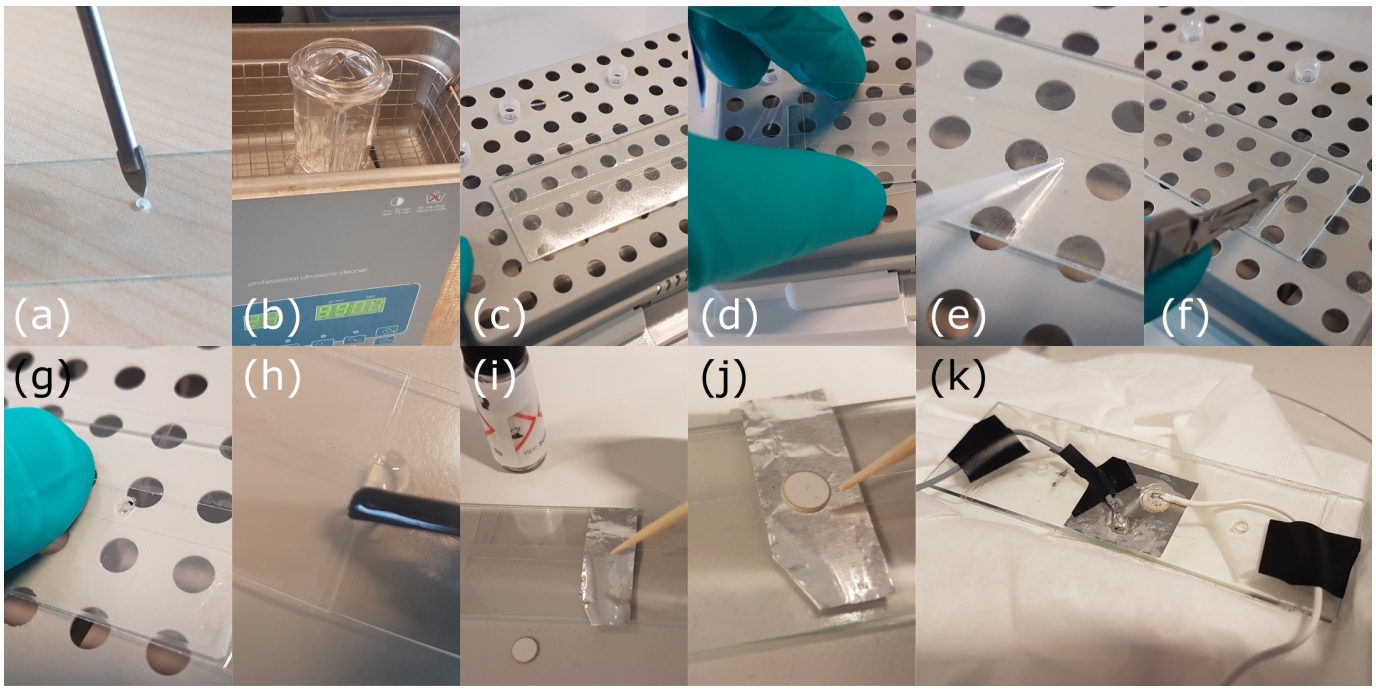

Figure 3: Fabrication procedure as outlined in "5. Build instructions"

- Place the chip on an inverted microscope. The device is now ready for imaging and trapping of micro-objects using acoustophoresis. For example, turn the signal generator on to generate a sinusoidal with a frequency of 7.5 MHz and adjust the amplitude by using this signal generator, whose amplitude will be amplified approximately 2.7 times by the amplifier to output the required V_{pp}. The beads should now be trapped at a particular focal plane. This can be observed through the microscope by adjusting the excitation intensity level and camera exposure time. In this paper the Nikon Eclipse TS2R inverted microscope with a water immersed objective and 60 times magnification is used for the derivation of the calibration curve and trapping experiments. The camera pixel size is 0.126 μm per pixel with an array size of 4908x3264 pixels. The image acquisition settings are: 50 frames per second, exposure time of 500 μs, a light source with a wavelength of 470 nm and the light intensity is set with 64 times analog gain and ten manual turns on the intensity knob.
- Safety: ensure electrical connections are well made and not touching each other.

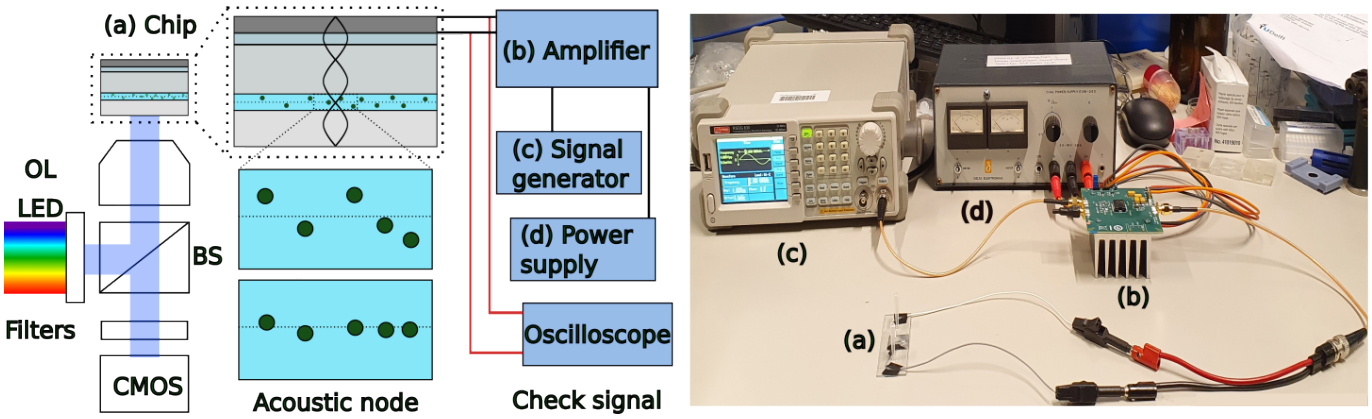

Figure 4: The left image is a schematic of the setup used for trapping the experiments. The movement of the beads is imaged through an objective lens (OL) with filtered light from a LED (light-emitting diode) source that passes through a beam splitter (BS), and the reflected light from the beads is processed with a digital camera (CMOS). The chip is connected to the amplifier's output ports, which are connected to the power supply and signal generator. The oscilloscope can be connected in parallel to the chip to check the input signal. The right image is a picture of the real setup, where (a) represents the chip,(b) amplifier (Analog Devices ADA4870), (c) signal generator (RS pro RSDG 830) and (d) power supply (Delta electronics E018-0.6D) in both images.

7. Validation and Characterization

The trap stiffness of the fundamental frequency can be derived from the FEM model by calculating the acoustic radiation force profile in the middle of the channel. This profile is derived by placing ten evenly spaced 1.5 micron polystyrene beads in a vertical line through the middle of the channel as shown in Figure 5a and Figure 5b. Ten beads are needed to sample the sinusoidal acoustic force profile with a sampling rate ten times its frequency [17] with negligible interaction between the beads .

With these ten data points, a sine wave can be fitted to the data to derive the acoustic radiation force shown in Figure 5c for 23.7 V_{pp}.

By taking the derivative of these sinusoidal curves at the middle of the channel ($z = 50$ μm) with respect to z, one can retrieve the trap stiffness for the fundamental frequency. By repeating this procedure for all relevant V_{pp} values, the trap stiffness curves shown in Figure 5d can be calculated.

The force on a DNA strand with a length of 10 μm can be derived from the trap stiffness by observing that the derivative at the center of the channel ($z = 50$ μm) in Figure 5c is roughly equal to the derivative at $z = 0$ μm and $z = 100$ μm and further, close to a node, the sinusoidal acoustic radiation force can be approximated to be linear. So the force on the DNA is therefore simply the length of the DNA strand multiplied by the trap stiffness for the fundamental frequency.

For example, the trap stiffness for 23.7 V_{pp} at 7.41 MHz is equal to 2.36 pN/μm for the simulation model without glue. This value times the length of the DNA becomes 23.6 pN. This value is a good approximation of the actual force experienced at 10 microns away from the bottom glass layer (at $z = 0$ μm) or top glass layer (at $z = 100$ μm) as shown in Figure 5c. This same assumption holds for the COMSOL model with glue, which is evident from Figure 5c and Figure 5d.

For validation, we first derived the calibration curve of the axial position versus σ_x in micrometers (from Equation 1) on a fixed bead sample (Fluoresbrite YG carboxylate 1.5 μm polystyrene beads beads immobilized in 0.1 w/v % agarose solution) by scanning the axial position of the stage (i.e. the focal plane) through a bead.This calibration curve is derived with the following camera settings: exposure time of 1 ms, 470 nm wavelength light source, 64 analog gain light intensity and turning 30 times the manual light intensity knob. We then placed the device in an inverted microscope (Nikon) and injected 1.5 μm polystyrene beads suspended in deionized water at a concentration of $1.8461 \cdot 10^7$ beads/mL. Low concentrations of beads are required to reduce the interaction between the beads that attract each other [18] and avoid overlapping beads. Videos of the suspended beads being trapped were recorded at a frame rate of 50 frames per second, exposure time of 500 μs,

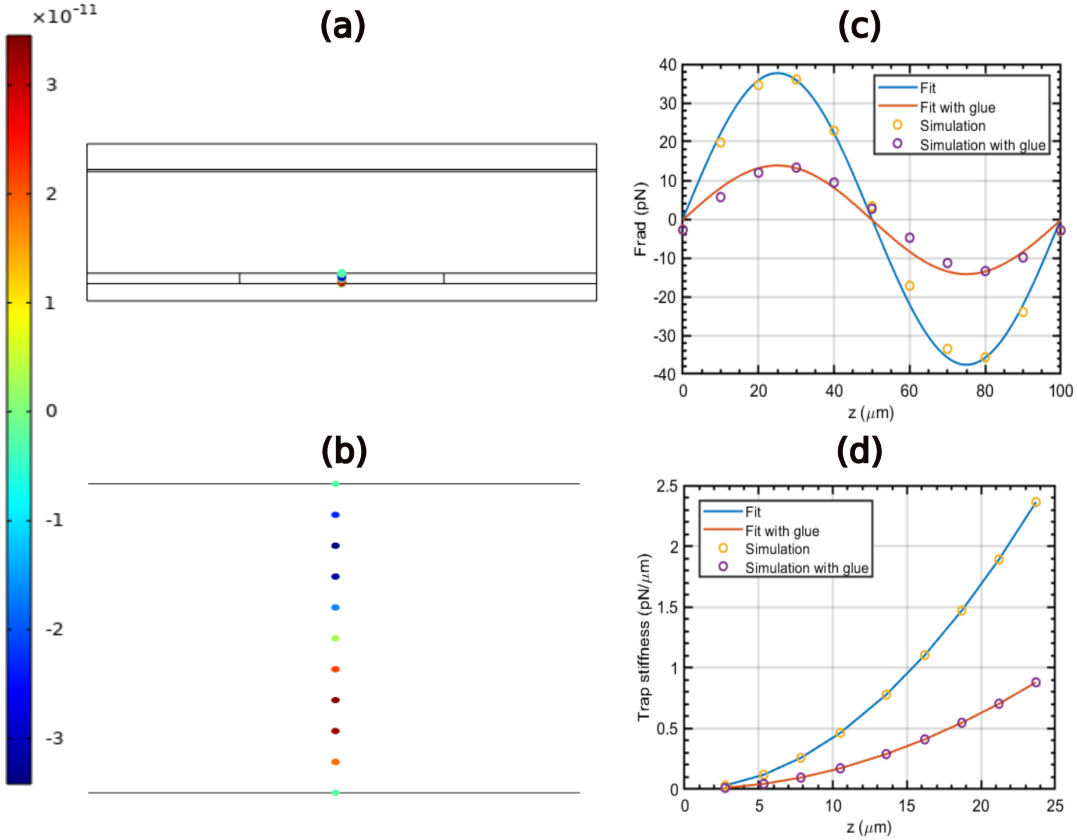

Figure 5: Procedure to derive simulated trap stiffness. (a) A schematic drawing of the device modelled in COMSOL Multiphysics 5.6 with 1.5-micron polystyrene beads placed in a vertical line through the center of the channel. (b) Zoomed in figure of the beads with the colours corresponding to the scale bar and representing the magnitude of the acoustic radiation force in Newtons on the given bead position at excitation frequency of 7.41 MHz and an amplitude of 23.7 V_{pp}. (c) Sinusoidal fit to the simulated acoustic radiation force data from figure 5c. (d) A plot of trap stiffness against the applied V_{pp} at excitation frequency of 7.41 MHz.

a light source with a wavelength of 470 nm and 64 times analog gain and ten manual turns on the intensity knob to regulate the light source intensity, tuned to ensure that the bead intensities were not saturated. Different lightning conditions between the calibration and experiment is used because of the low signal to noise ratio of the calibration sample. This can be caused by the fact that the beads in the calibration are used multiple times, and therefore bleaching occurs, and they are stored outside the fridge for some time and therefore lose some of their fluorescence. In order to deal with different lightning conditions the mean is subtracted and all the intensity profile of each bead is normalized with its maximum value [19] [20].

In Figure 6a-d, the subsequent frame-by-frame image analysis and axial localization algorithm are shown. The peak detecting algorithm developed by Blair et al. [21] is used to detect the bead locations in 2D (Figure 6b). When the 2D location of the bead is known, the image is cropped further to contain a single bead (Figure 6c). The intensity profile of each bead image is normalized with its maximum value, and then a 2D Gaussian fit is applied (Figure 6d). The 2D Gaussian fit uses nonlinear quadratic optimization to fit the 2D Gaussian function [22] to the intensity profile of the bead. This function reads as:

$$f(x,y) = Ae^{-\left(\frac{(x-x_0)^2}{2\sigma_x^2}+\frac{(y-y_0)^2}{2\sigma_y^2}\right)} + B \tag{1}$$

Where A represents the normalized amplitude of the beads' intensity profile with a value between 0 and 1, (x_0,y_0) represents the center coordinate of the bead in micrometers, σ_x and σ_y represents the standard deviation in x and y in micrometers, respectively and B represents the background term.

Only the value of σ_x will be used for the derivation of the calibration curve and characterization of the trap stiffness. The squared norm of the residual for the fit and the absolute difference between σ_x and σ_y needs to be smaller than a given threshold to filter out overlapping beads or beads that are excessively distorted due to the planar motion, after which only σ_x is used. During optimization it was found that by fixing the background value B to zero, low variance in the calibration curve is realized.

By applying this procedure to the fixed bead sample for different focal planes, the calibration curve in Figure 6e can be obtained. The calibration curve is fitted to the medians of σ_x between a z-range of -5 to 5 micron as shown in Figure 6e to obtain a R^2-value above 0.8 ($R^2 = 0.86$) and the resulting equation is:

$$\sigma_x = 2.69 \cdot 10^{-9} z^4 + 0.028 z^2 + 0.39 \tag{2}$$

By following the same image processing procedure Figure 6a-d for beads suspended in deionized water and trapped using the acoustic force device, we can obtain values of σ_x for the trapped beads within a user-defined region of interest. With these σ_x values (in microns), we can use the calibration curve described in Equation 2 to obtain the δz distance away from the focal plane. The real and positive δz value is used since the calibration curve is symmetric, and only the distance between the bead and the focal plane can be calculated. However, since we are only interested in the trapping stiffness, this does not matter, and the absolute value of δz is sufficient. The obtained δz values are then mirrored about the vertical axis where δz equals zero to obtain a Gaussian distribution. Hereafter, the variance in δz is derived with Gaussian fitting.

The equipartition theory describes the stiffness of an acoustic trap. This theory is dependent on the frame rate of the image acquisition device, but it will saturate to a fixed value, as is shown by Pesce et al. [23]. and Gerspach et al. [14]. Gerspach et al. described that the saturation value could be used to determine the trapping stiffness, which will make the equipartition theory independent of the frame rate of the capturing device. For one coordinate, the saturated equipartition theory value is given by [23]:

$$var(z) = \frac{2k_B T}{k_z} \tag{3}$$

Where $var(z)$ represents the variance in the axial position z in micrometers, k_B represents the Boltzmann constant, T is the absolute temperature in Kelvin, and k_z is the stiffness of the trap in the axial direction z in N/m.

Assuming the absolute temperature to be 293.15 K, one can derive the trapping stiffness for 18.7 V_{pp} shown in Figure 6h to be 0.54 pN/μm. Furthermore, a stiffness curve can be plotted by performing these trapping experiments with different V_{pp} values as shown in Figure 6f.

We verified the result using FEM by simulating the same device geometry and input voltages. The trap stiffness of the FEM simulation is then derived using the acoustic force profile in the fluid layer. An example of an acoustic force profile is shown in Figure 6g for 23.7 V_{pp}. The trap stiffness is found by taking the derivative of this profile at z=50 μm with respect to z. A simulated stiffness curve is obtained by performing this calculation for different V_{pp} values (Figure 6f), which can be compared with experimentally determined trap stiffness values.

From the results shown in Figure 6f, we have been able to reach a trap stiffness of approximately 0.6 pN/μm at 18.7 V_{pp} for 1.5 μm polystyrene beads. Higher input voltages can cause cavitation and heating inside the channel, leading to air bubbles forming and fast drying of the channel fluid. The trap was located at 50 μm depth in the channel. Varying the frequency slightly away from 7.5 MHz caused the trap to disappear.

A video of the trap operation is included in the supplementary materials. Still, frames are shown in Figure 7. Initially, the beads suspended in a fluid are randomly distributed, as can be seen from the varying point-spread-function sizes. Once the trap is turned on (Figure 7b), the beads move and stay at the focal plane, after some time, neighbouring beads started interacting with each other (Figure 7c), this forms an experimental basis for the study of particle interaction, for example.

If we assume the sinusoidal acoustic pressure field is roughly linear close to a node, then for a 10 μm DNA strand tethered to a 1.5 μm bead, the maximum force experienced is 6 pN. Since the acoustic radiation force on an object scales with its volume [13] and the gravitational and buoyancy forces are cancelled, we expect for a 4.5 μm bead (which is three times as large as the 1.5 μm bead) a $3^3 = 27$ times increase in maximum force, i.e., 162 pN.

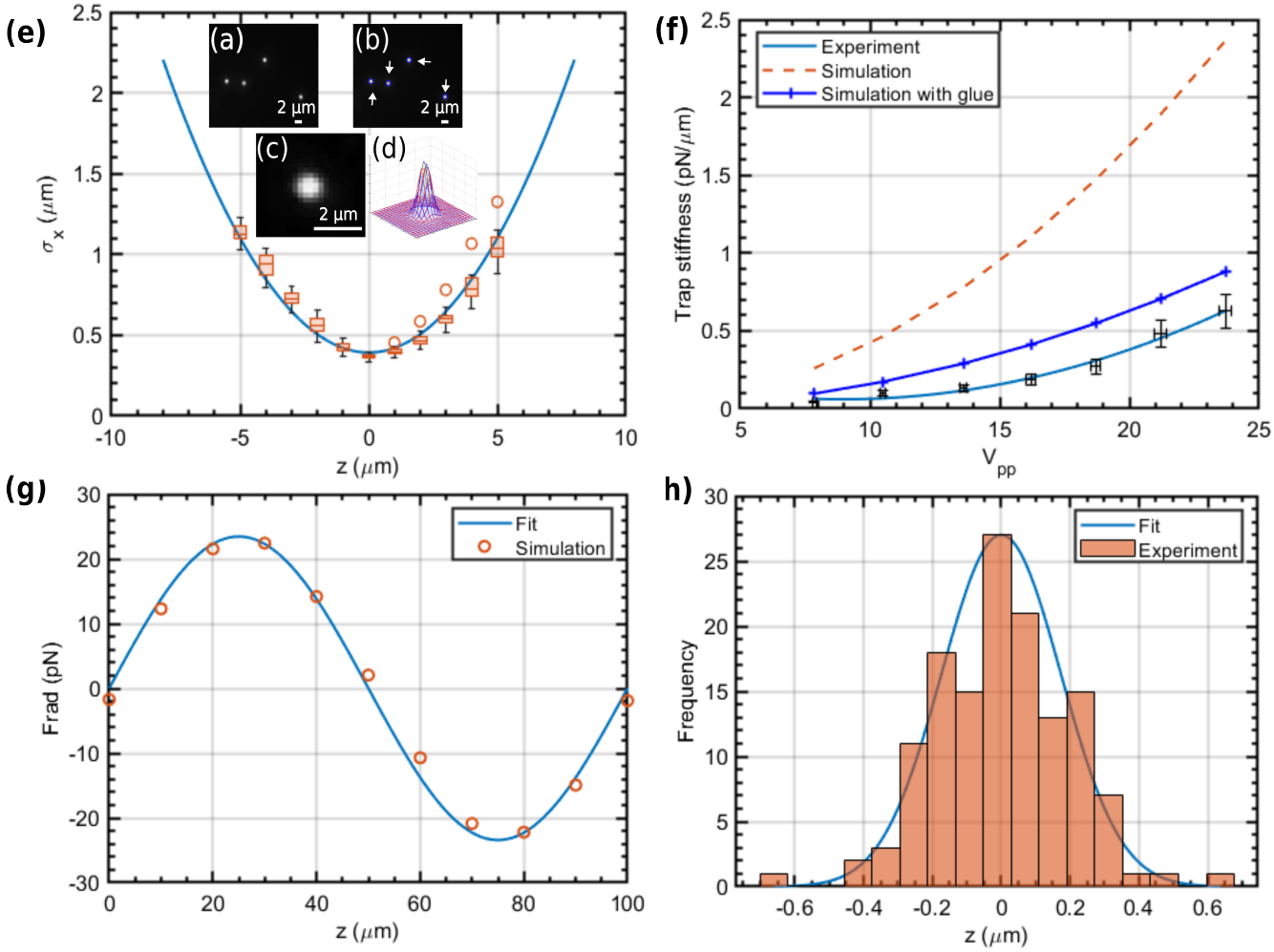

Figure 6: Image processing procedure (a)-(d) represents a step-by-step procedure to obtain the calibration curve as well as the trap stiffness from experiments. (a) The original frame containing 1.5 micron beads in agarose for calibration, (b) detected beads in a 2D plane marked by blue circles and white arrows, (c) cropped image around a single bead and (d) the 2D Gaussian fit with Equation 1 to obtain the σ_x value for every bead intensity profile. (e) The corresponding calibration curve for the calibration sample is shown with error bars indicating uncertainty and circles representing outliers and the z-coordinate describes the distance away from the focal plane. (f) A plot of the simulated and experimental trap stiffness for a range of V_{pp} values and error bars representing uncertainty in experimental results. (g) Simulated acoustic radiation force on a 1.5 micron bead at 7.41 MHz (simulated half-wave mode) and 18.7 V_{pp} with z-coordinate representing the distance away from the top glass/microscope slide. (h) Example of histogram obtained with the image processing procedure and the calibration curve for trapping experiment at 7.5 MHz and 18.7 V_{pp} with z-coordinate representing the distance away from the trap/focal plane and negative values represents position below focal plane.

Although the target stiffness was reached, there is still some discrepancy between simulated trap stiffness and experimentally obtained values Figure 6f. This can be explained by the fact that the glueing layers between piezo, aluminium foil, glass, and double-sided tape were not included in the finite element model. Air bubbles which become trapped at the tape-glass interfaces can form during fabrication, lowering the overall stiffness of the device. Further, operating the piezo at high input voltages can cause heating of the device, which in turn affects the mechanical properties of the glueing layers.

Some future suggestions to improve trap stiffness include using laser-cut channels with the channel edges ground down to achieve a flat glass surface suitable for glass-to-glass bonding. However, this might increase

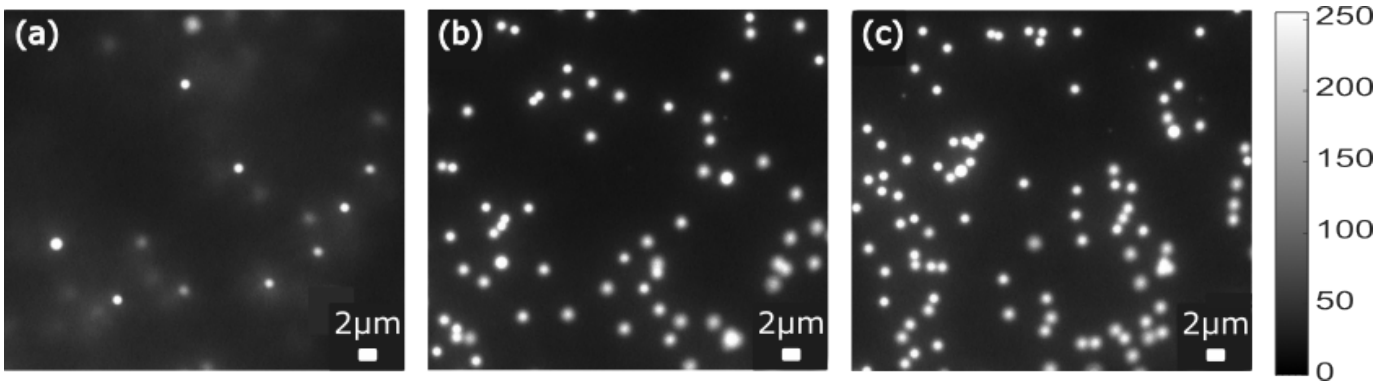

Figure 7: (a) Beads image without actuation of piezo. (b) Bead trapping right after actuation of piezo. (c) Bead trapping after 9.6 seconds of actuation.

fabrication costs and require specialized tools. Purchasing piezo discs with wrap-around electrodes would help avoid too much glue on the top of the glass slide, but again with a matching cost increase.

In summary, we have fabricated a low-cost acoustic force microfluidic device suitable for trapping polystyrene beads to study biomolecules, physical interactions between neighbouring beads, and general education. Total costs per unit can be as low as ∼10 EUR while still producing a 0.6 pN/μm trap on multiple 1.5 μm beads.

CRediT author statement

Vi-hung Tsan: Methodology, Investigation, Software, Validation, Writing - Original Draft **Daniel Fan**: Methodology, Supervision, Writing - Original Draft **Sabina Caneva**: Methodology, Writing - Review & Editing **Carlas S. Smith**: Conceptualization, Writing - Review & Editing, Funding acquisition **Gerard Verbiest**: Conceptualization, Supervision, Funding acquisition, Writing - Review & Editing

Acknowledgements

We would like to thank Murali Ghatkesar for discussions on acoustic impedance, Gurhan Ozkayar on microfluidic operation, and Dong Hoon Shin, Gideon Emmanuel and Andres Hunt for help with glass cutting and drilling.

This work was partially supported by the TU Delft cohesion grant (...)

This research did not receive any specific grant from funding agencies in the public, commercial, or not-for-profit sectors.

References

[1] *Working principle of Acoustic Force Spectroscopy*, LUMICKS, https://lumicks.com/knowledge/acoustic-force-spectroscopy-and-z-movi-technology/ (visited on 08/25/2022).

[2] *Microfluidic Acoustophoresis*, uFluidix, https://www.ufluidix.com/microfluidics-research-reviews/microfluidic-acoustophoresis/ (visited on 08/25/2022).

[3] A.-G. Niculescu, C. Chircov, A. C. Bîrcă, and A. M. Grumezescu, "Fabrication and Applications of Microfluidic Devices: A Review", International Journal of Molecular Sciences **22**, 2011 (2021).

[4] V. Ortseifen, M. Viefhues, L. Wobbe, and A. Grünberger, "Microfluidics for Biotechnology: Bridging Gaps to Foster Microfluidic Applications", Frontiers in Bioengineering and Biotechnology **8**, 589074 (2020).

[5] A. Ozcelik, J. Rufo, F. Guo, Y. Gu, P. Li, J. Lata, and T. J. Huang, "Acoustic tweezers for the life sciences", Nature Methods **15**, 1021–1028 (2018).

[6] R. Bocanegra, G. I. Plaza, C. R. Pulido, and B. Ibarra, "Dna replication machinery: insights from in vitro single-molecule approaches", Computational and Structural Biotechnology Journal **19**, 2057–2069 (2021).

[7]G. Reinhart, J. Hoeppner, and J. Zimmermann, "Non-contact wafer handling using high-intensity ultrasonics", in 2001 ieee/semi advanced semiconductor manufacturing conference (ieee cat. no. 01ch37160) (IEEE, 2001), pp. 139–140.

[8]M. Wu, A. Ozcelik, J. Rufo, Z. Wang, R. Fang, and T. Jun Huang, "Acoustofluidic separation of cells and particles", Microsystems & nanoengineering **5**, 1–18 (2019).

[9]A. Ashkin, J. M. Dziedzic, J. E. Bjorkholm, and S. Chu, "Observation of a single-beam gradient force optical trap for dielectric particles", Optics Letters **11**, 288 (1986).

[10]A. R. Bausch, W. Möller, and E. Sackmann, "Measurement of Local Viscoelasticity and Forces in Living Cells by Magnetic Tweezers", Biophysical Journal **76**, 573–579 (1999).

[11]A. Karimi, S. Yazdi, and A. M. Ardekani, "Hydrodynamic mechanisms of cell and particle trapping in microfluidics", Biomicrofluidics **7**, 021501 (2013).

[12]A. Lenshof, M. Evander, T. Laurell, and J. Nilsson, "Acoustofluidics 5: Building microfluidic acoustic resonators", Lab on a Chip **12**, 684 (2012).

[13]G. Sitters, D. Kamsma, G. Thalhammer, M. Ritsch-Marte, E. J. G. Peterman, and G. J. L. Wuite, "Acoustic force spectroscopy", Nature Methods **12**, 47–50 (2015).

[14]M. A. Gerspach, N. Mojarad, D. Sharma, T. Pfohl, and Y. Ekinci, "Soft electrostatic trapping in nanofluidics", Microsystems & nanoengineering **3**, 1–10 (2017).

[15]R. Krimholtz, D. Leedom, and G. Matthaei, "New equivalent circuits for elementary piezoelectric transducers", Electronics Letters **6**, 398 (1970).

[16]S.-i. Funano, N. Ota, and Y. Tanaka, "A simple and reversible glass–glass bonding method to construct a microfluidic device and its application for cell recovery", Lab on a Chip **21**, 2244–2254 (2021).

[17]R. S. Figliola and D. E. Beasley, *Theory and design for mechanical measurements* (John Wiley & Sons, 2020).

[18]T. Baasch, I. Leibacher, and J. Dual, "Multibody dynamics in acoustophoresis", The Journal of the Acoustical Society of America **141**, 1664–1674 (2017).

[19]L. A. Carlucci and W. E. Thomas, "Modification to axial tracking for mobile magnetic microspheres", Biophysical Reports **1**, 100031 (2021).

[20]J. P. Cnossen, D. Dulin, and N. Dekker, "An optimized software framework for real-time, high-throughput tracking of spherical beads", Review of Scientific Instruments **85**, 103712 (2014).

[21]D. Blair and E. Dufresne, *Particle location and tracking tutorial*, https://site.physics.georgetown.edu/matlab/, Accessed: 2022-07-06.

[22]G. Nootz, *Fit 2d gaussian function to data*, https://nl.mathworks.com/matlabcentral/fileexchange/37087-fit-2d-gaussian-function-to-data, Accessed: 2022-07-06.

[23]G. Pesce, G. Volpe, O. M. Maragó, P. H. Jones, S. Gigan, A. Sasso, and G. Volpe, "Step-by-step guide to the realization of advanced optical tweezers", JOSA B **32**, B84–B98 (2015).

Chapter 5

Chip Characterization

This chapter aims to describe the chip characterisation part. The main objective is to describe how captured videos and images of beads are analysed and converted to the trapping stiffness of the acoustic tweezer. First, the derivation of the simulated trap stiffness will be discussed. Hereafter, the setup used for the trapping experiment will be presented along with the image processing method. Then the derivation of the calibration curve, sample preparation, image acquisition, derivation of the histogram of axial position, equipartition theory and error propagation will be discussed. Finally, the results will be presented and as well discussed.

5-1 Simulation trap stiffness

The trap stiffness from the simulation is derived by placing ten beads in a vertical line in the middle of the channel, as shown in Figure 5-1a and Figure 5-1b. Ten beads are needed to sample the sinusoidal acoustic force profile with a sampling rate ten times its frequency with negligible interaction between the beads.

With these ten data points, a sine wave can be fitted to the data to derive the acoustic radiation force shown in Figure 5-1c for 23.7 V_{pp}.

By taking the derivative of this sinusoidal at the middle of the channel ($z = 50$ μm), one can retrieve the trap stiffness for the fundamental mode. And by repeating the procedure for all relevant V_{pp} values, the trap stiffness curve shown in Figure 5-1d can be derived.

The force on a DNA strand with a length of 10 μm can be derived from the trap stiffness by observing that the derivative at the center of the channel ($z = 50$ μm) in Figure 5-1c is roughly equal to the derivative at $z = 0$ μm and $z = 100$ μm and for small length scales the sinusoidal acoustic radiation force can be approximated to be linear. So the force on the DNA is therefore simply the length of the DNA strand multiplied by the trap stiffness for the fundamental mode.

For example, the trap stiffness for 23.7 V_{pp} at 7.41 MHz is equal to 2.36 pN/μm. This value times the length of the DNA becomes 23.6 pN. This value is a good approximation of the

simulated force experienced at 10 microns away from the bottom glass layer (at $z = 0$ μm) or top glass layer (at $z = 100$ μm) as shown in Figure 5-1c.

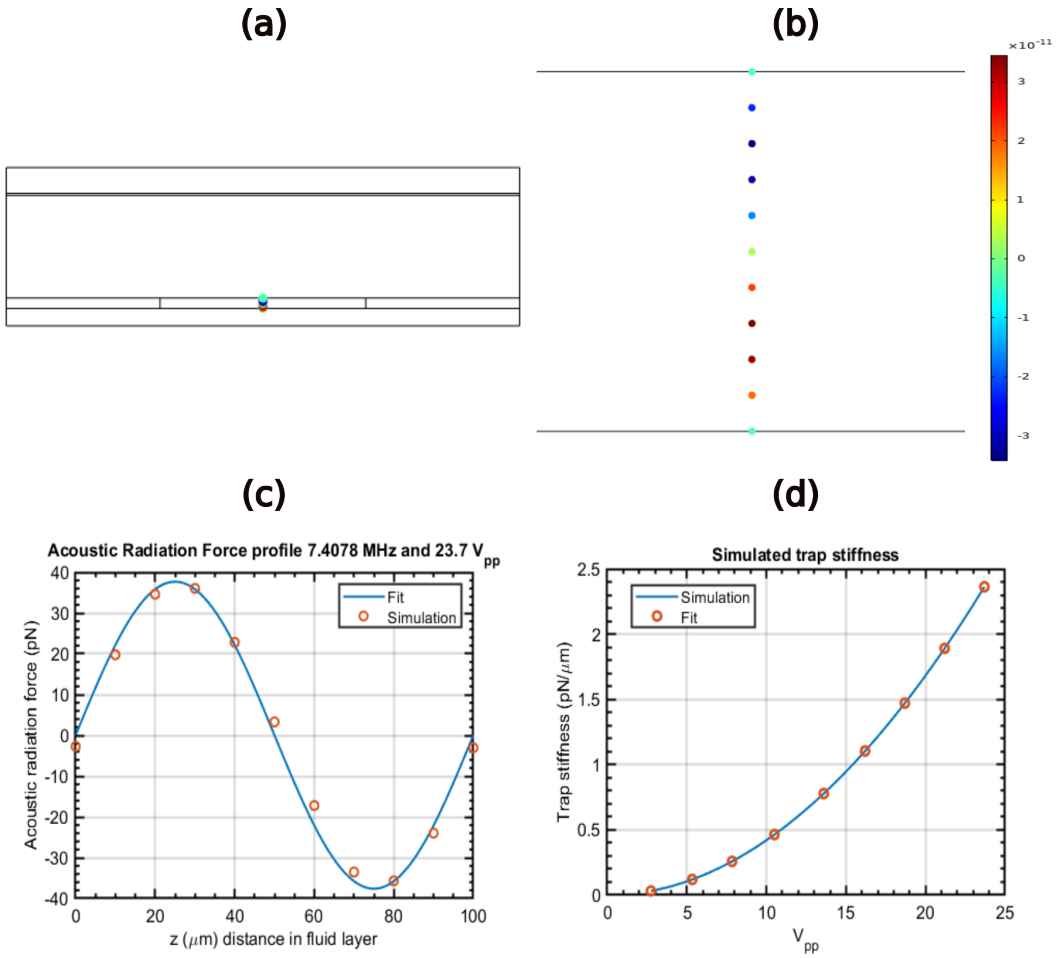

Figure 5-1: Procedure (a)-(d) represents the process of obtaining the trap stiffness from simulation. (a) Simulation of the acoustic radiation force on 1.5-micron polystyrene beads for the double-sided tape chip without glue layer at 7.41 MHz and 23.7 V_{pp}. (b) Zoomed in image of the acoustic radiation force on ten beads in a vertical line through the middle of the channel. (c) Fit a sinusoidal signal to the ten data points and derive the derivative of this function with respect to z at $z = 50$ μm. (d) Repeat this procedure for all relevant V_{pp} values to obtain this trap stiffness curve as function of V_{pp} at 7.41 MHz excitation.

5-2 Setup

The setup shown in Figure 5-2 is used to perform the trapping experiments. The function generator used in the experiments is the RS pro RSDG 830. This function generator can generate sine waves up to 30 MHz with a maximum peak-to-peak voltage of 20.

The amplifier used is the ADA4870, together with a heat sink underneath. This amplifier can, at most, generate an output of 40 peak-to-peak voltage with a frequency of 52 MHz, and it amplifies the input signal approximately 2.7 times. The amplifier is powered by the dual power supply Delta Elektronika E018-0.6D. This power supply can output +18 V, and -18 V, which results in a voltage drop of 36 V on the amplifier and the maximum current is limited to 0.6 A.

The chip is connected to the output gate of the amplifier and placed in the standard sample holder of the microscope.

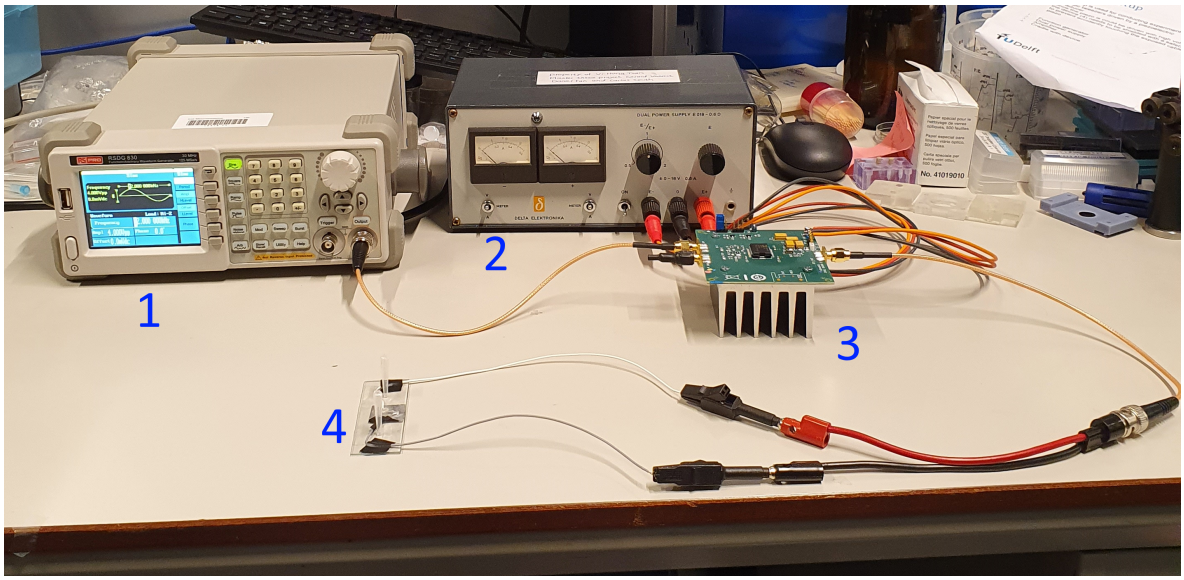

Figure 5-2: Setup used to perform bead trapping experiments, where 1 represents the sinusoidal function generator, 2 the dual power supply, 3 the amplifier and 4 the acoustofluidic chip.

5-2-1 Inverted microscope

The inverted microscope Nikon Eclipse TS2R with a water immersed objective, magnification of 60 times, camera pixel size is 0.126 μm per pixel and an array size of 4908x3264 pixels is used to capture images and videos for calibration and to trap experiments with the beads. The water immersion objective is used together with a 470 nm light source in echo-planar imaging (epi) mode and the maximum image acquisition rate of 50 frames per second (FPS). The focal plane can be adjusted with manual focusing knobs with the finest increments of 1 μm.

5-3 Image analysis

5-3-1 Image processing

In Figure 5-3, the image processing procedure of the 3D localisation algorithm is shown, which is based on the work of Gerspach et al. [30]. The in-plane localisation of the beads is conducted on a user-defined rectangular box (blue rectangle). This region of interest (ROI) is used on all the captured video frames for detecting beads. In addition, the peak detecting algorithm developed by Blair et al. [7] detects the beads' location in 2D.

When the 2D location of the bead is known, the image is cropped further to contain a single bead. Then, the intensity profile of each bead image is normalised with its maximum value, and a 2D Gaussian fit is applied to all the images. The 2D Gaussian fit uses nonlinear quadratic optimisation to fit the 2D Gaussian function [63] to the intensity profile of the bead. This function reads as:

$$f(x,y) = Ae^{-\left(\frac{(x-x_0)^2}{2\sigma_x^2}+\frac{(y-y_0)^2}{2\sigma_y^2}\right)} + B \tag{5-1}$$

Where A represents the normalized amplitude of the beads' intensity profile with a value between 0 and 1, (x_0,y_0) represents the center coordinate of the bead in micrometers, σ_x and σ_y represents the standard deviation in x and y in micrometers, respectively and B represents the background term.

Only the value of σ_x will be used for the derivation of the calibration curve and characterization of the trap stiffness. The squared norm of the residual for the fit and the absolute difference between σ_x and σ_y needs to be smaller than a given threshold to filter out overlapping beads or beads that are excessively distorted due to planar motion, after which only σ_x is used. During optimization it was found that by fixing the background value B to zero, low variance in the calibration curve is realized.

An off-focus calibration curve is needed to detect the axial position of the bead (z-coordinate). The derivation of the calibration curve is described in detail in section 5-4. This calibration curve describes the relationship between σ_x and the distance z away from the focal plane, so with this curve, one can derive the z position of the bead away from the focal plane whenever the σ_x is known.

5-4 Calibration

The calibration sample consists of immobilised beads in agarose solution. The agarose solution is used to approximate the optical properties of deionized water (DI) water, which is used for the trapping experiments. The z-stack of bead images with known displacements from the focal plane is obtained by varying the position of the focal plane with the focusing knob. These images are obtained with an exposure time of 1 ms, 470 nm wavelength light source, 64 analog gain light intensity and turning 30 times the manual light intensity knob.

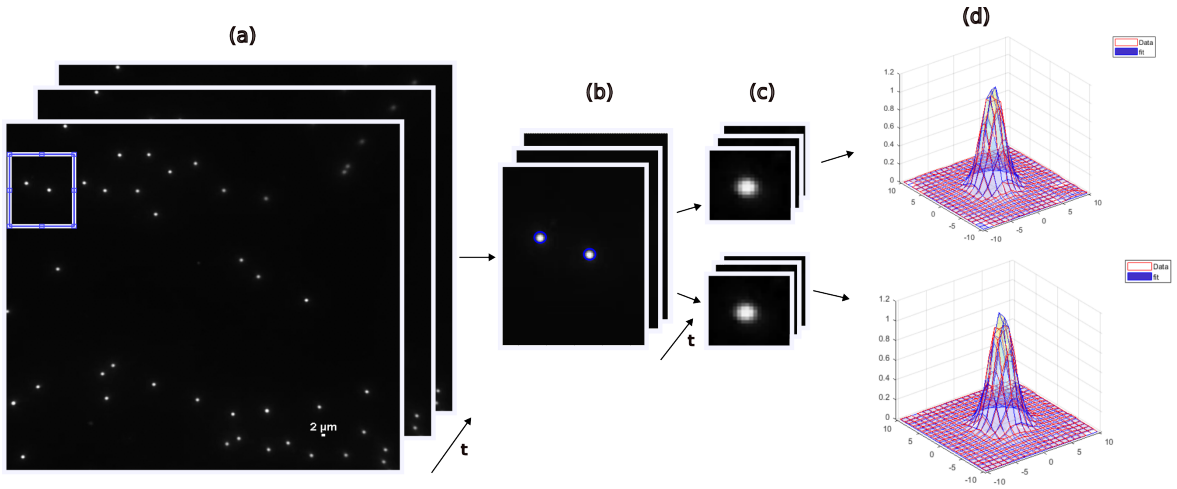

Figure 5-3: Flowchart of the localisation algorithm. (a) The region of interest (ROI) was selected by the user and applied to all the video frames captured with the inverted microscope. (b) Images cropped with the ROI used for tracking and further analysis. (c) Crop images further to contain a single bead. (d) 2D Gaussian fitting was applied on the cropped images containing single beads.

By applying the flowchart shown in Figure 5-3 to an image stack of known displacement away from the focal plane and a ROI that is equal to the original size of the image, one can obtain the calibration curve shown in Figure 5-4. This calibration curve contains box plots for each measured distance away from the focal plane. The circles represent outliers and indicate that moving the focal plane above the beads leads to more noise.

The calibration curve is fitted to the medians of σ_x between a z-range of -5 to 5 micron as shown in Figure 5-4e to obtain a R^2-value above 0.8 ($R^2 = 0.86$) and a fourth-order polynomial is used to reduce the noise [35] the resulting equation is reads as:

$$\sigma_x = 2.69 \cdot 10^{-9} z^4 + 0.028 z^2 + 0.39 \tag{5-2}$$

Where σ_x represents the standard deviation of the beads' intensity profile in the x-direction (in μm) and z distance of the bead away from the trap plane (in μm).

5-5 Measurements

5-5-1 Sample preparation

The bead trapping experiments are performed with Fluoresbrite YG carboxylate 1.5-micron beads [40]. The original concentration is diluted 1000 times with deionized water (DI), which results in $1.349 \cdot 10^7$ beads/mL. Low concentrations of beads are required to reduce the interaction between the beads that attract each other [5] and reduce the intensity of the beads.

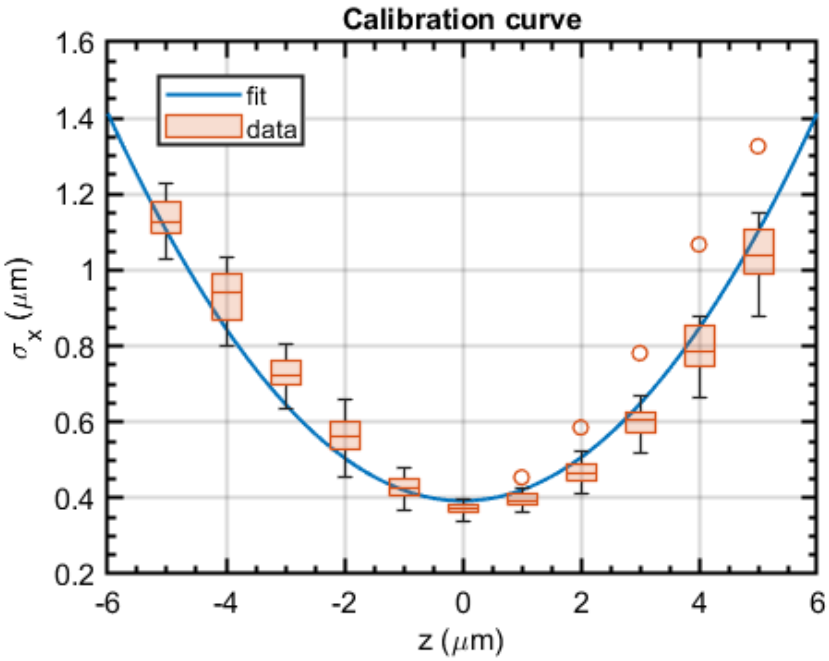

Figure 5-4: Calibration curve showing the relationship between σ_x and the distance z away from the focal plane. The boxplots show the uncertainty of each measured value due to the variation in bead size and finite accuracy of adjusting the focal plane, and the circles indicate outliers.

5-5-2 Image stack acquisition

The image stack for a given peak-to-peak voltage is obtained by recording a video when the piezo is actuated. This video is recorded with the maximum frame rate of 50 FPS, 500 μs exposure time, 64 times analog gain of light intensity, 470 nm wavelength of the light source and pushing 10 times on the manual light intensity knob. These settings are different from those used in the calibration because applying the same settings as in the calibration, will result in over-saturated intensity profiles. This can be caused by the fact that the beads in the calibration are used multiple times, and therefore bleaching occurs, and they are stored outside the fridge for some time and therefore lose some of their fluorescence. Also, it is difficult to obtain exactly the same concentration of beads. In order to resolve this issue, the mean is subtracted for each frame and all the intensity profiles of the beads are normalised by their maximum value. Since it can be assumed that the distribution of beads' intensity does not change with magnitude [14] [17].

5-5-3 Histogram of axial position

By following the flowchart shown in Figure 5-3, one can obtain the values of σ_x for the relevant trapped beads. With these σ_x values, one can use the calibration curve described in Equation 5-2 to obtain the z distance away from the focal plane. The real and positive z value is used in this case. Since the calibration curve is symmetric, only the distance between the bead and the focal plane can be calculated. However, since we are interested in the trapping stiffness, this value is sufficient. The obtained z values are then mirrored about the vertical

axis where z equals zero to obtain a Gaussian distribution. Hereafter, the variance in z is derived with Gaussian fitting as shown in Figure 5-5.

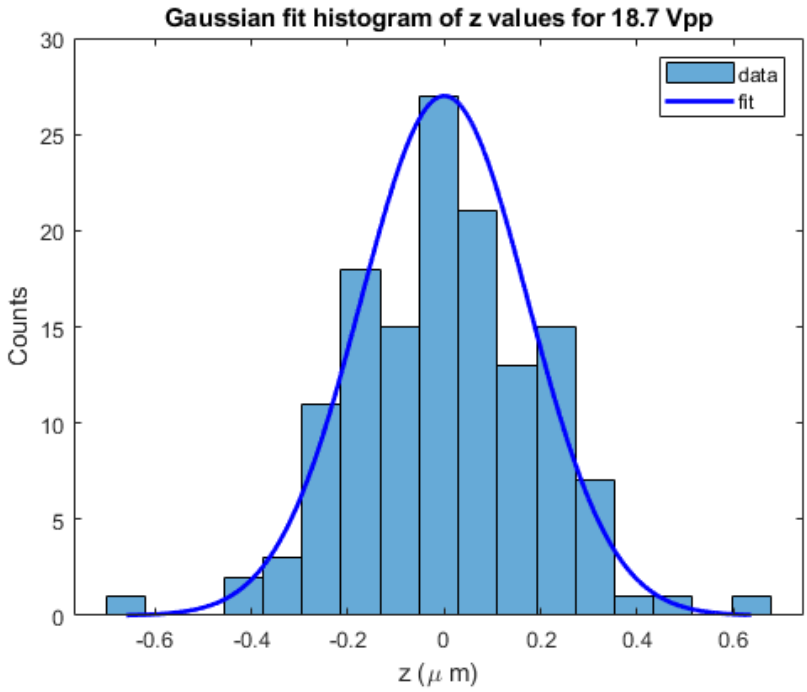

Figure 5-5: Histogram of z values for trapping with 18.7 peak-to-peak voltage with the double-sided tape chip. Gaussian fit is applied to determine the variance of the z positions, which is equal to 0.1732 μm. This histogram is obtained from 30 seconds video using one single, double-sided tape chip with an image acquisition rate of 50 frames per second for 2 beads with an average of 100 frames per bead due to planar motion.

5-5-4 Equipartition theory

The equipartition theory describes the stiffness of an acoustic trap. This theory is dependent on the frame rate of the image acquisition device, but it will saturate to a fixed value, as is shown by Pesce et al. [65]. and Gerspach et al. [30]. Gerspach et al. described that the saturation value could be used to determine the trapping stiffness, which will make the equipartition theory independent of the frame rate of the capturing device. For one coordinate, the saturated equipartition theory value is given by [65]:

$$var(z) = \frac{2k_B T}{k_z} \tag{5-3}$$

Where $var(z)$ represents the variance in the axial position z (in m), k_B represents the Boltzmann constant, T is the absolute temperature (in K), and k_z is the stiffness of the trap in the axial direction z (in N/m).

By assuming the absolute temperature to be 293.15 K, one can derive the trapping stiffness for 18.7 V_{pp} shown in Figure 5-5 to be 0.54 $\pm$0.05 pN/μm.

5-5-5 Propagation of uncertainty

The following equations are used to propagate fractional uncertainties:

$$\begin{aligned} \frac{\delta y}{y} &= n\frac{\delta a}{a} && \text{if } y = a^n \\ \frac{\delta y}{y} &= \delta a + \delta b && \text{if } y = a + b \\ \frac{\delta y}{y} &= \frac{\delta a}{a} + \frac{\delta b}{b} + \frac{\delta c}{c} && \text{if } y = \frac{ab}{c} \end{aligned} \tag{5-4}$$

Several sources of error propagate to the trapping stiffness. By propagating the fractional uncertainty with Equation 5-3, one can deduce that the fractional uncertainty on the stiffness is given by:

$$\frac{\delta k_z}{k_z} = \frac{\delta T}{T} + \frac{\delta var(z)}{var(z)} \tag{5-5}$$

Where δk_z, δT and $\delta var(z)$ represent the uncertainty in trapping stiffness, temperature and variance in z, respectively.

It is assumed that the uncertainty in temperature is just a few degrees [44]. The value of $\delta var(z)$ can be derived by using the definition of variance and the assumption that z has zero mean, which will result in:

$$\begin{aligned} var(z) &= \frac{1}{N}\sum_{i=1}^{N}(z_i)^2 \\ &= \frac{1}{N}(z_1^2 + z_2^2 + ... + z_N^2) \\ &= \frac{1}{N}(y_1 + y_2 + ... + y_N) \end{aligned} \tag{5-6}$$

By applying the error propagation equation for the sum and power and assuming that the fractional uncertainty is the same for all values of z, one can obtain:

$$\begin{aligned} \frac{\delta y_i}{y_i} &= 2\frac{\delta z_i}{z_i} \rightarrow \\ \delta var(z) &= \frac{1}{N}(\delta y_1 + \delta y_2 + ... + \delta y_N) \\ &= \frac{1}{N}(2z_1^2\frac{\delta z_1}{z_1} + 2z_2^2\frac{\delta z_2}{z_2} + ... + 2z_N^2\frac{\delta z_N}{z_N}) \\ &= 2\frac{\delta z}{z}var(z) \end{aligned} \tag{5-7}$$

The fraction uncertainty on $var(z)$ can now be described as:

$$\frac{\delta var(z)}{var(z)} = 2\frac{\delta z}{z} \tag{5-8}$$

Now by using a simplified version of the calibration curve:

$$\sigma_x \approx az^2 + b \tag{5-9}$$

With Equation 5-9, the uncertainty on σ_x can be estimated by:

$$\begin{aligned} \frac{\delta \sigma_x}{\sigma_x} &\approx 2\frac{\delta z}{z} + \frac{\delta b}{b} \rightarrow \\ 2\frac{\delta z}{z} &\approx \frac{\delta \sigma_x}{\sigma_x} + \frac{\delta b}{b} \end{aligned} \tag{5-10}$$

So by combining Equation 5-5, Equation 5-8 and Equation 5-10 together one will derive:

$$\frac{\delta k_z}{k_z} = \frac{\delta T}{T} + \frac{\delta \sigma_x}{\sigma_x} + \frac{\delta b}{b} \tag{5-11}$$

In Equation 5-11 the first term on the right hand side describes the uncertainty due to temperature ($\delta T = 2$ °C), the second term is the uncertainty in the calibration curve shown in Figure 5-4 due to varying bead sizes, uncertainty due to finite accuracy adjusting of the focal plane and optical aberrations that will affect the σ_x value ($\delta\sigma_x = 0.06$ micron), and the third term describes the uncertainty on k_z due to variance in bead size ($\delta b = 0.022$ micron).

Sitters et al. [71] showed that for a 4 V_{pp} the piezo heated up around 3°C for actuation at 6.7 MHz for 6 minutes. The heating of the fluid as a result of this is hard to predict since the heating of the piezo is affected by its size, geometry, material properties and conditions of the room it is in. Therefore, the piezo is actuated for only 30 seconds to capture trapping videos and turned off again to minimise this uncertainty. For each new V_{pp} value, the piezo is turned on and off again. Sitters et al. reported a sample temperature increase of a few degrees [71]. This will also be assumed for this chip.

There is also focal plane drift that can cause uncertainty in the measurement, but since the microscope provides means to manual lock the position of the focal plane, this uncertainty is neglected.

Carlucci et al. [14] also described sources of error coming from the limited axial range of most three-dimensional bead tracking methods due to low signal-to-noise ratio far away from the focal plane, as can be observed in Figure 5-4. In addition, the beads' movement in the lateral plane during trapping can lead to blurring and distortions of the beads' intensity profile. The distortion due to lateral movement is minimised by filtering the beads based on the difference between w_x and w_y as explained in subsection 5-3-1. Another mechanism that leads to uncertainty is the nonuniformity of the beads themselves. For example, an asymmetric bead that rotates will influence the beads' intensity profile and, therefore, also the trapping stiffness. To minimise this error, small bead sizes are chosen under the assumption that the effect of impurities is smaller [14].

5-6 Results

This section will present the trapping stiffness of the fundamental mode at 50 $\pm 0.1\mu$m from the bottom glass. The trap stiffness from simulation with and without glue is compared to the experimental derived trap stiffness in Figure 5-6. The glue layer between the piezo, aluminium layer and glass is assumed to have a thickness of 20 μm, which is around the same thickness as the aluminium layer. The material properties of the epoxy layer in the simulation are: E = 3.45 GPa, $\nu = 0.321$, $\rho = 1.44$ kg/m^3 [59].

The error bars on the experimental stiffness are obtained with Equation 5-11, and the uncertainty in V_{pp} is equal to one percent according to the specifications of the signal generator.

During the experiments, it was also found that the beads will move towards each other after some time in the acoustic trap for a ten times higher concentration of beads, $1.8461 \cdot 10^8$ beads/mL. Furthermore, the attraction between beads was more pronounced for higher V_{pp} values. This phenomenon is shown in Figure 5-7.

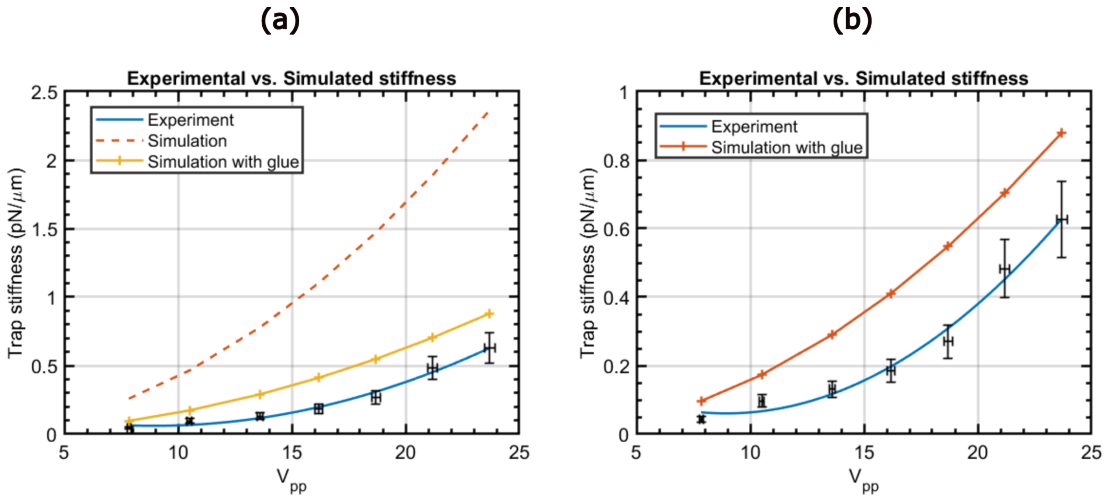

Figure 5-6: A plot of the simulated and experimental trap stiffness at 50 $\pm 0.1\mu$m away from the bottom cover glass, for a range of V_{pp} values using the double-sided tape chip. The error bars represent the uncertainty in the experimental stiffness and the applied V_{pp} value. (a) Experimental trapping stiffness plotted together with simulated stiffness with (at 7.13 MHz) and without the glue layer (at 7.41 MHz). (b) Experimental strapping stiffness plotted together with the simulated trapping stiffness with glue.

5-7 Discussion

The highest measured trap stiffness is around 0.6 pN/μm for a 1.5-micron bead. Since the sinusoidal acoustic radiation force is roughly linear close to a node, the force it exerts on a 10 μm DNA can be calculated with just the trap stiffness times the length of the DNA, which is equal to 6 pN. From Equation 2-9, it can be derived that the acoustic radiation force scales with the volume of the bead and the gravity force is cancelled mainly by the buoyancy force. So the expected maximum force on the DNA for a 4.5 μm bead should be 27 times this value, equal to 162 pN.

Although the target stiffness was reached, there is still some discrepancy between the experimentally obtained and simulated stiffness curves. The deviation is considerable when the glue layer is not simulated as shown in Figure 5-6. The glue layers between the piezo chip and aluminium foil, between the aluminium foil and the glass and between the double-sided tape and two glass interfaces will have a much lower quality factor. They will therefore attenuate the acoustic radiation energy more.

The experimental results are closer to the simulation model that takes glue into account. However, there is still some discrepancy between these two stiffness curves. This may occur due to the trapping of air bubbles during the fabrication process by the double-sided tape, which can also lower the overall trap stiffness.

Tilt and decenter of the piezo chip can cause discrepancies between simulation and experiments since the displacement of a piezoelectric transducer is not uniform [69]. This means that if the center of the piezo is close to the tape layer, it may be damped more. In addition, tilts caused by glueing layers with nonuniform thicknesses can increase the deviation between the model and experiments.

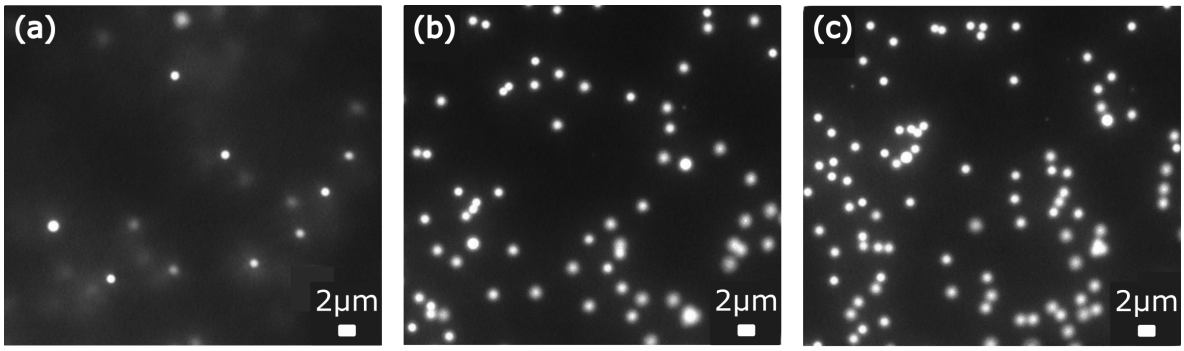

Figure 5-7: (a)Image of beads without actuation of piezo. (b) Bead trapping right after actuation of piezo. (c) Bead trapping 9.6 seconds after actuation.

Another source for the discrepancy can be caused by the solder on top of the piezo that will add damping to the piezo.

Also, all the materials, including the double-sided tape, are assumed to be homogeneous linear elastic materials. However, more complex models are needed to represent the glueing layers accurately.

Finally, operating the piezo at high input voltages will cause temperature effects on the material, leading to much more damping, especially for the glue layer. In addition, the properties of the glue can change a lot, which results in more damping [23].

Chapter 6

Conclusion

This chapter aims to summarise the main findings and insights gained during this master thesis project. Hereafter, recommendations are made, and a future outlook will be provided to the future user and researchers of this chip to improve its performance further.

6-1 Summary

The human body is perhaps the most complex system in existence. Although a lot of ground-breaking research and discoveries have been conducted, the working principle behind the replication process can still not be fully quantified. Nevertheless, the replication process is the fundamental process of life. Gaining more insight into this process may lead to the development of medicine for diseases that are still incurable today.

The replication process is widely considered a stochastic process, which is the main reason why the acoustic tweezer, similar to the one developed in this report, is gaining increased attention. Furthermore, this tweezer offers highly multiplexed DNA manipulation capabilities and will therefore offer statistically significant data time-efficiently.

Several kinds of micro-particle manipulation methods are available, but compared with these methods, the acoustic tweezer is relatively easy to build and operate and cost-effective. While capable of still offering comparable performance.

In this report, we focused on the standing wave device (BAW) and showed that it could reach 120 pN force on a 10 μm DNA strand attached to the coverglass on one side and a 4.5 μm polystyrene microbead on the other. Moreover, it can be built for less than €10, which is more than ten times the price reduction compared to the flow cell made by Lumicks.

In addition, all design requirements outlined in section 2-1 are met. This allows it to be utilized in studying the replication dynamics and also the interaction between beads.

6-2 Recommendations/Outlook

The main motivation behind developing the acoustic tweezer was to study DNA replication in a highly multiplexed setting. However, due to time limitations, it was not possible to perform these experiments within the time frame of this project. Therefore it is highly recommended to utilize this chip in micro-bead tethered DNA experiments.

The planar motion of the bead during trapping resulted in more uncertainty in the trapping stiffness due to possible distortions and variance in bead sizes. To get more accurate results, it is recommended to perform calibration and trapping with the same bead in real time.

In this thesis project, microbeads are not tracked. Instead, a region of interest is used to get as close as possible to analyzing single beads, so by expanding this code to contain bead tracking over the whole field of view, the trap stiffness can be evaluated for every single bead, and this will result in more accurate stiffness data. And pave the way to quantify the position dependence of the trap stiffness.

During this project, fluid control with a microfluidic pump was explored to counter the planar motion of the beads, but due to time limitations, it was not possible to fine-tune this process and get actual results. This is an interesting research opportunity for further research.

Another interesting field of study is the particle-to-particle interaction and the accuracy of the FEM model for flow cells with different geometries. From experimental observations, it seems that higher input voltages will result in increased attraction between particles. The formation of angled sidewalls was observed during the optimization process of the femto laser cut process parameters. The effect of these angled sidewalls on the trapping capability is, to the best of the authors' knowledge, not been presented in literature before. Further research is needed to quantify this effect.

Future suggestions to improve the trapping performance are optimising the laser-cut channels further and grounding down the edges to make glass-to-glass bonding without the need for any polymer between the glass layers, and purchasing piezo with wrap-around electrodes to minimize the use of glue. However, this will increase the cost of the chip and therefore does not match our main objective. It may be advisable to develop an accurate model of the glue and tape layers using more accurate finite element models mentioned in subsection 5-5-5.

In subsection 1-1-2, it was mentioned that the main disadvantage of acoustic tweezers compared to other types of tweezers is its limited spatial resolution in manipulating microparticles. During this thesis project, an interesting idea was discussed to increase the spatial resolution of the acoustic tweezer by replacing the spacer material between the glass layer with piezo ceramic material. The idea was to actuate the piezoceramic material to change the fluid layer's height and provide high spatial resolution by controlled shifting of the trapping plane. This is another interesting research area to increase the spatial resolution of the acoustic tweezer.

Also, further research is needed to verify the assumption of limited temperature effect on the trap stiffness by measuring the piezo's heating as was done by Sitters et al. [71].

The main objective of this project is to present easy-to-build and low-cost acoustic tweezers available to anyone interested in conducting experiments with microparticles or micro-bead tethered DNA. By lowering the barrier to microparticle manipulation methods, the authors are hopeful that this will lead to accelerated breakthroughs.

Appendix A

Proofs and derivations

A-1 Intuition behind circuit equivalent model

The equivalent circuit model for the piezoelectric transducer is based on the similarity between the mechanical mass-spring-damper model and the electric circuit consisting of a resistor, inductor, and capacitor connected in series [75].

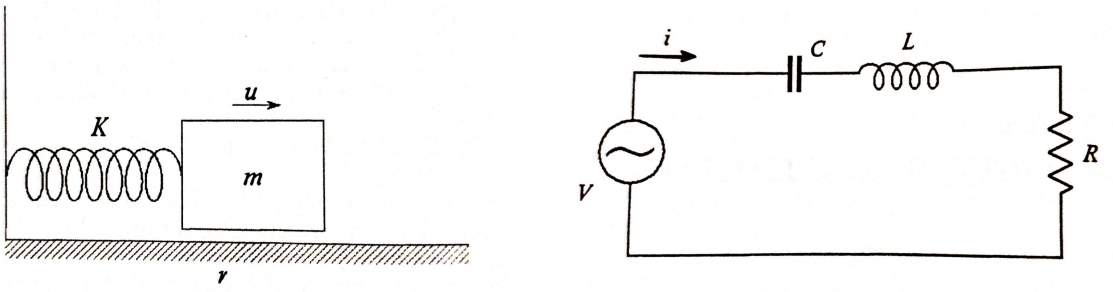

Figure A-1: Intuition behind the circuit equivalent model for piezoelectric actuators (a) Mass-spring-damper system that can be used to represent a piezoelectric actuator. Where K represents the spring stiffness, m is the mass, ν is the resistive damping coefficient, and u is the oscillating velocity of the mass. (b) Electrical circuit equivalent to the mass-spring-damper system with resistance R, inductance L, capacitance C, current i and oscillating voltage V. These figures are adapted from [75]

The equation of motion by applying an oscillating force $F_0 e^{j\omega t}$ on the mass-spring-damper system shown in Figure A-1a can be derived with Newton's second law of motion and reads as:

$$F_0 e^{j\omega t} = m\frac{du}{dt} + \nu u + K\int u dt \tag{A-1}$$

By applying an oscillating voltage $V_0 e^{j\omega t}$ to the electric circuit shown in Figure A-1b, the following equation can be derived:

$$V_0 e^{j\omega t} = L\frac{di}{dt} + Ri + \frac{1}{C}\int i dt \tag{A-2}$$

The similarity in form between Equation A-1 and Equation A-2 can be used to derive the model for the layered resonator.

Bibliography

[1] Daniel Ahmed, Adem Ozcelik, Nagagireesh Bojanala, Nitesh Nama, Awani Upadhyay, Yuchao Chen, Wendy Hanna-Rose, and Tony Jun Huang. Rotational manipulation of single cells and organisms using acoustic waves. *Nature communications*, 7(1):1–11, 2016.

[2] alufoil European Aluminium Foil Association. Aluminium foil: Characteristics and properties. https://www.alufoil.org/properties. Accessed: 2022-07-1.

[3] Arthur Ashkin and James M Dziedzic. Optical trapping and manipulation of viruses and bacteria. *Science*, 235(4795):1517–1520, 1987.

[4] Arthur Ashkin, James M Dziedzic, John E Bjorkholm, and Steven Chu. Observation of a single-beam gradient force optical trap for dielectric particles. *Optics letters*, 11(5):288–290, 1986.

[5] Thierry Baasch, Ivo Leibacher, and Jürg Dual. Multibody dynamics in acoustophoresis. *The Journal of the Acoustical Society of America*, 141(3):1664–1674, 2017.

[6] Andreas R Bausch, Winfried Möller, and Erich Sackmann. Measurement of local viscoelasticity and forces in living cells by magnetic tweezers. *Biophysical journal*, 76(1):573–579, 1999.

[7] Daniel Blair and Eric Dufresne. Particle location and tracking tutorial. https://site.physics.georgetown.edu/matlab/. Accessed: 2022-07-06.

[8] Alfonso Blázquez-Castro. Optical tweezers: phototoxicity and thermal stress in cells and biomolecules. *Micromachines*, 10(8):507, 2019.

[9] Rebeca Bocanegra, GA Ismael Plaza, Carlos R Pulido, and Borja Ibarra. Dna replication machinery: Insights from in vitro single-molecule approaches. *Computational and Structural Biotechnology Journal*, 19:2057–2069, 2021.

[10] Henrik Bruus. Acoustofluidics 7: The acoustic radiation force on small particles. *Lab on a Chip*, 12(6):1014–1021, 2012.

[11] Carlos Bustamante, Wei Cheng, and Yara X Mejia. Revisiting the central dogma one molecule at a time. *Cell*, 144(4):480–497, 2011.

[12] Carlos Bustamante, John F Marko, Eric D Siggia, and S Smith. Entropic elasticity of λ-phage dna. *Science*, 265(5178):1599–1600, 1994.

[13] Joan Camunas-Soler, Marco Ribezzi-Crivellari, and Felix Ritort. Elastic properties of nucleic acids by single-molecule force spectroscopy. *Annual review of biophysics*, 45:65–84, 2016.

[14] Laura A Carlucci and Wendy E Thomas. Modification to axial tracking for mobile magnetic microspheres. *Biophysical Reports*, 1(2):100031, 2021.

[15] Jiajie Chen, Hengji Cong, Fong-Chuen Loo, Zhiwen Kang, Minghui Tang, Haixi Zhang, Shu-Yuen Wu, Siu-Kai Kong, and Ho-Pui Ho. Thermal gradient induced tweezers for the manipulation of particles and cells. *Scientific reports*, 6(1):1–13, 2016.

[16] Suzanne Clancy. Dna damage & repair: mechanisms for maintaining dna integrity. *Nature Education*, 1(1):103, 2008.

[17] Jelmer P Cnossen, David Dulin, and NH Dekker. An optimized software framework for real-time, high-throughput tracking of spherical beads. *Review of Scientific Instruments*, 85(10):103712, 2014.

[18] Adam E Cohen and WE Moerner. Method for trapping and manipulating nanoscale objects in solution. *Applied physics letters*, 86(9):093109, 2005.

[19] COMSOL. Piezoacoustic transducer. https://www.comsol.com/model/piezoacoustic-transducer-1477. Accessed: 2021-08-1.

[20] CONRAD. 3m 665dp old665dp dubbelzijdige tape scotch 665 transparant (l x b) 7.9 m x 12 mm 1 stuk(s). https://www.conrad.nl/nl/p/3m-665dp-old665dp-dubbelzijdige-tape-scotch-665-transparant-l-x-b-7-9-m-x-12-mm-1-stuk-s-542464.html. Accessed: 2022-07-1.

[21] Ghulam Destgeer, Hyunjun Cho, Byung Hang Ha, Jin Ho Jung, Jinsoo Park, and Hyung Jin Sung. Acoustofluidic particle manipulation inside a sessile droplet: four distinct regimes of particle concentration. *Lab on a Chip*, 16(4):660–667, 2016.

[22] Xiaoyun Ding, Peng Li, Sz-Chin Steven Lin, Zackary S Stratton, Nitesh Nama, Feng Guo, Daniel Slotcavage, Xiaole Mao, Jinjie Shi, Francesco Costanzo, et al. Surface acoustic wave microfluidics. *Lab on a Chip*, 13(18):3626–3649, 2013.

[23] Jurg Dual and Thomas Schwarz. Acoustofluidics 3: Continuum mechanics for ultrasonic particle manipulation. *Lab on a Chip*, 12(2):244–252, 2012.

[24] David Dulin, Tao Ju Cui, Jelmer Cnossen, Margreet W Docter, Jan Lipfert, and Nynke H Dekker. High spatiotemporal-resolution magnetic tweezers: calibration and applications for dna dynamics. *Biophysical journal*, 109(10):2113–2125, 2015.

[25] American Elements. Aluminum foil. https://www.americanelements.com/aluminum-foil-7429-90-5. Accessed: 2022-07-1.

[26] Xingyu Fan and Jun Li. Damage identification in plate structures using sparse regularization based electromechanical impedance technique. *Sensors*, 20(24):7069, 2020.

[27] Richard S Figliola and Donald E Beasley. *Theory and design for mechanical measurements*. John Wiley & Sons, 2020.

[28] Shun-ichi Funano, Nobutoshi Ota, and Yo Tanaka. A simple and reversible glass–glass bonding method to construct a microfluidic device and its application for cell recovery. *Lab on a Chip*, 21(11):2244–2254, 2021.

[29] L Gardini, A Tempestini, FS Pavone, and M Capitanio. High-speed optical tweezers for the study of single molecular motors. In *Molecular Motors*, pages 151–184. Springer, 2018.

[30] Michael A Gerspach, Nassir Mojarad, Deepika Sharma, Thomas Pfohl, and Yasin Ekinci. Soft electrostatic trapping in nanofluidics. *Microsystems & nanoengineering*, 3(1):1–10, 2017.

[31] Peter Glynne-Jones, Rosemary J Boltryk, and Martyn Hill. Acoustofluidics 9: Modelling and applications of planar resonant devices for acoustic particle manipulation. *Lab on a Chip*, 12(8):1417–1426, 2012.

[32] Andrei A Golosov, Joshua J Warren, Lorena S Beese, and Martin Karplus. The mechanism of the translocation step in dna replication by dna polymerase i: a computer simulation analysis. *Structure*, 18(1):83–93, 2010.

[33] Yuxuan Gong, Scott T Misture, Peng Gao, and Nathan P Mellott. Surface roughness measurements using power spectrum density analysis with enhanced spatial correlation length. *The Journal of Physical Chemistry C*, 120(39):22358–22364, 2016.

[34] J Hawkes Jeremy, Gröschl Martin, Benes Ewald, Nowotny Helmut, and Coakley W Terence. Positioning particles within liquids using ultrasound force fields.

[35] Øystein Ivar Helle, Balpreet Singh Ahluwalia, and Olav Gaute Hellesø. Optical transport, lifting and trapping of micro-particles by planar waveguides. *Optics express*, 23(5):6601–6612, 2015.

[36] Martyn Hill, Yijun Shen, and Jeremy J Hawkes. Modelling of layered resonators for ultrasonic separation. *Ultrasonics*, 40(1-8):385–392, 2002.

[37] Martyn Hill, Rosemary J Townsend, and Nicholas R Harris. Modelling for the robust design of layered resonators for ultrasonic particle manipulation. *Ultrasonics*, 48(6-7):521–528, 2008.

[38] Martyn Hill and Robert JK Wood. Modelling in the design of a flow-through ultrasonic separator. *Ultrasonics*, 38(1-8):662–665, 2000.

[39] Po-Hsun Huang, Nitesh Nama, Zhangming Mao, Peng Li, Joseph Rufo, Yuchao Chen, Yuliang Xie, Cheng-Hsin Wei, Lin Wang, and Tony Jun Huang. A reliable and programmable acoustofluidic pump powered by oscillating sharp-edge structures. *Lab on a Chip*, 14(22):4319–4323, 2014.

[40] Polysciences Inc. Fluoresbrite® yg carboxylate microspheres 1.50µm. https://www.polysciences.com/india/fluoresbrite-yg-carboxylate-microspheres-150m. Accessed: 2021-10-1.

[41] TED PELLA INC. Schott d263m glass coverslips technical data. https://www.tedpella.com/histo_html/coverslip-info.aspx. Accessed: 2022-07-1.

[42] VWR International. Objectglaasjes. https://nl.vwr.com/store/product/564378/objectglaasjes#order. Accessed: 2022-07-1.

[43] Frank Jülicher and Robijn Bruinsma. Motion of rna polymerase along dna: a stochastic model. *Biophysical journal*, 74(3):1169–1185, 1998.

[44] Douwe Kamsma, Ramon Creyghton, Gerrit Sitters, Gijs JL Wuite, and Erwin JG Peterman. Tuning the music: acoustic force spectroscopy (afs) 2.0. *Methods*, 105:26–33, 2016.

[45] Mohammad R Kasaai, Vijayalakshmi Kacham, Francis Theberge, and See Leang Chin. The interaction of femtosecond and nanosecond laser pulses with the surface of glass. *Journal of Non-Crystalline Solids*, 319(1-2):129–135, 2003.

[46] Keyence. Area roughness parameters. https://www.keyence.com/ss/products/microscope/roughness/surface/parameters.jsp. Accessed: 2022-07-06.

[47] Jadoon Khan. Difference between ssdna vs dsdna (table): Easy biology class, Jul 2020.

[48] Lawrence E Kinsler, Austin R Frey, Alan B Coppens, and James V Sanders. *Fundamentals of acoustics*. John wiley & sons, 2000.

[49] Richard Krimholtz, David A Leedom, and George L Matthaei. New equivalent circuits for elementary piezoelectric transducers. *Electronics Letters*, 6(13):398–399, 1970.

[50] Imam Kusyairi, Helmy Mukti Himawan, Moch Agus Choiron, and Yudy Surya Irawan. Manufacture of origami pattern crash box using traditional investment casting method. In *IOP Conference Series: Materials Science and Engineering*, volume 494, page 012006. IOP Publishing, 2019.

[51] Junjun Lei, Martyn Hill, Carlos Ponce de León Albarrán, and Peter Glynne-Jones. Effects of micron scale surface profiles on acoustic streaming. *Microfluidics and Nanofluidics*, 22(12):1–14, 2018.

[52] Andreas Lenshof, Mikael Evander, Thomas Laurell, and Johan Nilsson. Acoustofluidics 5: Building microfluidic acoustic resonators. *Lab on a Chip*, 12(4):684–695, 2012.

[53] Changning Liu, Yang Liao, Fei He, Yinglong Shen, Danping Chen, Ya Cheng, Zhizhan Xu, Koji Sugioka, and Katsumi Midorikawa. Fabrication of three-dimensional microfluidic channels inside glass using nanosecond laser direct writing. *Optics Express*, 20(4):4291–4296, 2012.

[54] MY Polymers Ltd. Bio-photonics materials. https://www.mypolymers.com/products. Accessed: 2022-08-1.

[55] Lumicks. u-flux™ microfluidics flow cells. https://store.lumicks.com/product/u-flux-microfluidics-flow-cells-c1-c2/. Accessed: 2022-08-20.

[56] Barry R Lutz, Jian Chen, and Daniel T Schwartz. Hydrodynamic tweezers: 1. noncontact trapping of single cells using steady streaming microeddies. *Analytical chemistry*, 78(15):5429–5435, 2006.

[57] Berenike Maier, David Bensimon, and Vincent Croquette. Replication by a single dna polymerase of a stretched single-stranded dna. *Proceedings of the National Academy of Sciences*, 97(22):12002–12007, 2000.

[58] Asier Marzo, Sue Ann Seah, Bruce W Drinkwater, Deepak Ranjan Sahoo, Benjamin Long, and Sriram Subramanian. Holographic acoustic elements for manipulation of levitated objects. *Nature communications*, 6(1):1–7, 2015.

[59] MatWeb. Overview of materials for epoxy adhesive. https://www.matweb.com/search/datasheettext.aspx?matguid=c1ec1ad603c74f628578663aaf44f261. Accessed: 2022-8-20.

[60] Ronán McCann, Komal Bagga, Gabriel Duaux, Apryll Stalcup, Mercedes Vázquez, and Dermot Brabazon. Taguchi method modelling of nd: Yag laser ablation of microchannels on cyclic olefin polymer film. *Optics & Laser Technology*, 106:265–271, 2018.

[61] Kai Melde, Andrew G Mark, Tian Qiu, and Peer Fischer. Holograms for acoustics. *Nature*, 537(7621):518–522, 2016.

[62] Long Meng, Feiyan Cai, Fei Li, Wei Zhou, Lili Niu, and Hairong Zheng. Acoustic tweezers. *Journal of Physics D: Applied Physics*, 52(27):273001, 2019.

[63] Gero Nootz. Fit 2d gaussian function to data. https://nl.mathworks.com/matlabcentral/fileexchange/37087-fit-2d-gaussian-function-to-data. Accessed: 2022-07-06.

[64] Adem Ozcelik, Joseph Rufo, Feng Guo, Yuyang Gu, Peng Li, James Lata, and Tony Jun Huang. Acoustic tweezers for the life sciences. *Nature methods*, 15(12):1021–1028, 2018.

[65] Giuseppe Pesce, Giorgio Volpe, Onofrio M Maragó, Philip H Jones, Sylvain Gigan, Antonio Sasso, and Giovanni Volpe. Step-by-step guide to the realization of advanced optical tweezers. *JOSA B*, 32(5):B84–B98, 2015.

[66] Rings M. Ponsen C., Cedric S. Engineering a microfluidic device for acoustic levitation of microbeads. unpublished, 2022.

[67] Leslie Pray. Discovery of dna structure and function: Watson and crick. *Nature Education*, 1(1), 2008.

[68] Roland Probst and Benjamin Shapiro. Three-dimensional electrokinetic tweezing: device design, modeling, and control algorithms. *Journal of Micromechanics and Microengineering*, 21(2):027004, 2011.

[69] Ahmad Safari. *Piezoelectric and acoustic materials for transducer applications*. Springer, 2010.

[70] Mikkel Settnes and Henrik Bruus. Forces acting on a small particle in an acoustical field in a viscous fluid. *Physical Review E*, 85(1):016327, 2012.

[71] Gerrit Sitters, Douwe Kamsma, Gregor Thalhammer, Monika Ritsch-Marte, Erwin JG Peterman, and Gijs JL Wuite. Acoustic force spectroscopy. *Nature methods*, 12(1):47–50, 2015.

[72] Steven B Smith, Yujia Cui, and Carlos Bustamante. Overstretching b-dna: the elastic response of individual double-stranded and single-stranded dna molecules. *Science*, 271(5250):795–799, 1996.

[73] Steven B Smith, Laura Finzi, and Carlos Bustamante. Direct mechanical measurements of the elasticity of single dna molecules by using magnetic beads. *Science*, 258(5085):1122–1126, 1992.

[74] L Spigarelli, NS Vasile, CF Pirri, and G Canavese. Numerical study of the effect of channel aspect ratio on particle focusing in acoustophoretic devices. *Scientific reports*, 10(1):1–11, 2020.

[75] Dennis Stansfield. *Underwater electroacoustic transducers: a handbook for users and designers*. Peninsula Publishing, 2017.

[76] PI store. Product information "pryy+0398". https://www.physikinstrumente.store/us/pryy-0398/. Accessed: 2022-06-1.

[77] Henrik Sönnerlind. How to model adhesion and decohesion in comsol multiphysics. https://www.comsol.com/blogs/how-to-model-adhesion-and-decohesion-in-comsol-multiphysics. Accessed: 2022-8-1.

[78] Paul A Tipler and Gene Mosca. *Physics for scientists and engineers*. Macmillan, 2021.

[79] SB Tiwari and B Nageswara Rao. Finite element modeling of adhesively bonded joints. *Trends in Applied Sciences Research*, 1(1):25–40, 2006.

[80] RJ Townsend, M Hill, NR Harris, and MB McDonnell. Performance of a quarter-wavelength particle concentrator. *Ultrasonics*, 48(6-7):515–520, 2008.

[81] Continental Trade. Soda lime glass. https://www.continentaltrade.com.pl/soda-lime-glass. Accessed: 2022-07-1.

[82] Joost van Mameren, Peter Gross, Geraldine Farge, Pleuni Hooijman, Mauro Modesti, Maria Falkenberg, Gijs JL Wuite, and Erwin JG Peterman. Unraveling the structure of dna during overstretching by using multicolor, single-molecule fluorescence imaging. *Proceedings of the National Academy of Sciences*, 106(43):18231–18236, 2009.

[83] VWR. Optical analysis microscope accessories. https://www.slaughter.co.uk/image/CatPagePDF/VWRAPPS2015/Bigbook%20UK%20PDF%202142.pdf. Accessed: 2022-07-1.

[84] Kai Wang, Ethan Schonbrun, Paul Steinvurzel, and Kenneth B Crozier. Trapping and rotating nanoparticles using a plasmonic nano-tweezer with an integrated heat sink. *Nature communications*, 2(1):1–6, 2011.

[85] James D Watson and Francis HC Crick. Molecular structure of nucleic acids: a structure for deoxyribose nucleic acid. *Nature*, 171(4356):737–738, 1953.

[86] Ming C Wu. Optoelectronic tweezers. *Nature Photonics*, 5(6):322–324, 2011.

[87] Gijs JL Wuite, Steven B Smith, Mark Young, David Keller, and Carlos Bustamante. Single-molecule studies of the effect of template tension on t7 dna polymerase activity. *Nature*, 404(6773):103–106, 2000.

[88] Limin Xiang, Kun Chen, and Ke Xu. Single molecules are your quanta: A bottom-up approach toward multidimensional super-resolution microscopy. *ACS nano*, 2021.

[89] Hu Zhang and Kuo-Kang Liu. Optical tweezers for single cells. *Journal of the Royal Society interface*, 5(24):671–690, 2008.

[90] Yongzhuang Zhou, Michael Handley, Guillem Carles, and Andrew R Harvey. Advances in 3d single particle localization microscopy. *APL photonics*, 4(6):060901, 2019.

Glossary

List of Acronyms

AFS	Acoustic Force Spectroscopy
BAW	bulk acoustic wave
DI	deionized water
DNA	Deoxyribonucleic acid
DNApol	DNA polymerase
dsDNA	double-stranded DNA
epi	echo-planar imaging
FEM	finite element method
FJC	freely jointed chain
FPS	frames per second
IDTs	interdigitated transducers
kbp	kilo base pairs
KLM	Krimholtz, Leedom and Matthae model
ROI	region of interest
SMLM	single-molecule localization microscopy
SAW	surface acoustic wave
ssDNA	single-stranded DNA
$\mathbf{V}_{pp}$	peak-to-peak voltage
WLC	worm-like chain
ANOVA	analysis of variance